ISSN 1349-6832

JEOL news

July 2007 Vol.42 No.1

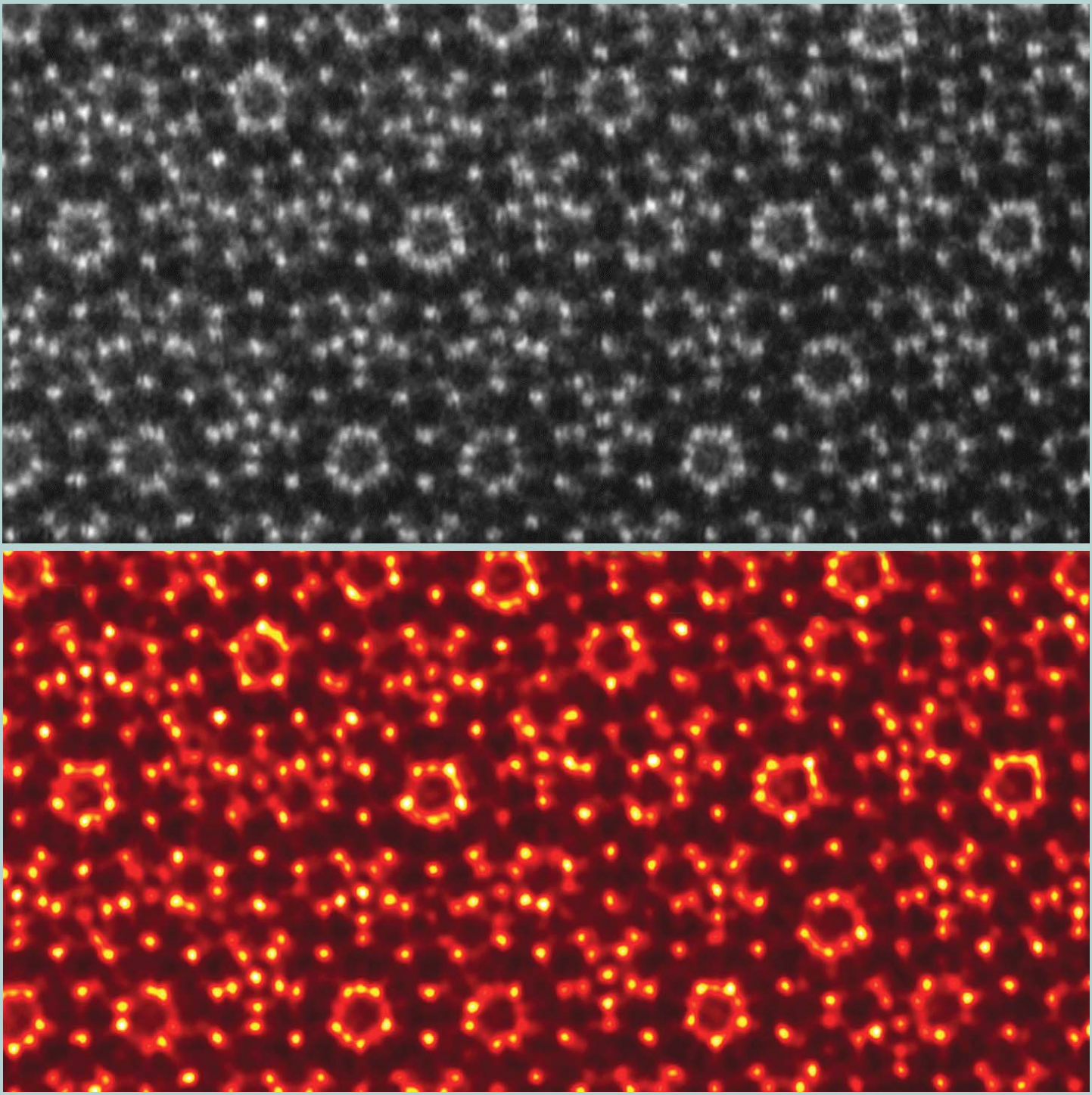

JEOL news

Volume 42 Number 1
July, 2007

Characterization of the JEM-2100F -LM TEM for Electron Holography and Magnetic Imaging

M. A. Schofield†, M. Beleggia†, J. W. Lau†,†† and Y. Zhu†

†Institute for Advanced Electron Microscopy, Brookhaven National Laboratory, USA
††Currently, National Institute of Standards and Technology, USA

The holography performance and magnetic imaging capabilities of the JEM-2100F-LM electron microscope are reported here. Measurements of the fringe spacing, contrast, and hologram width obtained as a function of applied biprism voltage are presented. Measurements of the spherical aberration coefficient Cs = (108.7 ± 2.2) mm and minimum achievable focal step δf = (87.6 ± 1.4) nm for the specially designed objective lens of this microscope are also presented. We characterize the magnetic field present in the sample region of the JEM-2100F-LM and find a remnant field about 4 Oe under normal operating conditions. Additionally, we characterize the objective lens remnant field along two orthogonal directions, the spatial characteristics of the field profile during specimen entry into the column, and the field conditions at the sample region as a function of objective lens excitation. Finally, we provide experimental holography results illustrating some of the more unique capabilities of the microscope.

Introduction

Several experimental techniques (each having distinct advantages and disadvantages, or applicability) are available to study magnetic structure and properties of materials [1, 2]. As the characteristic size in device technologies utilizing magnetic phenomena decreases, quantitative magnetic materials research with ever increasing spatial resolution and sensitivity becomes critical. For example, understanding reversal dynamics, the effect of neighboring magnetic elements, or the fine details of magnetic structures is crucial to continued technological development, and methods capable of quantitative magnetization measurement with high sensitivity and spatial resolution are required.

Of the available techniques to carry out quantitative magnetization measurement, off-axis electron holography in a transmission electron microscope (TEM) [3, 4] has significant potential with regard to spatial resolution and sensitivity compared to many other techniques. By recovering the phase shift of electrons passing through the sample, a direct relation to the electrostatic and magnetostatic potentials associated with the sample is obtained [5]. A critical aspect of holography is to characterize the fringe spacing and contrast that can be obtained with the holography setup for a given instrument. The fringe spacing is directly related to the spatial resolution that can be obtained [6], while the fringe contrast directly determines the phase sensitivity of the experiment [7]. Along with the width of the interference patch, these parameters specify the limits of what features are meaningful in the recovered electron phase shift.

In studies of magnetic materials, electron holography is certainly not the only useful TEM technique. Indeed, important information of the magnetic structure and domain configuration down to the nanometer scale can be obtained through Lorentz and Foucault modes of operation [8,9]. *In situ* magnetization dynamics can also be studied in the TEM, for example, with a specialized sample holder capable of applying a small field in the plane of the specimen [10 13]. Typically, the main objective lens of the microscope is switched off during these studies, and imaging is performed with the objective mini-lens, similar to the low-mag-mode in conventional TEM imaging. The reason for this is to avoid penetrating the sample with the strong field ~30 kOe (for a 300kV high-resolution TEM) of the main objective lens. Nevertheless, the remnant field from the objective, even while switched off, can produce fields at the sample region on the order of a few hundred Oersted. Certainly studies have exploited this fact to carry out *in situ* magnetization experiments by tilting the sample in this remnant field [14], however, one needs to know the field in order to calibrate the "applied field". In other cases, knowledge of the remnant field is important in order to address the

† Corresponding author: Building 480, Upton NY 11973, USA.
E-mail : schofield@bnl.gov

Contents

Cover micrograph

ADF-STEM images of $Al_{66}Cu_{17}Co_{17}$ decagonal quasicrystal, taken with JEM-2100F with Cs-corrector (Cs~0) and Maximum-entropy deconvolution map obdtained from Cs-corrected image (See page 14).

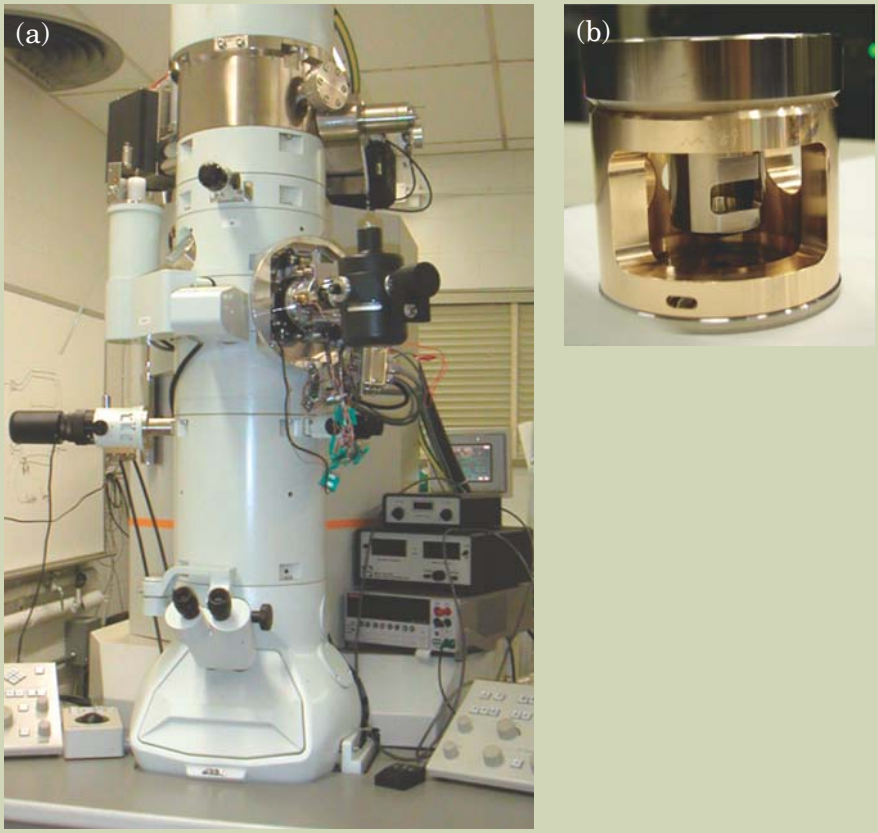

Fig. 1 (a) The JEM-2100F-LM at Brookhaven National Laboratory dedicated for high-performance magnetic imaging and holography. (b) The specially designed pole-piece of the long-focal-length objective-lens of the microscope.

effect of the microscope on the observed magnetic structure, and detailed characterization the objective lens (OL) field in a TEM dedicated to magnetic imaging is especially necessary.

The JEM-2100F-LM at Brookhaven National Laboratory, **Fig. 1(a)**, is specially designed and dedicated to quantitative magnetic imaging and holography, and is the first of its kind in the United States. The instrument is based on the JEM-2010F, a 200 kV TEM with a thermally assisted field-emission source. The unique feature of the JEM-2100F-LM is its long focal length (17 mm) objective lens shown in **Fig. 1(b)**. Since the OL is weakly excited and the specimen is located above the pole piece gap, the magnetic field at the sample area is significantly reduced to a few Oe when the lens is on (3-4 orders of magnitude smaller than a standard objective lens). A similar prototype objective lens was first installed and tested on a JEM-3000F microscope at Prof. Shindo's lab at Tohoku University in Japan. Although the pole-piece gap of our instrument is about 8 mm, the tilt angle of the sample holder is still limited to about 15° due to the narrow entrance of the pole-piece to reduce the leakage field. Since the objective lens is weakly excited, the lattice resolution of the microscope in its specification is 0.7 nm, although we have obtained test results better than 0.5 nm. The JEOL specification for the spherical aberration Cs of the machine is 95 mm, while for the chromatic aberration Cc is 16 mm. The other performance of the instrument is quite the same as a standard JEM-2010F, including a wide range of diffraction capabilities. This is particularly important for magnetic domain imaging, where we can easily observe the splitting of the central beam due to the variation in local magnetization, which is extremely useful for quantitative Foucault imaging. Our instrument is equipped with a 2 k × 2 k 16-bit CCD camera (14 μm pixel size) and a JEOL biprism (0.6 μm diameter, 180° rotation) for electron holography.

In the following section we present measurements of the fringe spacing, hologram width and fringe contrast as a function of biprism voltage for the HOLO-M mode setup of our JEM-2100F-LM. In the section of "Lorentz Imaging Characteristics", we present measurements of the objective lens spherical aberration and the minimum focal step that can be obtained with the microscope. In addition to the holography measurements, we describe in the section of "Objective Lens Field Measurements" a relatively simple modification to adopt a Hall probe to a standard analytic TEM holder that allows us to easily and accurately measure the OL remnant field in our JEM-2100F-LM. We characterize the field along two orthogonal directions, one perpendicular to the specimen plane and the other along the axis of the holder, and the spatial characteristics of the field profile for all stages of specimen entry into the column. We also measure the OL field in the sample region as a function of operating OL voltage, which is important for *in situ* magnetization experiments.

Holography Characteristics

In order to characterize the holography capabilities of the JEM-2100F-LM, the fringe-spacing, contrast, and hologram width were measured as a function of biprism voltage [15]. Here, "hologram width" refers to the FWHM of the interference patch, which differs from the well-defined concept of "interference distance" [16]. The results are shown in **Fig. 2** where data were collected in the HOLO-M mode of the microscope, and lens program determined and installed by the factory. The results in **Fig. 2** show the basic capabilities of the microscope where moderate improvement to the contrast might be expected with special attention paid to the room environment. All data were acquired using the now standard procedure of stretching the illumination along the perpendicular to the biprism [6].

For measurement of fringe spacing and contrast, holograms were recorded at a nominal 48 kX magnification, which corresponds to a calibrated pixel size of 0.22 nm on the 2 k × 2 k CCD camera. This corresponds to a sampling of about 6 pixels per fringe for the finest spacing. In this case, the transfer function of the CCD camera is likely to have an adverse influence on the measured contrast, although the detection properties of the CCD camera have not been measured. Regardless, **Fig. 2(a)** and (c) show that fringe spacing less than 1.5 nm can be easily achieved with a moderate contrast around 10-15%. The data shown in **Fig. 2** were recorded with 2 seconds exposure times during normal working hours. Longer exposures often resulted in significantly reduced contrast, and it is clear that the principle limitations to the holography performance are currently due to vibration and the room environment in general. This point, although far from being made for

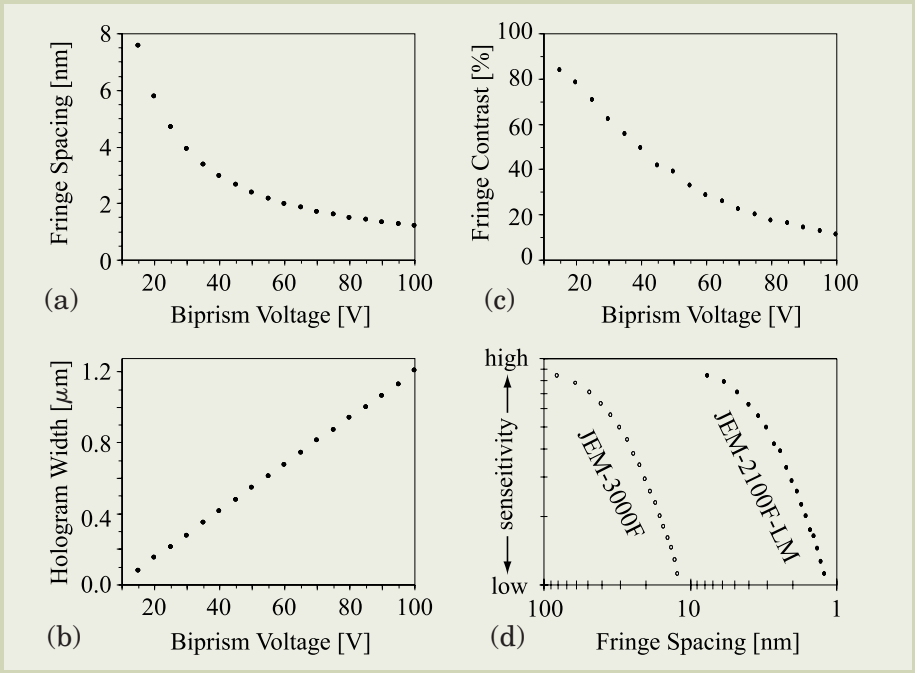

Fig. 2 Plots of (a) fringe spacing, (b) hologram width, and (c) fringe contrast as a function of biprism voltage. The sensitivity (fringe contrast) vs. fringe spacing (spatial resolution) for the JEM-2100F-LM is plotted (d) to show the overall performance of the holography capabilities, and compared directly to similar measurements made on our JEM-3000F, a high-resolution TEM operated in Lorentz mode for these measurements. The 2100F has an order of magnitude improvement in holography capabilities compared to the 3000F.

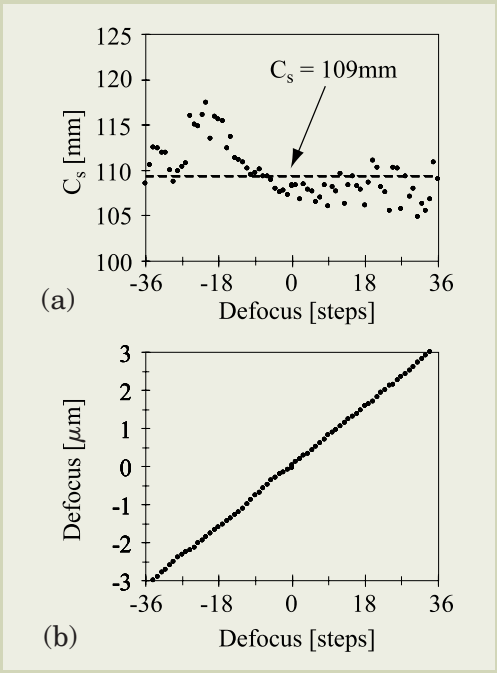

Fig. 3 Plots of (a) coefficient of spherical aberration, and (b) image defocus as a function of focal steps.

the first time, accentuates the importance of the laboratory environment in carrying out the most demanding experiments.

Figure 2(b) shows the measured hologram width as a function of biprism voltage. With the highest voltage where the fringe contrast is still reasonable, the hologram width is easily 1 μm. While a large field-of-view is potentially desirable, especially for magnetic studies where fringing fields can be quite long ranged, in this case the full 1 μm field-of-view cannot be completely utilized. This is due to limitations of the CCD camera. That is to say, a minimum magnification is needed to sample the fringes with enough pixels and simultaneously, enough total pixels on the camera are needed to cover the whole hologram. In our case, the magnification of the microscope is sufficient to sample the fringes with about 6 pixels per fringe, but then the field of the camera is only about 500 nm. This translates to a less-than-optimum setup of the recording conditions for biprism voltages larger than about 75 V for our microscope. Installation of a 4 k × 4 k CCD camera could provide better terms of sampling, utilizing the full field of the hologram.

Finally, consider the regime where the hologram width is roughly 1.5 times the CCD field-of-view for the highest available magnification. This corresponds to a situation where the Fresnel fringes from the biprism edge are largely outside of the recording region, and represents a regime where the sampling is roughly optimum given the constraints of the CCD size and holography geometry. For our setup, this corresponds to a biprism voltage around 70-75 V and, consequently, fringe spacing around 1.7 nm. Under these conditions, 5 nm spatial resolution may be easily obtained with roughly a 500 nm field-of-view. Further, the fringe contrast is 20-25%, which provides suitable phase sensitivity in general. For this microscope, these conditions would be considered characteristic of its median performance where higher resolution, higher sensitivity, or larger field-of-view cannot all be simultaneously obtained with any sort of ease. The interplay between spatial resolution and sensitivity (embodied by the holographic fringe contrast) is summarized in **Fig. 2(d)** where the fringe contrast (sensitivity) is plotted vs. the fringe spacing (resolution) for our JEM-2100F-LM. For comparison, similar measurements made on our JEM-3000F (a 300 kV high-resolution TEM) in Lorentz mode where the main OL is turned off and an objective mini-lens is used for image formation, are also shown in the figure. There is an order of magnitude improvement in holography performance between the two machines.

Lorentz Imaging Characteristics

Although the holography performance of the JEM-2100F-LM is generally satisfactory for a wide range of potential applications, one desires complementary capabilities for quantitative magnetic imaging. In particular, one may use through-focus techniques [17,18] to obtain quantitative magnetic information, but it is necessary to know the focal step between recorded images. Additionally, knowledge of the spherical aberration Cs of the imaging lens is required, either directly in the case of through-focus reconstruction, or indirectly for proper interpretation of results in the case of transport-of-intensity methods [19]. Knowledge of defocus and Cs is also important for holography applications involving high resolution since the image wave is reconstructed rather than the *object* wave. For this reason, we have measured Cs and the minimum focal step δf for our microscope.

A focal series of images were recorded at 200 k× magnification of holey carbon covering the focal range from −36 to +36 focal steps around zero defocus. For each image, numerical diffractograms were calculated, and all visible ring positions were measured. Between 9 and 35 ring measurements were obtained per image depending on the focus. Following well-documented methods, Cs and the absolute defocus for each image were obtained [8, 20-21]. **Figure 3(a)** shows the results of Cs measurement for each of the 73 images recorded in the series. During calculation of Cs for each image, which requires a linear fit to the ring positions, the R^2 value of the fit was noted and used as a weight when calculating the overall average Cs value. The result, as shown in **Fig. 3(a)** by the dashed line, is Cs = (108.7 ± 2.2) mm. This compares reasonably well with the value of 95 mm cited by the manufacturer JEOL.

Figure 3(b) shows results of the absolute focus obtained for each of the 73 through-focus images. The focus is linear over the range of ±3 μm with a focal step δf = (87.6 ± 1.4) nm. For quantitative Lorentz imaging, these characteristics of the focal behavior are satisfactory. The measured value of Cs = 109 mm gives a point-to-point resolution $r_{min} \cong 0.67\lambda^{3/4}Cs^{1/4}$ =0.77 nm [21]. In terms of holography applica-

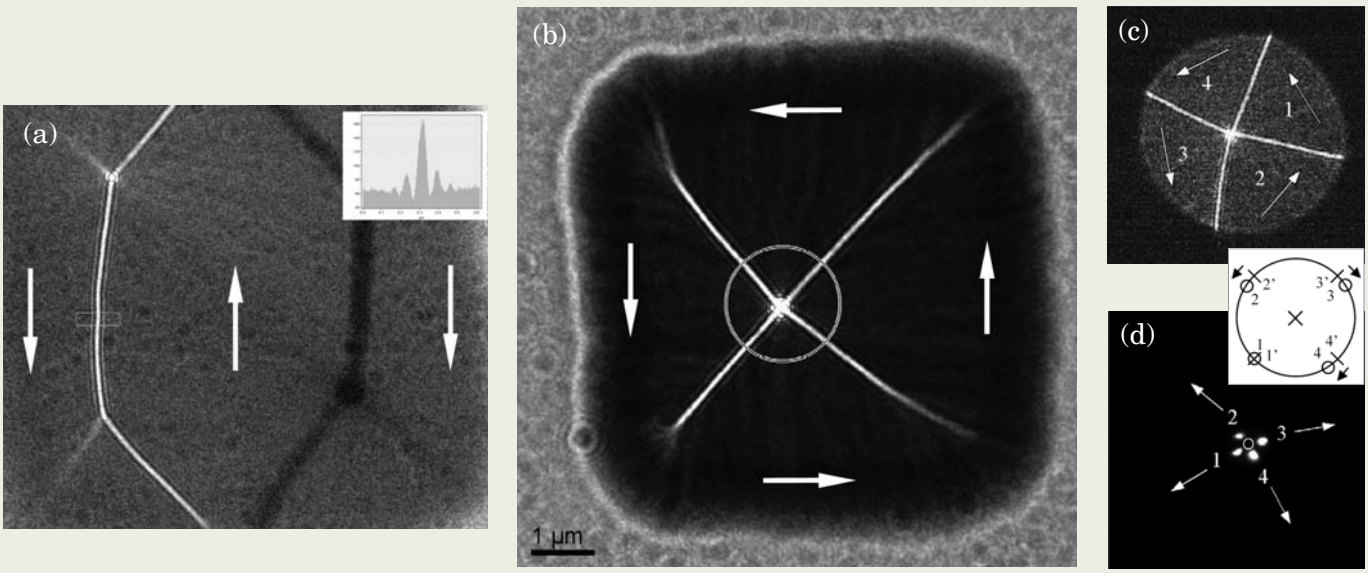

Fig. 4 Lorentz images of magnetic domains in square elements of Permalloy thin films. (a) Seven-domain configuration, where the vertical lines are 180° domain walls. The white line is a divergent domain-wall with a line-scan of its intensity shown in the inset, while the black line being a convergent domain-wall for this image focus. The arrows indicate the domain magnetization direction. (b) Vortex-domain configuration, where the white lines correspond to ~45° domain-walls with a vortex core (out-of-plane magnetization) at the intersection. (c) The area selected by the diffraction (SAD) aperture to form the diffraction pattern in (d), showing splitting of the transmitted beam. The position of the splitting spots allows us to determine the deviation from an ideal 45° magnetization near the vortex core. The domain label in (c) corresponds to the spot label in (d).

tions, this does not impose any limitations for the HOLO-M mode since the minimum fringe spacing that can be achieved only approaches 1 nm and, therefore, a resolution larger than 3 nm in the reconstructed wave.

As an example of the magnetic imaging capabilities of the JEM-2100F-LM, **Figs. 4(a)** and **(b)** are Lorentz images of magnetic domains in square elements of patterned Permalloy films grown by UHV e-beam deposition on SiN substrate using shadow-mask techniques. A line-scan of the image intensity, inset of **Fig. 4(a)**, across the divergent domain-wall (white line features in the image) clearly show oscillations in the Fresnel contrast,indicating the suitability of the image formation capabilities for possible quantitative studies. **Figure 4(b)** shows a closure domain structure in a similar Permalloy element where splitting of the transmitted beam due to the magnetic domain configuration is clearly seen in the diffraction pattern, **Fig. 4(d)**. **Figure 4(c)** indicates the area of the sample selected by the diffraction aperture, and this example illustrates some of the possible diffraction capabilities of the microscope. Combined with the Lorentz imaging capabilities and holography performance, several experimental techniques are available with the JEM-2100F-LM suitable for magnetic studies.

Objective Lens Field Measurements

The TEM holder that we adapted for the Hall probe modification was the Gatan half-finished heating holder without heating elements (Model 646), which is commercially available, and is a high-resolution double-tilt TEM holder (for a 2 mm pole-piece gap) with electrical through-put providing four terminals near the sample position for electrical contacts. The carriage that normally holds the TEM sample was removed for our modification to allow additional space to mount the Hall sensor accurately at the normal specimen position within the holder. **Figure 5** is a picture of our modified holder with the Hall sensor mounted at the sample position; additional details can be found in reference [22].

The objective lens of the JEM-2100F-LM has a long focal length that allows the sample to be situated above the pole-piece gap, in a "field-free" region, during normal operation. The manufacturer provides specification that the remnant field at the sample is ≤ 8 Oe. The pole-piece for this microscope is designed such that the strong field from the lens is routed around the region where the sample sits by mu-metal shielding. During insertion of the sample into the TEM column, the sample passes through an 8-mm gap in the shielding and, therefore, may be subjected to significant magnetizing effects. This is one of the features we wished to investigate with our adapted Hall probe, in addition to the field characteristics at the sample region during normal operation.

Measurements perpendicular to specimen plane

The first measurements were made with the Hall probe oriented in the modified holder so as to measure the field along the optic axis of the TEM, i.e., perpendicular to specimen plane. This is expected to be the principle orientation of the OL remnant field. We measured the field along various positions of sample insertion into the column with the OL on and as well as off, and **Fig. 6** shows the results of our measurements.

As evident in the figure, there is a significant difference for the 2100F-LM depending upon whether the OL is switched on or off. When the lens is excited to normal operating conditions, the sample is subjected to about 350 Oe field during insertion, presumably as it traverses the gap in the upper pole piece of the lens. With the OL off, however, only the remnant field of the lens is directed along the shielding and the sample is subjected to significantly reduced field about 18 Oe. This indicates that normal practice for loading a magnetic sample in this microscope should involve switching off the OL lens prior to insertion. With the sample fully inserted into the column, the measured field is 4 Oe when the OL is on, and 0 Oe when the OL is off. In this case, the manufacturer's specification of less than 8 Oe residual field at the sample position is confirmed.

We performed additional measurements with the Hall probe situated at the normal working position of the holder in the TEM column, and excited every lens in the microscope (except the OL, which we describe below) to their fullest extent in order to determine whether nearby lenses affected the field at the sample region. We did not measure any difference in the field at the probe position, regardless of lens excitation. Nor did we measure any difference as a function of sample position over the full extent of stage translation. As a function of sample tilt we measured a slight reduc-

tion of the field (from 4 Oe to 3.8 Oe) for high tilt above 20°. This is consistent with the remnant field aligned mainly along the optic axis of the microscope.

In terms of OL excitation, we indeed measure a field dependence on the lens potential used to excite the lens. **Figure 7** shows results of measurements made as a function of lens excitation. The standard lens excitation used for normal operation of the microscope corresponds to a lens potential of 0.76 V as read from the lens-data display of the TEM. With moderate lens excitation, we measure a roughly linear increase in the field generated at the sample area. While these excited OL conditions are far enough from normal operating conditions that one does not have to worry about generating above 4 Oe on the sample during conventional imaging and diffraction, it does allow for the possibility to carry out *in situ* magnetization experiments of the sort described in the introduction.

Measurements in the specimen plane

By rotating 90° the aluminum support holding the Hall probe, we were additionally able to measure the component of remnant OL field along the axis of the holder, i.e., one of the directions in the plane of the specimen. **Figure 8** summarizes the measurements made, and there is again a significant difference depending whether the OL is on or off. As seen in the figure, when the OL is switched off, the measured field peaks at about 18 Oe and switches from an initial negative polarity (directed away from the column center) when the sample insertion begins, to a positive polarity (directed toward the column center) when the sample passes through the mu-metal shielding. Still, the field component is relatively small, although the same magnitude as the perpendicular component. This further supports the conclusion that the OL lens should be turned off prior to sample insertion in order to minimize magnetizing effects from the OL field.

With the OL turned on, the field component along the holder axis is quite large on average, switching polarity relative to the probe during the insertion process. We note that the rightmost measurement (at 7 cm distance in **Fig. 8**) corresponds to the probe located in the load-lock of the specimen exchange, which explains why the measured field is not zero. Nevertheless, our results indicate that this in-plane component is just as significant as the out-of-plane component during sample insertion regardless of whether the OL lens is on or off, albeit the net field is much smaller with the lens turned off. When the sample is in the normal operating position, i.e., fully inserted, we measure about 1.6 Oe for the in-plane field component. Comparing this to the 4 Oe vertical component, it appears that the residual field on the sample cannot be considered essentially vertical, even if the main component is indeed along the optic axis.

Holography Examples

The unique capabilities of our JEM-2100F-LM allow us to investigate magnetic structures in comparatively low field, about 4 Oe vertical residual field compared to ~200 Oe in a conventional microscope when the objective lens is switched off. While the principle utility of the JEM-2100F-LM is for application to magnetic studies, we illustrate the comparatively high resolution and sensitivity of the holography capabilities of this microscope with two examples. The first example, while purely an electrostatic problem involving measurement of charged latex spheres, nicely illustrates nevertheless the sensitivity of the microscope.

Figure 9 shows holography results from a 94 nm latex sphere dispersed on holey carbon substrate. The cosine map of the reconstructed phase, **Fig. 9(a)**, is amplified 16× to show the fringing field associated with the charged sphere. The phase was reconstructed from a hologram recorded with 1.97 nm interference fringes and 18% contrast in the sample. A profile of the circularly averaged phase shift across the sphere is shown in **Fig. 9(b)**, along with the calculated phase shift shown as a red line. The best-fit parameters of the calculated phase shift gives a mean inner potential of 5.4 V and 65 electrons of charge distributed on the surface of the latex sphere. In this experiment, a much smaller charge than 65 electrons could have been detected (at least by a factor of 2), but serves in any case to illustrate the sensitivity of the microscope when combined with theoretical modeling and interpretation.

With the low-field characteristics of the specially designed pole-piece of the JEM-2100F-LM, combined with the capability to carry out holography experiments at comparatively high spatial resolution, we have initiated study of the structure of vortex cores in magnetic nanodisks. The vortex core is a nanometer-sized region of vertical magnetization that forms at the center of the vortex closure-domain, and is typical of nanodisks in a certain size range. While this phenomenon was experimentally observed using surface-sensitive spin polarized scanning tunneling microscopy [2], a great deal remains unknown, including the degree of extension of the vortex core as a function of the anisotropy of external parameters and disk size, as well as the transition of spin moments from in-plane to out-of-plane near the core due to quantum mechanic exchange.

Preliminary holography experiments involving measurement of the vortex core structure in thin Permalloy disks are summarized in **Fig. 10**. Samples consisted of 1 μm patterned Permalloy disks, about 20 nm thick, deposited on holey carbon substrate using shadow mask techniques by UHV e-beam deposition. Holography experiments were carried out with a biprism voltage of 110 V giving 1 nm interference fringes and about 5-10% contrast in the sample. In **Fig. 10**, the phase profile retrieved from holography (black line) is obtained after circular averaging about the core center, and is compared with a simulated profile where the core structure is neglected (red). In the inset, a more physical phase profile (blue) is matched against the data showing that near the core the signal drops due to the associated vertical component of the magnetization, m_z. In modeling the vertical component of the vortex core we took the ansatz $m_z=[1+(r/r_0)^2]^{-\alpha}$ where r is the distance from the core center. Best fit to the holography data gives r_0=28 nm and α=7/3. The FWHM of m_z with these parameters is 33 nm providing a characteristic size of the vortex core region in these particular Permalloy elements.

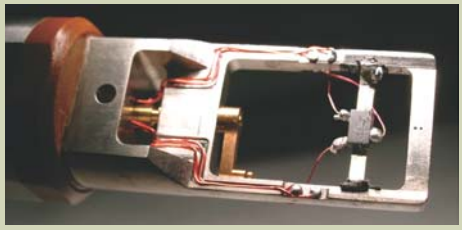

Fig. 5 Our modification to a standard double-tilt TEM holder with electrical through put allowing for a Hall probe to be mounted in the normal sample position. This modification allows accurate measurement of the OL field generated at the sample location.

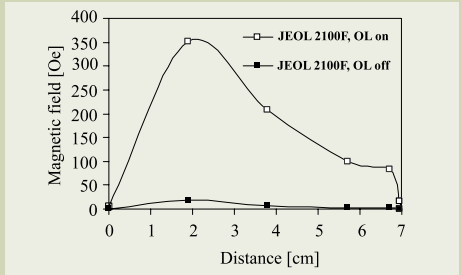

Fig. 6 Magnitude of the magnetic field profile as a function of distance from the center of the TEM column for the JEM-2100F-LM. (The lines in the plot are only to guide the eye between measured data points.) Independent measurements were made with the OL on (open squares) and off (closed squares).

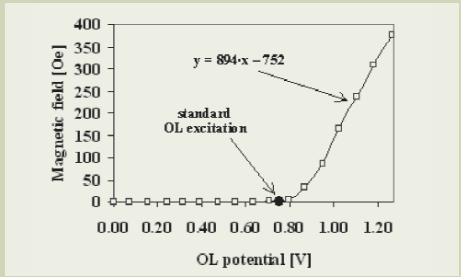

Fig. 7 Field measured along the optic axis as a function of OL excitation in the JEM-2100F-LM. (The line in the plot is only to guide the eye between measured data points.) The standard lens excitation for normal operation corresponds to 0.76V. Above about 0.85V, the field at the sample is roughly linear with OL excitation.

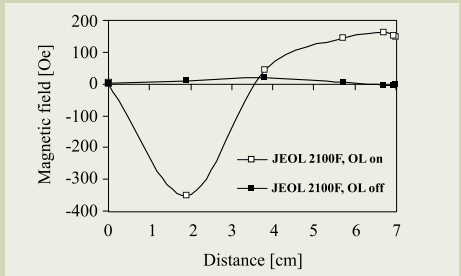

Fig. 8 Magnetic field profile along the holder axis as a function of distance from the center of the TEM column for the JEM-2100F-LM. (The lines in the plot are only to guide the eye between measured data points.) Independent measurements were made with the OL on and off. A positive polarity in the measured value corresponds to field component directed towards the center of the column, while a negative polarity indicates an outward direction.

Summary and Conclusion

While we continue with experiments and analysis of vortex core structure, the simple examples described above, including charge measurement on latex spheres, illustrate the unique holography capabilities of the JEM-2100F-LM for both electrostatic and magnetostatic studies. In characterizing the holography performance of the JEM-2100F-LM, we have found it easily suited for magnetic studies requiring a large field-of-view (about 500 nm) while maintaining high spatial resolution (about 5 nm) in the reconstructed phase. Measurement of the spherical aberration coefficient of the specially designed objective lens, which agrees with the manufacturer's claim, and calibration of the minimum focal step allows for the possibility for quantitative Fresnel imaging techniques, including through-focal techniques, that can supplement electron holography studies. During measurement of the objective lens field of the microscope we found that several hundred Oersted can be applied to the sample, if desired, which depends linearly on the moderate lens excitations we measured. Overall, the residual field on the sample due to the specially designed pole-piece is about 4 Oe under normal operating conditions, suitable for a wide range of studies involving magnetic materials. Combined with theoretical developments, such experimental capabilities will offer an opportunity to gain new essential scientific knowledge on technologically important magnetic structures at the nanoscale.

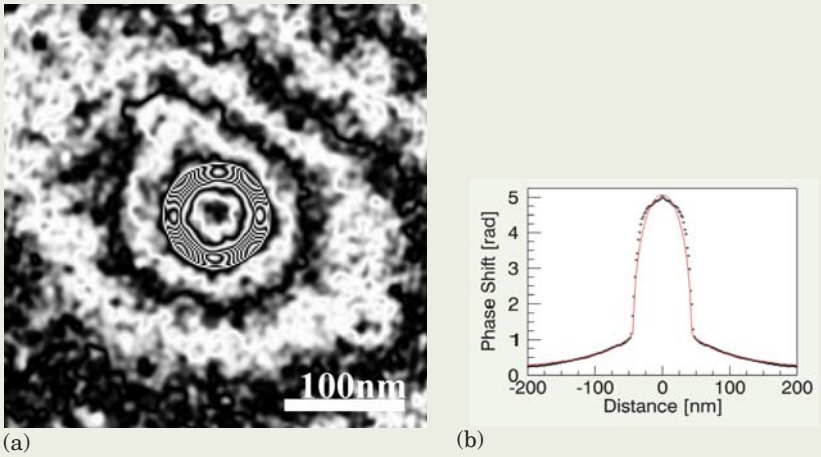

Fig. 9 (a) cosine of 16× amplified reconstructed phase from latex sphere, and (b) calculated phase shift (red line) for a sphere with 5.4V inner potential and 65 electrons of charge distributed on its surface.

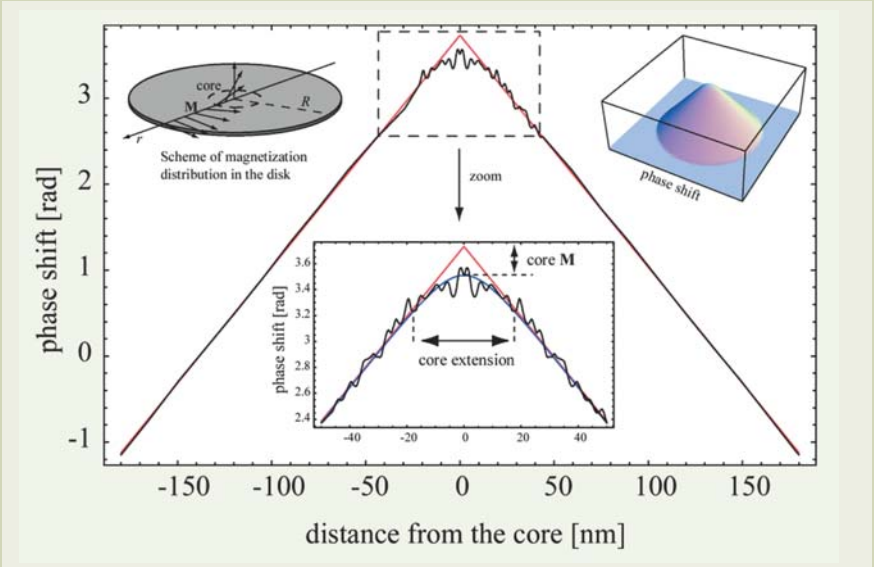

Fig. 10 Circularly averaged phase profile (black line) from electron holography of a magnetic vortex formed from closure domain structure in a 20-nm Permalloy disk compared with simulated profile where the vortex core structure is neglected (red). In the inset, a more physical phase profile (blue) is matched against the data showing that the experimental signal drops due to the associated loss of the vertical component of magnetization. Top left: scheme of the magnetization distribution in a circularly magnetized disk; Top right: electron-optical phase shift associated with the disk.

Acknowledgement

We gratefully acknowledge essential advice from Giulio Pozzi in the measurement of geometrical and electron-optical parameters of the microscope. We also thankfully acknowledge the contribution of Giorgio Matteucci in the electron holography research of charged particles. Work at Brookhaven National Laboratory was supported by the U.S. Department of Energy, Office of Basic Energy Science, under Contract No. DEAC02-98CH10886.

References

[1] M. De Graef and Y. Zhu (Eds.) Magnetic imaging and its application to materials, Academic Press, London, 2001.
[2] Y. Zhu (Ed.) Modern techniques for characterizing magnetic materials, Springer, Berlin, 2005.
[3] D. Gabor, *Nature* **161** (1948) 777.
[4] A. Tonomura, Electron Holography, 2nd Ed., SpringerVerlag, Berlin Heidelberg, 1999.
[5] Y. Aharonov and D. Bohm, *Phys. Rev.* **115** (1959) 485.
[6] E. Volkl, L.F. Allard and D.C. Joy (Eds.) Introduction to Electron Holography, Kluwer Academic, New York, 1999.
[7] W. J. de Ruijter and J. K. Weiss, *Ultramicroscopy* **50** (1993) 269.
[8] D. B. Williams and B. C. Carter, Transmission electron microscopy : a textbook for materials science. (Plenum Press, New York, 1996).
[9] Magnetic imaging and its applications to materials. (Academic Press, San Diego, 2001), pp.xvi, 295 p., [216] p. of plates.
[10] T. Uhlig, M. Heumann, and J. Zweck, *Ultramicroscopy* **94** (3-4), 193-196 (2003).
[11] G. Yi, W. A. P. Nicholson, C. K. Lim et al., *Ultramicroscopy* **99** (1), 65-72 (2004).
[12] J. W. Lau, M. A. Schofield, Y. Zhu et al., Proceedings of Microscopy and Microanalysis 9 (2), 130 (2003).
[13] J. W. Lau, M. Beleggia, M. A. Schofield et al., *J. Appl. Phys.* **97** (10), 10E702 (2005).
[14] J. W. Lau, J. K. Bording, M. Beleggia et al., *Appl. Phys. Lett.* **88** (1), 012508-012503 (2006).
[15] M. A. Schofield, M. Beleggia, Y. Zhu and G. Pozzi, submitted to Ultramicroscopy.
[16] G. Matteucci, G.F. Missiroli and G. Pozzi in Advances in imaging and electron physics 99, 171, (P.W. Hawkes ed., Academic Press, 1998).
[17] D. Van Dyck, M. Op. de Beeck and W. Coene, *Optik* **93** (1993) 103.
[18] S. Bajt, A. Barty, K.A. Nugent, M.R. Mc Cartney, M. Wall and D. Paganin, *Ultramicr.* **83** (2000) 67.
[19] M. Beleggia, M. A. Schofield, V. V. Volkov and Y. Zhu, *Ultramicroscopy* **102** (2004) 37.
[20] O. L. Krivanek, *Optik* **45** (1976) 97.
[21] P. Buseck, J. Cowley and L. Eyring (Eds.), HighResolution Transmission Electron Microscopy and Associated Techniques, Oxford University Press, Oxford, 1992.
[22] J. W. Lau, M. A. Schofield and Y. Zhu, *Ultramicroscopy* **107** (2007) 396.

Improvement of Reflection Electron Microscopy: LODREM

J. J. Métois, P. Müller *

Centre de Recherche sur la Matière Condensée et les Nanosciences, UPR CNRS associé aux universités Aix Marseille II et III, Aix-Marseille Université
***Campus de Luminy, Case 913, F-13288 Marseille Cedex 9, France**
also Université Paul Cézanne-Aix Marseille III

Owing to its surface sensitivity, Reflection Electron Microscopy (REM) is widely used to study surface structure and surface dynamic processes. However, because of the glancing conditions, REM images are severely foreshortened in one direction. We show that a simple modification inside the column of the microscope allows a true correction of the distortion. We call the new method we describe Low Distortion Reflection Electron Microscopy and give it the acronym LODREM.

Introduction

As soon as it was possible to observe surfaces in the direct space with rapid image acquisition and high surface sensitivity, studies of surface dynamic processes largely improved. Since Ruska seminal works [1], two techniques of electron microscopes specific for surface studies have been successively proposed: Reflection Electron Microscopy (REM) proposed in 1933 [1] but only available in 1978 [2], and more recently Low Energy Electron Microscopy (LEEM) proposed in 1962 [3] and available in 1985 [4].

In the REM method electrons of high energy (100-200 kV) are used so that surface sensitivity is only obtained by working at glancing incidence. More precisely, a RHEED pattern of the surface is formed at the back-focal plane of the electronic lens and the REM image, obtained after selection of a RHEED spot by an objective aperture, is projected on the microscope screen. Working with glancing incident electrons allow to be surface sensitive, but the "price to pay" is a severe foreshortening of the images so that the magnification is roughly 50 times higher in the direction perpendicular to the electron beam than in the direction of the electron beam. In spite of this image distortion, REM has been successfully used to study structural phase transitions, adsorption processes, crystal growth or evaporation, nanostructure formation.

Our task in this short paper is to show how some simple improvement of the microscope may be used to enhance REM capabilities.

Campus de Luminy, Case 913, F-13288 Marseille Cedex 9, France.
also Université Paul Cézanne-Aix Marseille III
E-mail : muller@ormch.univ-mrs.fr

Improvement of the REM Capabilities

As above-mentioned, in REM the image is foreshortened by a factor $\sin\theta$ where θ is the incidence angle of impinging electrons onto the surface. The exact value of the foreshortening depends upon the order of reflection used for imaging but in classical conditions roughly oscillates between 40 and 70. In our usual conditions we have a factor of 50 so that the magnification rate of the image is 50 times lower in the direction parallel to the electron beam than in the direction perpendicular to the electron beam. The distorted images may be numerically corrected, but the finite size of the pixels limits the final resolution so that numerical correction of REM images is not efficient to restore the original object with a good accuracy (see **Figure 1**). An alternative which would avoid any numerical correction would be to set upright the electronic image in the microscope before the screen or directly on the screen. In fact the simple way is to use a geometrical correction of the distortion by tilting the screen on which the image is projected. In other words a simple tilt of the screen should be enough to compensate the distortion due to the glancing incidence. However such a geometrical compensation can only be used when the following conditions are fulfilled:

(i) The tilt screen axis has to be parallel to the high magnification sample tilt axis. Indeed because of the image rotation associated to the electronic magnification change encountered the microscope JEOL JEM-100C we use, the position of the tilt axis of the screen, necessary for the geometrical correction, depends upon the amplitude of the electronic magnification. Thus two movements of the screen are needed. The first one consists in putting in coincidence the tilt axis of the screen with the high magnification axis (the rotation tilt axis of the sample). The second one is to tilt the screen from its initial position towards the grazing incidence θ' which allows a complete geometrical correction by fore-extending the image by a factor $\sin\theta$' which corrects the foreshortening due to the grazing incidence $\sin\theta$ *1 onto the sample. The correction should be complete for $\theta=\theta$'.

(ii) The depth of focus has to be large enough to insure good focus conditions on the whole screen. Owing to the high total magnification used in electronic microscopes the depth of focus (which must not be confused with the depth of field) practically is infinite so that it is possible to tilt the screen without introducing any additional blurring of the projected image.

(iii) The electronic intensity must be sufficient to compensate the intensity loss due to the glancing incidence on the sample and on the screen. In our configuration the intensity current only reaches 10^{-12}A cm^{-2} which is not enough to obtain a good image in video mode. We have thus substituted a CCD electron multiplier to our classical analogical camera. More precisely we have used a C9100 series camera of Hamamatsu but we have kept the initial fluorescent screen. Unfortunately, working in grazing incidence enhances the screen defects. Another solution should be to acquire a completely out-of-focus image that contains no information about the sample structure but only overall screen intensity variation then to correct pixel by pixel the image.

Towards Low Distortion Reflection Electron Microscopy (LODREM)

When the former conditions are fulfilled,

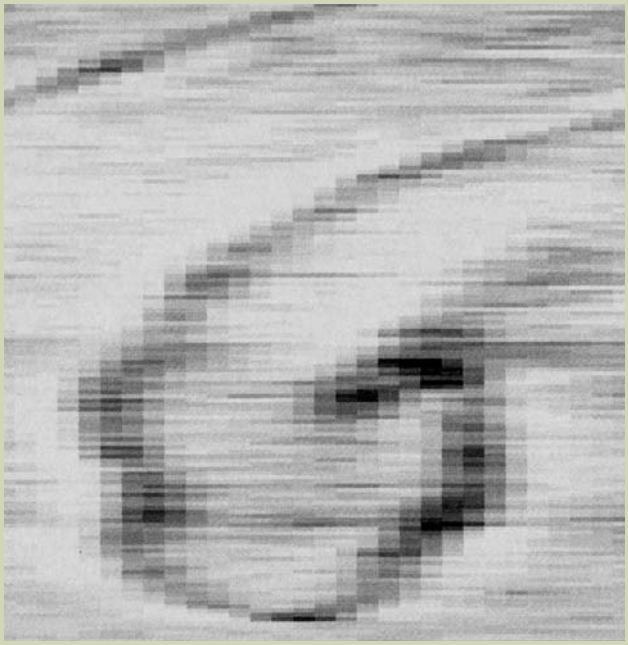

Fig.1 REM image of a spiral of evaporation on a Si(111) surface obtained after numerical correction. The pixel size limits the resolution [5].

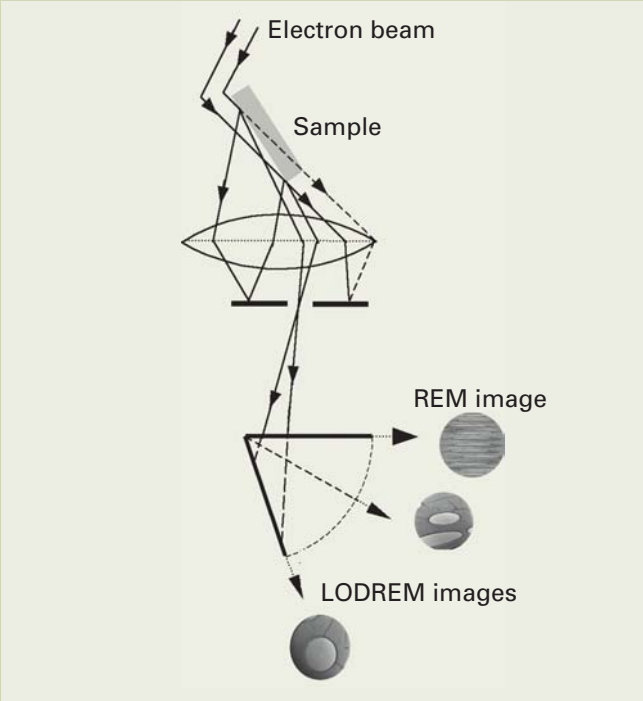

Fig.2 Schematic ray diagram for REM and LODREM conditions. On the right are given the REM and LODREM images of holes in a Carbon membrane.

the new above-mentioned microscope configuration allows to obtain low distorted or non distorted images and thus gives a second birth to REM applications so that we do not hesitate to give a new acronym for Low Distortion Reflection electron Microscope (LODREM) [5].

In **Figure 2** is reported in a schematics way the ray diagram for REM and LODREM configurations. In addition, we report on the right part of the scheme the transmitted image formed by an array of circular holes in a graphite membrane (the sample) the normal of which forms an incident angle of 85° with the incident electrons. Because of the foreshortening, the image in the usual REM plane is formed of several elliptic holes (see REM image in **Figure 2**), but a simple tilt of the screen is enough to restore the good circular shape. Obviously when increasing the screen angle θ', the ellipsoid shape evolves towards a circular form (reached for $\theta=\theta$') then must evolve again towards an elliptic shape for $\theta' > \theta$. The non distortion condition is thus obtained when we observe the largest structure in the direction perpendicular to the screen axis. As an illustration we report in **Figure 2** two LODREM images obtained with two different screen angles. In the intermediate image obtained at $\sin(25°)\approx 0.4$, the holes are still a bit elliptic, while in $\theta\approx\theta'\approx 85°$ conditions the circular shape is recovered*[2].

The principle of LODREM correction is perfectly illustrated in **Fig 3** where are reported the images of a spiral of evaporation recorded for various increasing screen angle. The first image is close to REM conditions, the last one corresponds to LODREM conditions ($\theta\approx\theta'$).

In **Figure 4** are reported some illustrations of the LODREM capabilities. For this purpose we give in **Figure 4a** a typical REM image of a Si(111) surface where can be recognised monoatomic steps and step bunches. At the same in **Figure 4b** is given a REM image of a spiral of evaporation due to a screw dislocation. In **Figure 4c** is shown a LODREM image of a part of a Si (111) surface exhibiting a train of monoatomic steps, while in **Figure 4d** is shown a LODREM image of a spiral of evaporation. Comparing REM and LODREM images is enough to understand the new capabilities offered by LODREM with respect to REM. In order to illustrate the screen angle effect we give in **Figures 4e** and **4f** two images of the same zone recorded in true LODREM condition that means when the screen and the sample angle are identical (**Fig .4f**) then when the screen angle is smaller (5°) than the sample angle so that a weak distortion remains (**Fig. 4e**).

Conclusion

In 1993 the review paper of Yagi [6] concluded that "correction to foreshortening in REM images are important to get a quantitative characterization of the surface topology". We have demonstrated that a simple geometrical modification of the microscope allows such a physical correction, avoiding any numerical correction of the image for which the pixel size is the limiting factor so that we do not hesitate to give a new acronym for Low Distortion Reflection Electron Microscope (LODREM). Beyond the improvement of REM (towards LODREM), we believe that such a system could also be very useful for other microscopic techniques such as TEM for which it would allow (i) to obtain a multiscale image and (ii) to control the shadow effect. More precisely the multiscale image could give access to various scales of periodicity and/or curvature on a given sample while the controlled shadow effect (by simultaneous tilt of the sample and the screen) could allow to observe simultaneously the lateral and vertical size distribution of a collection of 3D objects deposited on a surface.

Acknowledgements

We gratefully thank B. Detailleur (TCN CNRS) for having performed all the mechanical improvements of the REM microscope as well as B.Ranguelov from Bulgarian Academy of Science. Partial financial support by the Bonus Qualité Recherche of the University Paul Cézanne is also acknowledged.

References

[1] E. Ruska Z. *Phys*., **83**, 492 (1933).
[2] K.Yagi, K.Takayanagi, K.Kobayashi, N.Osakabe, Y.Tanishiro and G.Honjo, Proc. 9th cInt. Cong. On Electron Microscopy, Toronto, vol1, 458 (1978).
[3] E. Bauer, in Fifth Intern. Congress for Electron Microscopy (Breese, Jr Sydney S; Editors) New York Academic press (1962) D-11-12.
[4] W. Telieps and E. Bauer, *Ultramicroscopy*, **17**, 57 (1985).
[5] P.Müller and J.J.Métois, *Surf. Sci.*, **599**,187 (2005).
[6] K.Yagi, *Surf. Sci. Rep*., **14**, 305 (1993).

*[1] The incidence angle is the angle between the surface plane of the sample and the incidence ray. In other words θ is the tilt angle between the sample and the microscope axis. Similarly, θ' will be the angle between the screen and the incident ray.

*[2] Obviously while in the REM image one can observe several, but deformed, holes, in the LODREM image only one circular hole is observed.

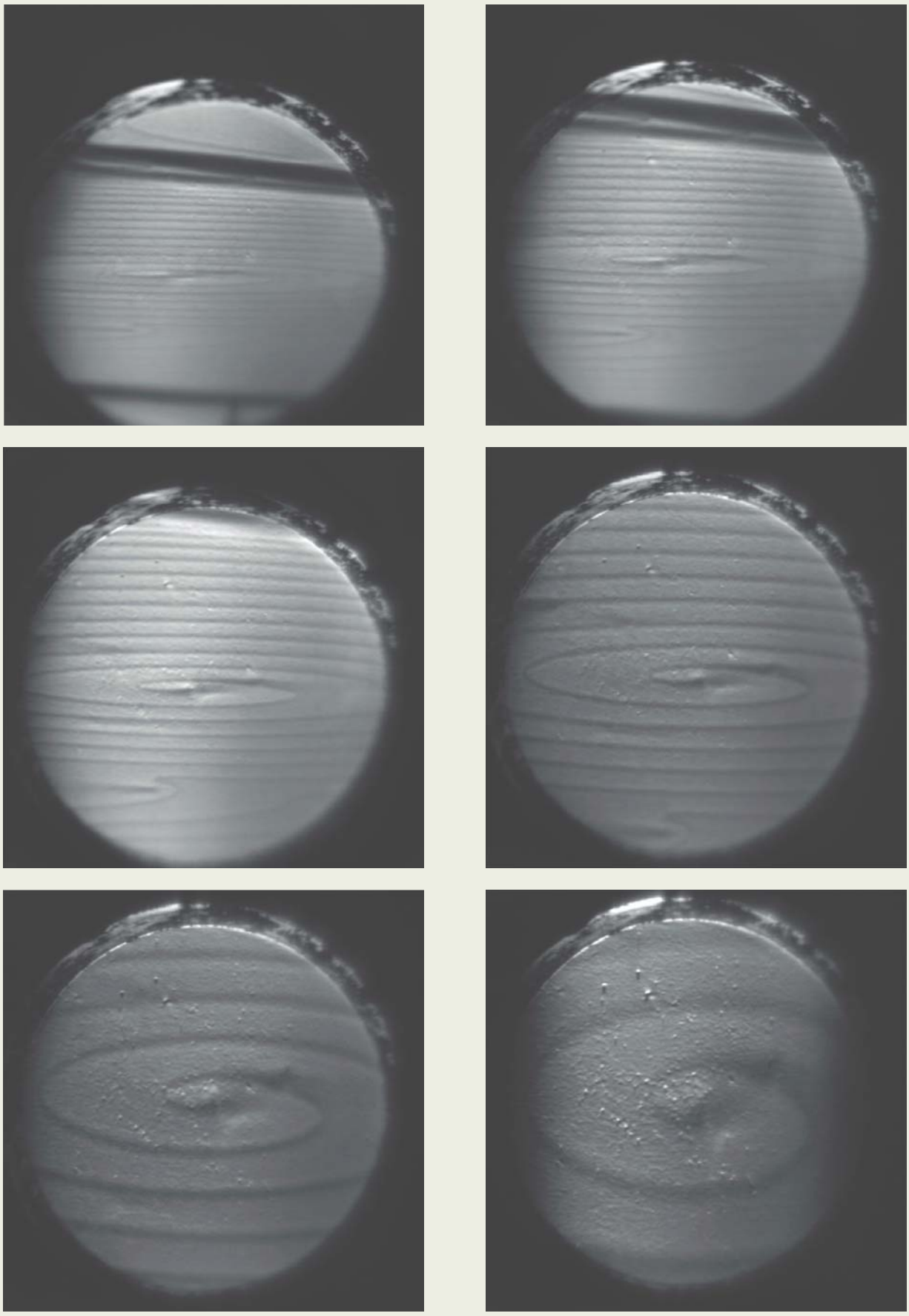

Fig . 3 Images of a spiral of evaporation recorded by for various increasing screen angle. The first image is close to REM conditions (weak θ' angle), the last one corresponds to LODREM conditions ($\theta \approx \theta$'). In this last case, because of the grazing incidence the screen defects are visible. The horizontal dimension of each image is roughly 10 μm.

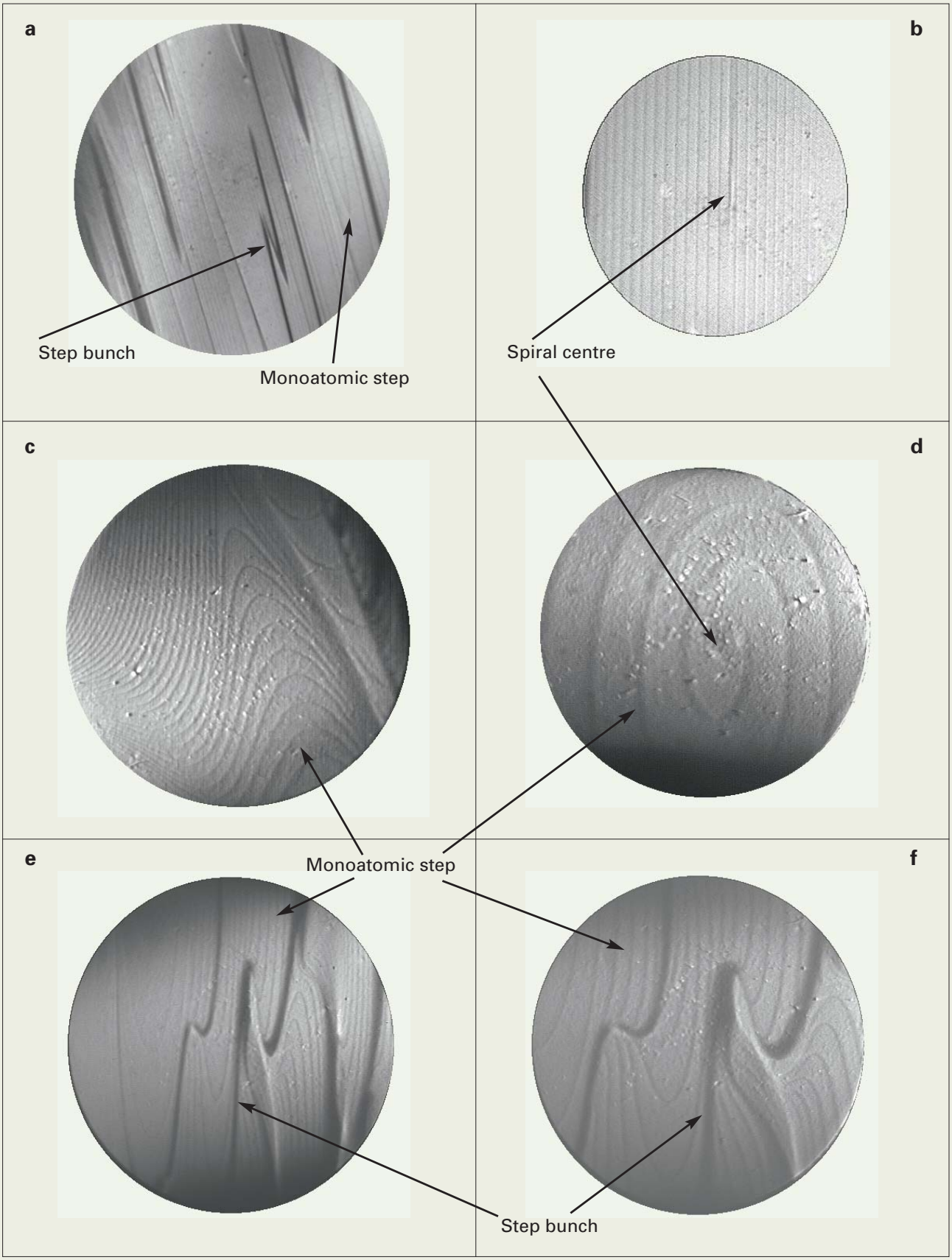

Fig.4 Comparison between typical REM images (a and b) and LODREM images (c-f) obtained on Si(111) surfaces: (a) Typical REM image with monoatomic steps and step bunches, (b) REM image of a spiral of evaporation. (c) LODREM image of monoatomic steps, (d) LODREM image of a spiral of evaporation, (e) and (f) typical LODREM images of a Si surface with monoatomic steps and step bunches. The only difference between the two last images is the screen angle. In image (e) the screen angle is smaller than the sample angle so a weak distortion remains. It is not the case in figure (f) where the two angles are identical. The vertical dimension of each image is roughly 2 μm.

Where Are the Atoms in Quasicrystals?
- direct imaging by aberration-corrected STEM -

Eiji Abe

Department of Materials Engineering, University of Tokyo

The scanning transmission electron microscope (STEM) with an annular dark-field (ADF) detector provides atomic-resolution incoherent images, whose resolution is dominated, to a good approximation, by the size of convergent electron beams. Improving a spherical aberration of microscope objective lenses has been successful in converging the beam into sub-Å scale, achieving a remarkably better resolution for STEM. Here we demonstrate the performance of aberration-corrected STEM based on direct imaging of a complicated quasicrystalline compound, which is composed of relatively light (aliminium) and heavy (transition metals) elements.

Introduction

Quasicrystals are aperiodic solids that are characterized by their rotational symmetries being incompatible with conventional periodic lattice order; e.g. icosahedral symmetry in three dimensions and ten-fold symmetry in the plane. At present both thermodynamically metastable and stable quasicrystalline phases can be formed in a variety of metallic alloys, and certain stable phases can be grown into a single grain several millimeters (**Fig.1(a)**) or even centimeters in size. Even though their diffraction peaks appear to be not periodic, some highly-perfect quasicrystalline materials exhibit quite sharp diffraction peaks (**Fig.1(b)**), whose sharpness is comparable to that from nearly-perfect crystals such as silicon within the limits of instrumental resolution. This is quite striking fact for the crystallography, since the diffraction peaks represented by delta-functions had been believed to be possible only for periodic crystals. Nowadays we interpret this novel, interesting long-range order as true quasiperiodicity, which is not a simple periodic arrangement of a unit cell as a normal crystal, but instead is composed of an array of two or more unit cells as represented by the Penrose tiling (**Fig.1(c)**). Quasiperiodicity is a precisely defined aperiodic order, and we particularly note that the term quasicrystal is a short form for 'quasiperiodic crystal'; it never means an imperfect, pseudo-crystal as one might guess from the expression. Rather, quasiperiodicity represents just as rigorous an ordering as periodic order.

"Where are the atoms?" – soon after the announcement of a quasicrystal discovery [1], Bak raised a simple but fundamental key question regarding its atomic structure [2]. The answer for this question is not so straightforward; one may face multiple solution problems when trying to tune the quasiperiodic atomic configurations solely based on the standard x-ray diffraction experiments. We describe quasicrystal structure according to a quasiperiodic lattice (quasilattice), as exemplified by the Penrose pattern composed of two different rhombic tiles those arrayed with matching rules. Variant quasilattices can also be constructed by using these two rhombic tiles (without matching rules), and each of them gives rise to identical diffraction intensity distributions. This is due to a local isomorphism of a quasilattice, and hence the multiple structural solutions, differing in tile (cluster) arrangements and local atomic configurations, intrinsically occur from the diffraction data [3]. Atomic-resolution electron microscope images are unique in this regard, as they directly represent the *local* atomic structure and can therefore investigate details of the cluster arrangements and relevant local atomic configurations. We below describe a recent remarkable progress of atomic imaging by STEM, which have been achieved through aberration correction of the beam convergent lens [4, 5].

Incoherent Imaging in STEM

Annular dark-field (ADF) STEM provides atomic-resolution images by effectively illuminating each atomic column one-by-one as a finely focused electron probe scans across the specimen, generating an intensity map at the ADF detector. The atomic images may, to a good approximation, be interpreted assuming independent scattering from individual atomic columns, and hence the observed intensity distribution ($I(\mathbf{R})$) can be simply described by a convolution between a probe-intensity function ($P(\mathbf{R})$) and a scattering object function ($O(\mathbf{R})$) [6] (the mathematical definition of incoherent imaging: **Fig. 2**);

$$I(\mathbf{R}) = O(\mathbf{R}) \otimes P(\mathbf{R}) \qquad \text{- (1)}$$

It should be noted that the STEM incoherent imaging becomes possible only when the ADF detector is located at sufficiently high-

7-3-1, Hongo, Bunkyo-ku, Tokyo, 113-8656, Japan
E-mail: abe@material.t.u-tokyo.ac.jp

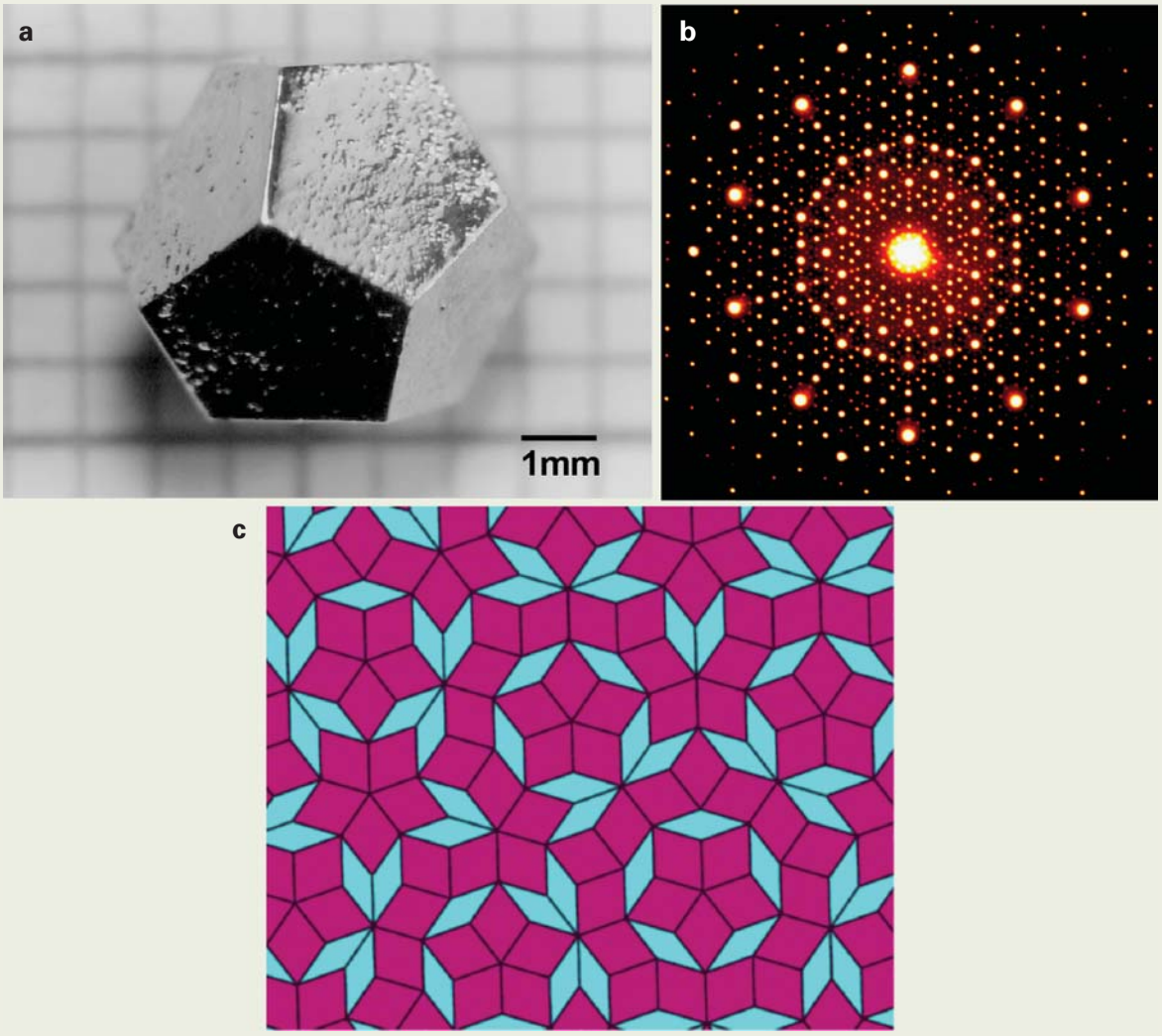

Fig. 1 (a) Optical micrograph of a large dodecahedral grain of $Zn_{56.8}Mg_{34.6}Ho_{8.7}$ quasicrystal successfully grown from the melt via slow-cooling method (courtesy of Ian Fisher and Paul Canfield [11]). (b) Electron diffraction pattern taken along the tenfold symmetry axis of the $Al_{72}Ni_{20}Co_8$ decagonal quasicrystal, one of the best quasiperiodic ordered materials available today. (c) Penrose tiling, which explains all structural fundamentals seen in a quasicrystal. Two rhombic tiles are arranged in accordance with the *matching rule*; this is a strict mathematical rule that forces the tiles to join uniquely into a perfect quasiperiodic pattern.

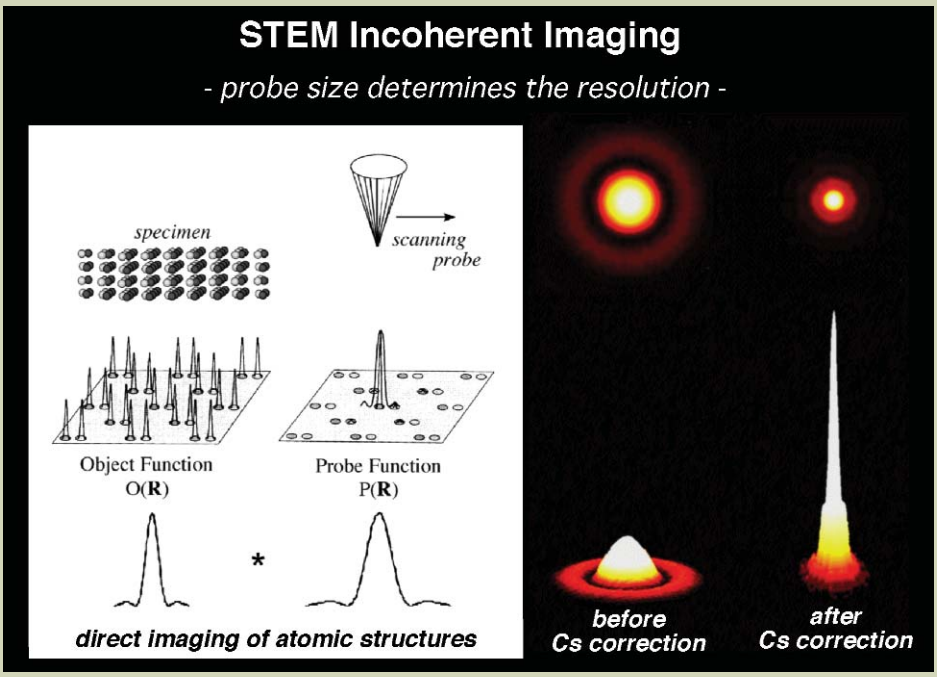

Fig. 2 Schematic illustrations of incoherent imaging in ADF-STEM (left) and calculated probe intensity distributions before and after aberration correction (right).

angle scattering ranges. Electron channeling along the atomic columns is achieved through the effective excitation of 1*s* Bloch state due to dynamical diffraction; though, this is not enough. To realize as if the individual columns are to be illuminated independently (Eq. (1)), *filtering* by the ADF detector to reduce the effects of other excited Bloch states, e.g. 2*s* state, is essentially necessary [7]. This Bloch state filtering to select 1*s*-state becomes significant at high-angle scatterings, and therefore the ADF detector is needed to be placed at those scattering ranges. At high-angle scatterings, the detector captures mostly the thermal diffuse scattering (TDS), whose intensity is well described by the TDS cross section (σ_{TDS}) that contributes to the ADF detector range. Since the TDS intensity is almost proportional to the square of atomic number Z, ADF-STEM imaging provides a significant Z-dependent contrast (Z-contrast) [6]. We here note that TDS described by σ_{TDS} is sufficient for estimating the integrated intensity reaching the detector, although it does not reflect any fine details of the high-angle diffraction pattern including Kikuchi lines (*incoherent* estimation of the scattering intensity).

As described above, Z-contrast is an unavoidable consequence of the incoherent STEM imaging. Incoherent STEM images are an ideal intensity map that represents directly the specimen scattering power, which can be intuitively inverted to the $O(\mathbf{R})$ that represents atomic structures. However, resultant structural information have been limited to mostly the heavy atom positions due to its Z-contrast nature, even when the simultaneous imaging of both the light and heavy atoms is required for the determination of complex compound structures. After the spherical aberration (Cs) correction of the objective lens in STEM, the available electron probe, $P(\mathbf{R})$, is now much sharper and brighter than before (**Fig.2**, **right**). This enables the ultrahigh-resolution incoherent imaging with significantly improved signal/noise ratio, emerging the light atom positions those even sitting nearby the heavy atom sites. Below we briefly demonstrate the performance of the present Cs-corrected STEM based on the observation of an Al-Cu-Co quasicrystalline compound.

STEM Experiment

ADF-STEM observations were performed by JEM-2010F (Cs = 0.5 mm) and JEM-2100F with CEOS Cs-corrector (Cs ~ 0). The minimum full-width half-maximum (FWHM) of the probe are estimated to be approximately ~1.5Å and ~0.9Å, respectively. Samples for STEM observation were prepared by crushing the single-quasicrystal of decagonal compound $Al_{66}Cu_{17}Co_{17}$, followed by dispersing the crushed powders on perforated carbon films supported on copper grids. By this method, surface amorphous layer, roughness, and contamination that are frequently induced by ion-milling and strongly affect the ADF contrast can be avoided.

Imaging of $Al_{66}Cu_{17}Co_{17}$ decagonal quasicrystal

Decagonal quasicrystals are the planar realization of a quasiperiodic order, whose structure is described as a periodic stack of quasiperiodic layers and is composed of decagonal columnar clusters as a building unit. Because of their two-dimensional character, quasiperiodic planar arrangements of atoms can be directly addressed through high-resolution observations viewing along the tenfold-symmetry axis [8]. $Al_{66}Cu_{17}Co_{17}$ decagonal phase is thermodynamically stable and known to form well-ordered quasiperiodic structure with a certain amount of phason-related structural disorders.

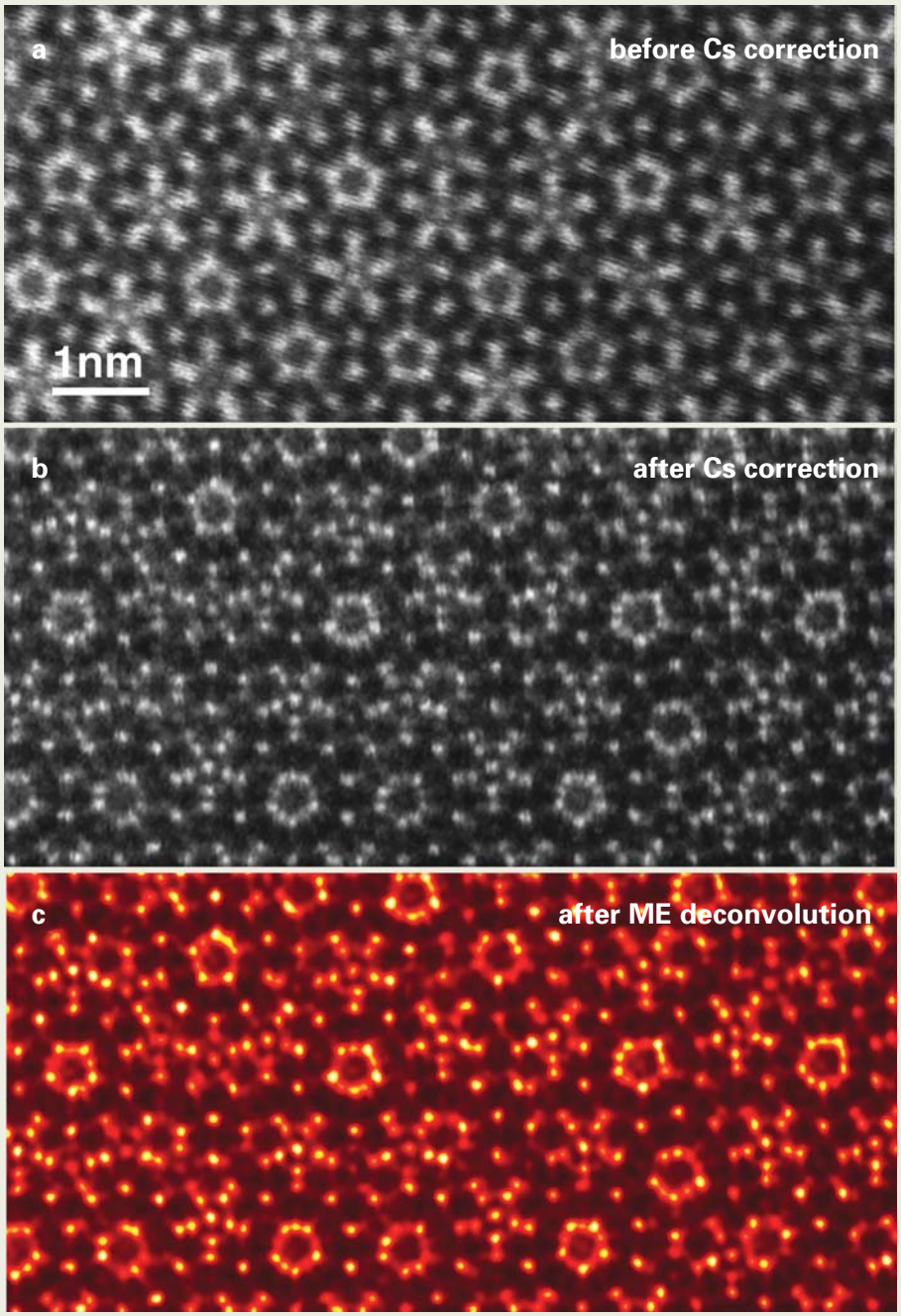

Fig. 3 ADF-STEM images of $Al_{66}Cu_{17}Co_{17}$ decagonal quasicrystal, taken with (a) JEM-2010F (Cs = 0.5mm) and (b) JEM-2100F with Cs-corrector (Cs~0). (c) Maximum-entropy deconvolution map obtained from Cs-corrected image of (b).

Figures 3 (a) and **(b)** show the ADF-STEM images of the decagonal $Al_{66}Cu_{17}Co_{17}$, obtained before and after the Cs-correction, respectively. From a comparison of these images, we immediately notice significant improvements of resolution and signal/noise ratio. The better resolution can be firstly seen for the brightest spots representing the atomic columns of Cu or Co, which appear to be quite sharper after the Cs-correction. Secondary, by looking carefully the image after the Cs-correction, there emerges many weak spots between the brightest spots; concerning the present compound of $Al_{66}Cu_{17}Co_{17}$, these are reasonably attributed to the Al columns. This is a remarkable effect of Cs-correction, provided a better signal-to-noise ratio which has been realized by suppressing secondary-maxima

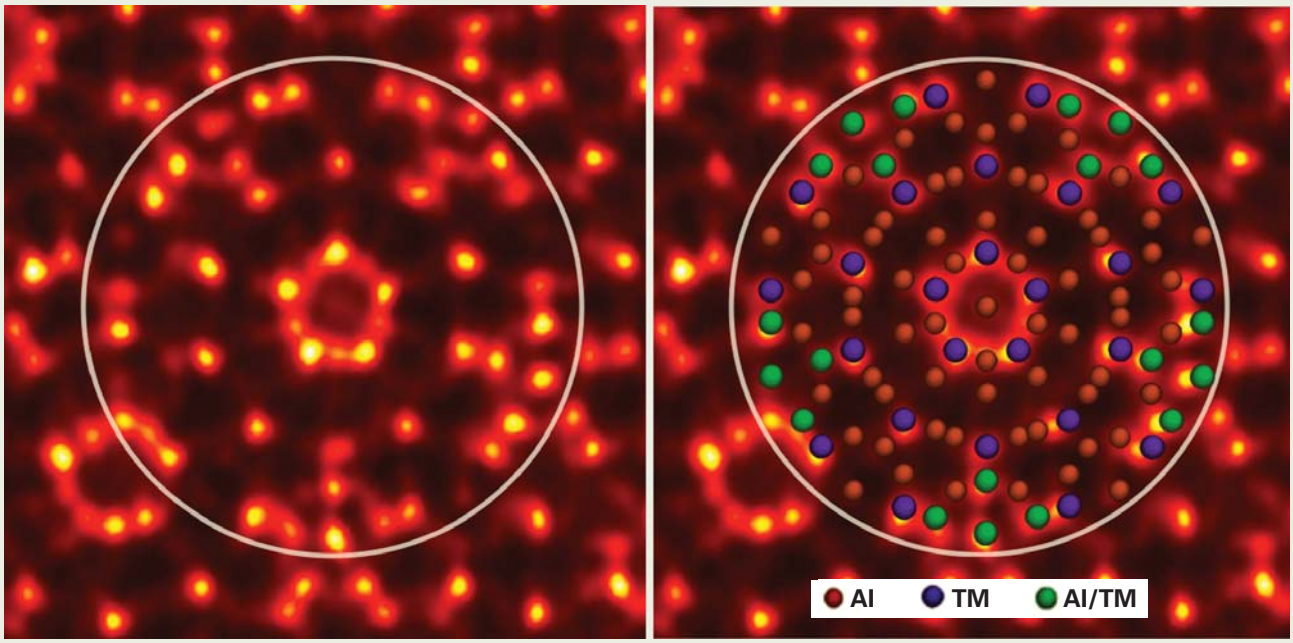

Fig. 4 Decagonal cluster with five-fold symmetry, which is a structural unit for the present decagonal $Al_{66}Cu_{17}Co_{17}$. Circles with a diameter of about 2 nm are inserted for its representation. In the structural model, TM represents the transition metals, namely Cu or Co.

that exist in uncorrected probe tails, and by increasing probe current (see **Fig. 2**). For the incoherent images described by Eq.(1), atomic structures, $O(\mathbf{R})$, can be directly addressed by a simple deconvolution procedure using $P(\mathbf{R})$ at given equipment parameters. Deconvolution using maximum entropy (ME) algorithm gives a safest, least possible structure that fits the experimental image. **Fig.3 (c)** shows the result after ME-deconvolution on Cs-corrected image, where the weak spots representing Al columns emerge out clearer by effective reduction of the quantum noise. Here we note in particular that, even applying the ME-deconvolution processing, the weak peaks never showed up from the non-Cs corrected STEM image (**Fig.3 (a)**) [9]. Given that sufficient signal/noise ratio with the Cs-corrected sharper/brighter probe, the ME-deconvolution effectively works to search the weak peaks that represent relatively light atomic sites.

Now we are able to discuss local structural details based on the incoherent STEM image, in which distributions of both the heavy and light atoms are seen simultaneously even under the Z-contrast condition. **Figure 4** shows an example of the cluster structure of the present $Al_{66}Cu_{17}Co_{17}$ quasicrystalline compound. One of the questions has been whether or not the Al atoms sit at the center of the cluster, since the atomic behaviors around the cluster center are believed to be the key to understand phason-related fluctuations [10]. Cs-corrected STEM imaging has indeed provided the answer – we see a certain weak peak at the cluster center in **Fig.4**, which is found to be reasonably attributed to the Al sites after tuning the cluster structure.

Summary

We have demonstrated that Cs-corrected STEM imaging provides a direct interpretation for not only heavy atom arrangements but also the light atom distributions in the $Al_{66}Cu_{17}Co_{17}$ quasicrystalline compound, even under the significant Z-contrast mode. By taking full advantage of incoherent STEM imaging, we do expect that STEM will uncover the veiled local structural details for various types of complicated compounds, whether they are periodic or aperiodic, to be providing a considerable number of breakthrough results in materials science.

References

[1] Shechtman, D., Blech, I., Gratias, D. and Cahn, J. W., Metalic phase with long-range orientational order and no translational symmetry. *Phys. Rev. Lett.*, **53**, 1951-1953 (1984).

[2] Bak, P., Icosahedral crystals: Where are the atoms? *Phys. Rev. Lett*., **56**, 861-864 (1986).

[3] Yamamoto, A., Crystallography of quasiperiodic crystals. *Acta Crystallogr*., **A 52,** 509-560 (1996).

[4] Haider, M., Uhlemann, S., Schwan, E., Kabius, B. and Urban, K., Electron microscopy image enhanced. *Nature*, **392**, 768–769 (1998).

[5] Batson, P. E., Dellby, N. and Krivanek, O. L., Sub-ångstrom resolution using aberration corrected electron optics., *Nature*, **418**, 617–620 (2002).

[6] Pennycook, S. J. and Jesson, D. E. High-resolution Z-contrast imaging of crystals. *Ultramicroscopy*, **37**, 14--38 (1991); High-resolution incoherent imaging of crystals. *Phys. Rev. Lett*., **64**, 938- 941 (1990).

[7] Pennycook, S. J., in Advances in imaging and electron physics, Vol. 123, pp173-206 (2002, Elsevier Science, USA).

[8] Abe, E., Yan, Y. and Pennycook, S. J., Quasicrystals as cluster aggregates. *Nature Materials*, **3**, 759-767 (2004).

[9] Ishizuka, K. and Abe, E., Improvement of spatial resolution of STEM-HAADF image by maximum-entropy and Richardson-Lucy deconvolution. Proc. of 13th European Microscopy Congress, IM03.P06 (2004).

[10] Abe, E., Pennycook, S. J. and Tsai, A. P., Direct observation of a local thermal vibration anomaly in a quasicrystal. *Nature*, **421**, 347-350 (2003).

[11] Fisher, I. R. et al. Growth of large-grain R–Mg–Zn quasicrystals from the ternary melt (R = Y, Er, Ho, Dy and Tb). *Phil. Mag.*, **B 77**, 1601-1615 (1998).

A New High-Temperature Multinuclear-Magnetic-Resonance Probe for Structure, Dynamics, and Reaction in Supercritical Water

Ken Yoshida†, Nobuyuki Matubayasi†, Masaru Nakahara†, Takeyoshi Ikeda†† and Takahiro Anai††

†Institute for Chemical Research, Kyoto University
††Analytical Instruments Division, JEOL Ltd.

A high-resolution nuclear magnetic resonance (NMR) probe (wide bore, 500 MHz for ^{1}H) has been developed for multinuclear pulsed field gradient spin-echo (PGSE) diffusion measurements at high temperatures up to 450°C. The high-level temperature homogeneity at high temperature is attained by using an innovative solid-state heating system composed of a ceramic (AlN) with high thermal conductivity. The new probe has been applied to the self-diffusion measurements on supercritical water over wide temperature and density ranges of 30-400 °C and 0.0041-1.0 g cm^{-3}, respectively.

Introduction

Recently, super- and subcritical water attracts much attention as a green solvent alternative to harmful organic solvents. Various kinds of new organic reactions have been found to be induced in super- and subcritical water [1], [2], [3], [4], [5]. Actually, nature has known the power of supercritical water since long before human beings have begun to learn it. Hot water is naturally abundant in the hydrothermal vents in the deep ocean [6]. Supercritical water was much more widely spread in the hot ancient ocean and thus chemical evolution is believed to have proceeded in hot water. Recently hydrothermal synthesis of a precursor of an amino acid has been demonstrated in a test tube [7]. Thus supercritical water is a novel, green, and natural solvent for the next generation.

In order to understand, utilize, and control supercritical reactions, we need to elucidate the supercritical hydration from a dynamic viewpoint. NMR is a most suitable, promising method for the purpose. Previously, proton NMR [8], [9], [10], neutron scattering [11], x-ray diffractometry [12], infrared (IR) [13], and Raman spectroscopies [14] have been used to study the structure of supercritical water. NMR data can be analyzed more simply and clearly than IR and Raman data because of the information about the hydrogen-bonding structure due to the motional narrowing. According to the state-of-the-art, modern NMR apparatus is much more powerful than the neutron scattering and x-ray diffractometry. Using the first-generation NMR probe, we have elucidated the existence of the static hydrogen bonding [8], [9] and the timescale of the rotational dynamics (several tens of fs) in supercritical water [15].

We have developed a second-generation high-temperature NMR probe that can be applied to the translational, as well as rotational, diffusion measurements [16]. The translational dynamics is important since diffusion controls the rate of collision between reactive species. So far, the method applicable for supercritical conditions has been limited to the electric conductivity measurement [17], [18], [19], [20]. However, the conductivity method cannot be used for neutral species. The limitations should be overcome because some of interesting chemical reactions in such neutral molecules as H_2, CO, CO_2, HCOOH, and H_2O are known to play a key role in controlling supercritical water reactions. Using NMR, such neutral molecules are observable. The difficulty in measuring the high-temperature diffusion is the temperature inhomogeneity that can affect the diffusion measurement to a large extent. We have overcome this difficulty by introducing a new heating system that can regulate the temperature with precision. In the newly developed system, the sample is symmetrically heated from the upper and lower sides by using a solid-state material of high thermal conductivity. The new probe is multinuclear, and can be used for a variety of nuclear species over a wide range of frequencies in a single set-up; various metallic elements (ions) can be also monitored by the new probe. The present high-precision NMR probe allows us to discuss the self-diffusion in the extremely low density region [21]. The new probe has been successfully applied to elucidate such a subtle effect as the isotope effect at high temperatures [16]. The self-diffusion coefficients are determined accurately enough to allow detailed comparison to theoretical analysis.

In this paper, we demonstrate the versatility of the new high-temperature NMR probe and show the recent results on the self diffusion measurement in super- and subcritical water. We also briefly introduce the possible applications of the new probe to a broad range of areas.

High-Temperature Probe

The following limitations of the first-generation probe [8], [9] have been improved by the second-generation high-temperature NMR probe. (i) The field strength of the superconductor magnet was 6.35 T (270 MHz for ^{1}H, wide-bore). (ii) The probe was not for multinuclear use (a different probe for each nucleus). (iii) The temperature homogeneity was insufficient for diffusion measurements because of the one-way flow of heated nitrogen gas from the bottom. The new probe was cooperatively developed by the Kyoto University group and JEOL; patent application, No.WO2005/022183. The probe is built into a 500 MHz system (JEOL JNM-ECA500) with a wide-bore superconductor magnet (11.3 T). The new high-temperature probe is multinuclear and can cover a wide range of resonance frequencies of 36-500 MHz; ^{14}N, ^{35}Cl, ^{133}Cs, ^{17}O, ^{2}H, ^{29}Si, ^{13}C, ^{23}Na, ^{31}P, ^{19}F, and ^{1}H can be measured with a single

Uji, Kyoto 611-0011, Japan
E-mail : nakahara@scl.kyoto-u.ac.jp

probe, irrespective of the charge of the monitored species. We have succeeded in determining the self-diffusion coefficient of the sodium ion in supercritical aqueous electrolyte solution [22].

In **Fig. 1**, we illustrate the new high-temperature probe. To minimize the temperature gradient in the sample, two electric heaters are placed symmetrically on the upper and lower sides of the sample. The sample holder is made of a good heat conductor, aluminum nitride; the thermal conductivity is as high as 200 W m^{-1} K^{-1}, which is close to that of aluminum (240 W m^{-1} K^{-1}). The rf coils are made of gold and can resist high-temperatures up to 450 ºC. A large magnetic field gradient of 270 G cm^{-1} can be generated at maximum. Hence the probe can be applied to measure the self-diffusion for various molecular species with low frequency and/or slow motion. To cancel the leaking of the gradient pulses, the shielding coil is incorporated. The heated nitrogen gas used in the previous probe is no longer necessary, and thus the new probe can be handled almost as safely as a normal solution-state probe. The gas-flow system is composed of materials of a wide range of magnetic susceptibility. This influenced the internal magnetic field and limited the shim conditioning to a high level.

The present measurements are carried out under isochoric conditions. The high-temperature and high-pressure conditions are controlled by the sealed tube method as shown in **Fig. 2** [7], [8], [15], [16], [21]. The sealed quartz tube was positioned at the rf center to attain a high level of resolution.

Temperature Homogeneity

Homogeneous temperature distribution is indispensable for accurate NMR diffusion measurements at high temperatures. The temperature distribution within the new probe system is shown in **Fig. 2** as a function of the height *z* from the bottom of the sample holder.

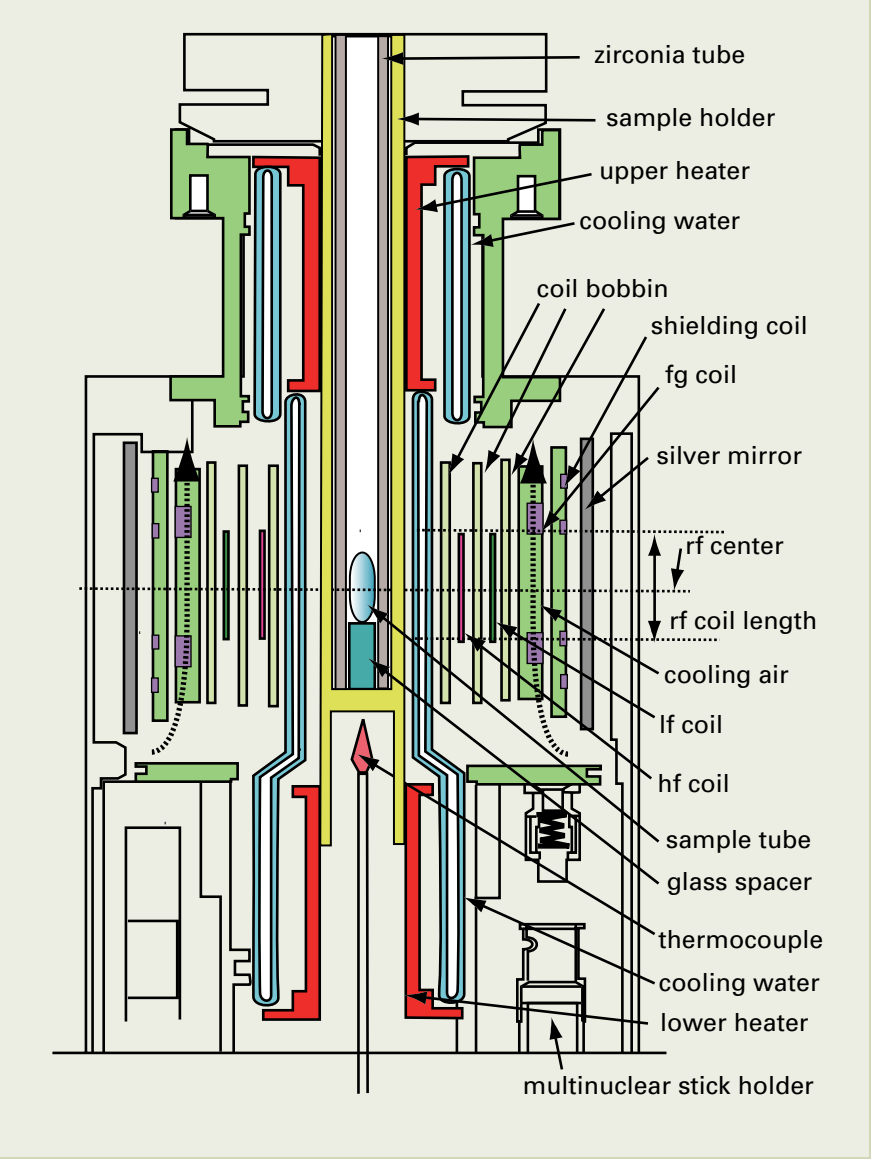

Fig. 1. The cross-section view of the high-temperature multinuclear diffusion NMR probe.

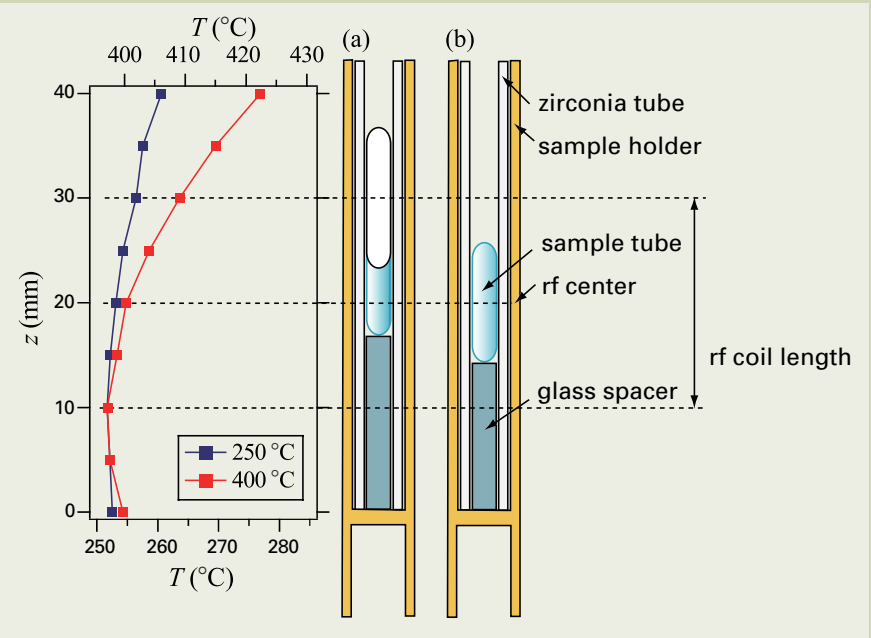

Fig. 2 The temperature distribution in the sample holder as a function of the height *z* (mm) from the bottom; the temperature monitored by the probe thermocouple is 250 (blue) and 400 °C (red). The sample settings for (a) subcritical and (b) supercritical conditions are shown on the scale corresponding to the longitudinal axis of the graph.

The sample is positioned close to the temperature minimum so that the temperature inhomogeneity can be minimized.

The currents of upper and lower heaters are adjustable independently to avoid the convection. The upper and lower heater currents are optimized to make the temperature gradient slightly upward with increasing z. In the previous probe, the temperature gradient was inevitably downward because of the heated gas flow from the bottom of the sample. We can confirm the absence of the convection effect by optimizing the parameters involved in the pulse sequence. When the diffusion coefficient is reliable in the optimized conditions, it should be independent of the time required for a molecule to diffuse in the pulsed field gradient spin-echo experiment.

The sample temperature was stable over time within ±0.2 ˚C due to the feedback temperature control. The sample temperature was controlled using a pulsed direct current applied at an on/off interval of 2.4 s as illustrated in **Fig. 3**. In order to avoid noises from the current on/off, the heater switches were left untouched during the acquisition of each free induction decay (FID). The current value during FID acquisition is optimized at each temperature.

Density Measurement

A precise density measurement is essential for the diffusion measurement in the low-density region. The sealed tube method employed in this study is suitable for the purpose. We have proposed two methods, the chemical shift method and the mass-volume method, which are used in the extremely low-density region [21] and medium to high-density region, [16] respectively.

In the chemical shift method, the density is determined by making use of the transition temperature T_t and the *PVT* data on the liquid-gas coexistence curve. The density in a supercritical state is equal to that of the gas branch of the coexistence curve at T_t when the density is lower than the critical value. The *PVT* data for water are released by the International Association for the Properties of Water and Steam (IAPWS) [23]. The T_t can be determined according to the temperature dependence of the proton chemical shift δ of the gas phase. In **Fig. 4**, the temperature dependence of δ is shown for a water sample at 0.0041 g cm^{-3} in the vicinity of T_t. As can be seen, δ has a maximum. The temperature of the maximum δ is T_t because the temperature dependence of the hydrogen-bond strength, which is in positive correlation with δ, turns over at T_t in a closed system. T_t and the density could be then determined with a precision of ±1 ºC and ±1%, respectively. This method can be applied to determine for aqueous electrolyte systems in supercritical conditions.

It becomes difficult to apply the chemical shift method when the density approaches the critical value. For such a density region, we propose another method called the mass-volume method, in which the bore volume of the tube and the mass of the sample are precisely determined. The density is given by the solution volume in a sample tube divided by the bore volume of the tube determined by the inner diameter. The volume of solution was obtained by the masses of the tube with and without the sample. The bore volume of the tube is the difference between the total volume of the tube and the volume of the quartz itself; the total volume is the volume determined by the outer diameter and is equal to the sum of the bore volume and the volume of the quartz itself. The total volume of the tube was determined by the change in the position of the meniscus when it was immersed into a liquid. The volume of the quartz itself was determined by its mass and density data. The masses were measured to an accuracy of 0.1% using an ultramicrobalance (Mettler Toledo UMX-2). When the sample is water, this method can be applied at 0.07 g cm^{-3} and above.

Diffusion Measurement

Our sample is pure light and heavy water (^1H_2O and ^2H_2O). The diffusion coefficients are obtained by the pulsed field gradient spin-echo method [24], [25]. The quality of our multinuclear spectra can be seen from those in **Fig. 5(a)** taken under extreme conditions. There is shown the ^2H spectrum for heavy water at a low density of 0.097 g cm^{-3} at a supercritical temperature of 400 ºC. This is a most difficult condition for the acquisition of the FID signals in this work. The FID signals were accumulated once for each duration time of a field gradient pulse δ. The signal-to-noise

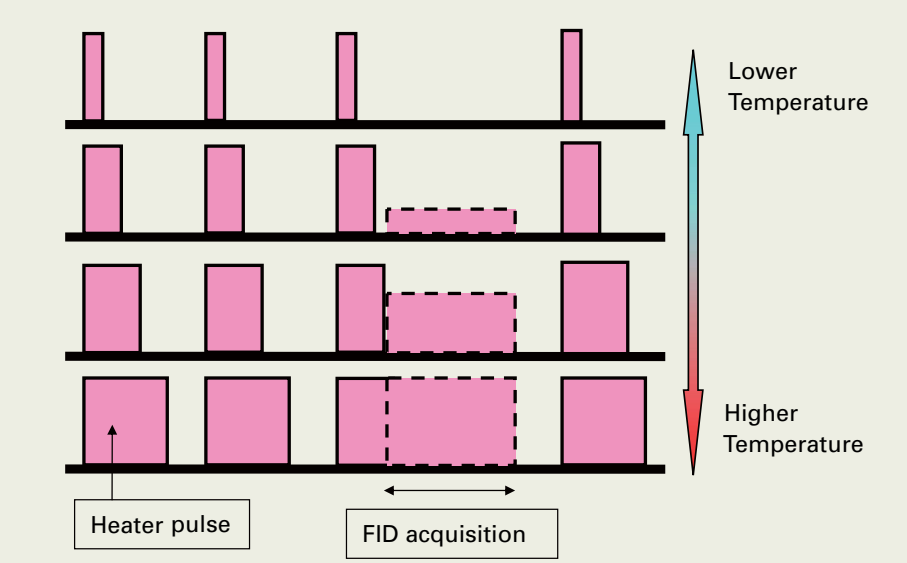

Fig. 3 An illustration of the temperature control by using the pulsed heater current.

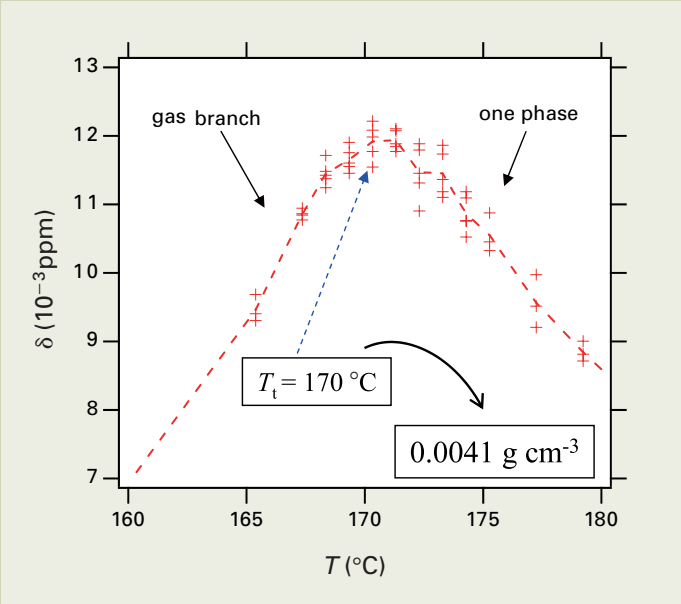

Fig. 4 The chemical shift δ plotted against temperature for the sample at the lowest density of 0.0041 g cm^{-3}. The δ for the gas branch of the liquid-gas coexistence curve at 146 ºC (0.0023 g cm^{-3}) is set to zero. The dashed line indicates the average of the repetitions.

ratio for δ = 0 ms exceeds 40, resulting in accurate diffusion coefficients within ±1%. The intensities of spin-echo signals M(τ) are extracted from **Fig. 5(a)** and plotted in **Fig. 5(b)** in order to determine the diffusion coefficient. The total uncertainty of D at 400 ˚C is estimated as about ±5% by taking into account the error due to the sample resetting.

Self-Diffusion Coefficients

The self-diffusion coefficients D have been determined for light (^1H_2O) and heavy (^2H_2O) water along the coexisting curve. There have been carried out a few pulsed field gradient spin-echo (PGSE) experiments on the self-diffusion coefficients of water in sub- and supercritical water [26], [27], [28], [29]. The D values for ^1H_2O by Hausser et al.[26] are in good agreement with the present values over the entire temperature range. The D values for ^1H_2O by Krinicki et al. [27] are slightly larger. The difference can be ascribed to the convection effect in their apparatus. Furthermore, our measurement was performed at resonance frequency one order of magnitude higher. For the case of ^2H_2O, the D values by Jonas and coworkers [29] are in reasonable agreement with the present values.

The temperature and density effects are not separated when the temperature is varied along the saturation curve. In supercritical water, however, the density effect can be isolated by fixing the temperature; thus the kinetic and potential effects are more clearly differentiated. The self-diffusion coefficient D obtained for water including extremely low densities is shown in **Fig. 6** in the form of $\rho D/\sqrt{T}$. The slope of $\rho D/\sqrt{T}$ against ρ is almost zero or slightly negative. This slope can be interpreted in terms of the lifetime of the supercritical hydration structure obtained through our recent molecular dynamics (MD) simulation [30]. The extrapolation of the experimental values to the zero density limit are much smaller than those predicted by the hard-sphere model, in which attractive interactions are neglected. This reflects the strong effect of attractive interaction on the self-diffusion in the low-density supercritical water.

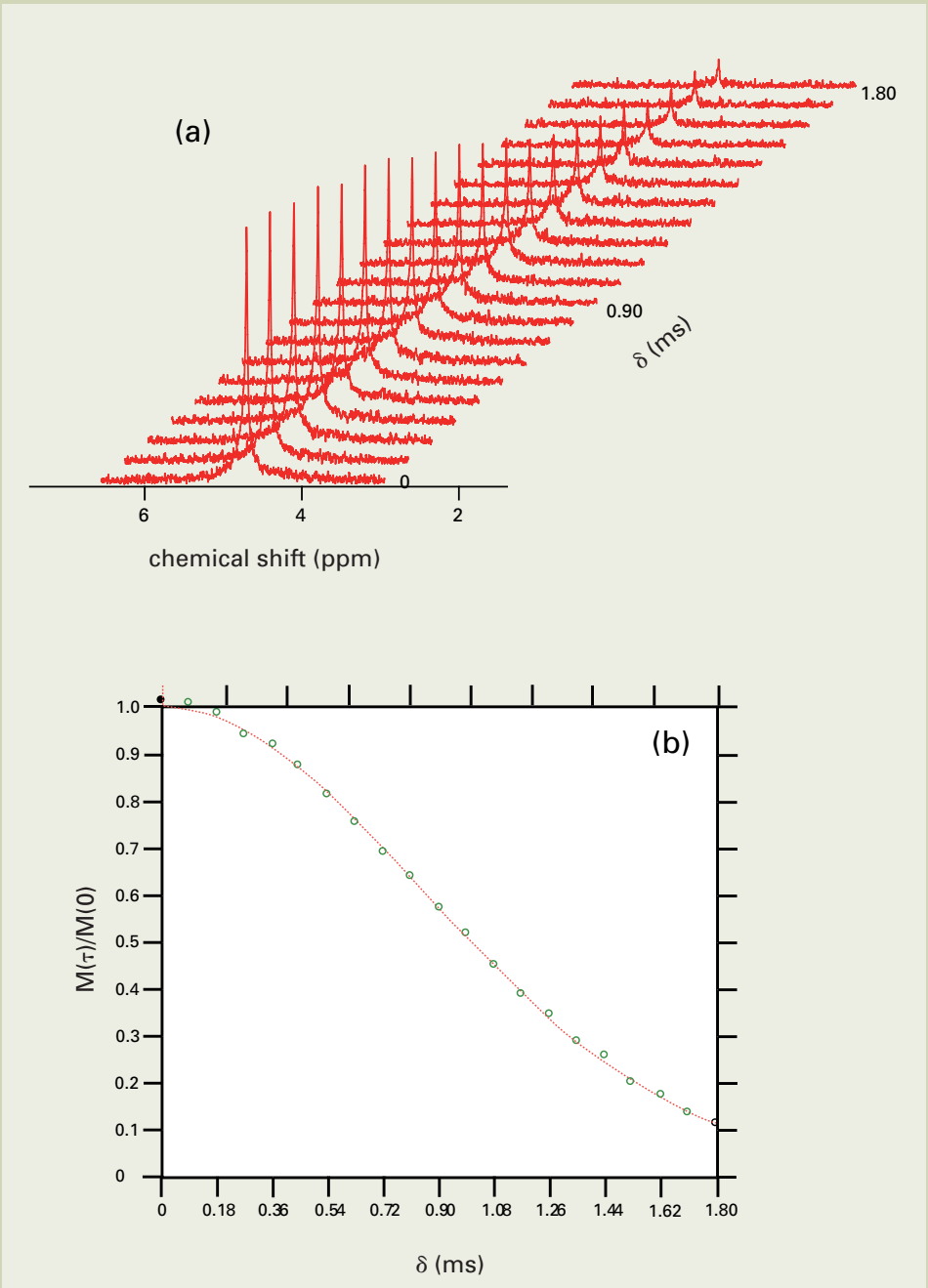

Fig. 5 (a) The attenuation of the echo signal of ^2H in ^2H_2O with a density of 0.097 g cm^{-3} and a supercritical temperature of 400 ºC. (b) The intensity of the echo signals shown in (a) as a function of the duration of the magnetic field gradient pulses M(τ) and M(0) are the intensities of the spin-echo signal when the field gradient is present and absent, respectively. The signal intensities are on an arbitrary scale.

Isotope Effect

At ambient conditions, the diffusion data of various isotopic species of water have yielded a rather detailed picture of the diffusion in water [31], [32]. In spite of the recent increase of interest in the dynamic isotope effect in water [33], [34], [35], reliable data are still awaited at high temperatures and high pressures, owing to experimental difficulties. The new high-temperature probe developed here is powerful enough to determine the isotope effect, which requires extremely high accuracy and precision.

In **Fig. 7**, we plot the isotope ratio $D(^1H_2O)/D(^2H_2O)$ against the temperature along the coexisting curve. It is clearly shown that the isotope effect decreases with increasing temperature. The value $D(^1H_2O)/D(^2H_2O)$, which is 1.23 in ambient water, becomes close to and slightly larger than unity at 350 ºC. This subtle effect has been beyond the precision of the previous studies [26], [27], [29]. Since ^2H_2O is considered to be more structured than ^1H_2O [36], [37], the isotope effect is a useful probe to intermolecular interaction, typically hydrogen bonding, apart from the density and the temperature dependencies. In ambient conditions, the effect of intermolecular interaction strength overwhelms the mass effect; the lower the temperature and/or the higher the density, the larger the isotope effect [38], [39]. It is of great interest to investigate the effect of weakened and distorted hydrogen bonding on the self-diffusion for super- and subcritical water from the classical and quantum mechanical points of view.

Future Directions

The high-temperature NMR method is now being proven to be useful in a broad range of areas including material, geological, and environmental sciences and technology. It is powerful in detecting reaction intermediates and identifying hydration effect on reactive species for environmentally benign, noncatalytic reactions in hot water [5], [7]. Application to ionic liquids, a new type of green solvent, is also subject to in-situ observation of a chemical process in it over a wide range of temperature [40]. A high-temperature condition is useful to characterize physical and chemical properties of polymers and organic complexes; a high-resolution, multinuclear

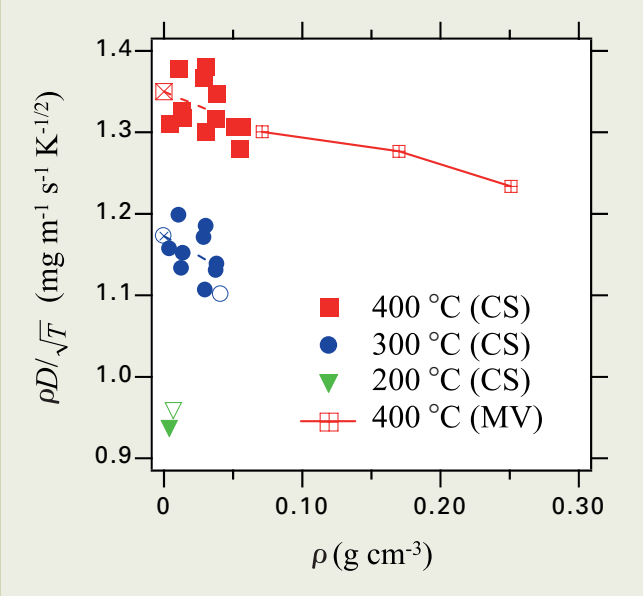

Fig. 6 The self-diffusion coefficient D of water determined in supercritical conditions. D is shown in the form of the product of the self-diffusion coefficients of water and the density divided by the square root of the temperature, $\rho D/\sqrt{T}$. The open symbols indicate the values on the gas branch of the liquid-gas coexistence curve. The dashed line is linearly fitted to the experimental values and the crossed symbols indicate the values extrapolated to the zero-density limit, $(\rho D)^0/\sqrt{T}$. MV and CS in the figure stand for the mass-volume method and the chemical shift method, respectively, for the ρ determination.

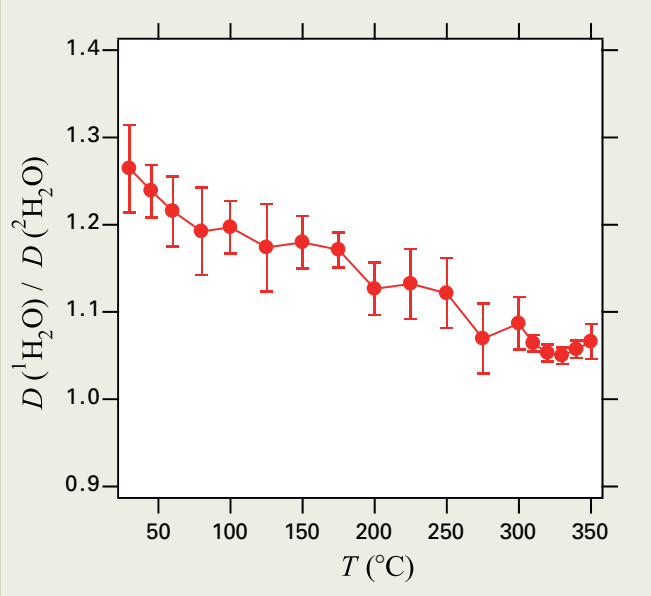

Fig. 7 Temperature dependence of the isotope ratio $D\,(^1H_2O)/D\,(^2H_2O)$ along the liquid branch of the liquid-vapor coexisting curve.

NMR can be conducted by melting or vaporizing them. It is thus expected in near future that the high-temperature NMR is a standard experimental procedure.

References

[1] *Water, A Comprehensive Treatise*, edited by F. Franks (Plenum, New York, 1972-1982), Vols. 1-7.

[2] J. S. Seewald, *Nature* (London) **370**, 285 (1994).

[3] P. A. Marrone, T. A. Arias, W. A. Peters, and J. W. Tester, *J. Phys. Chem.* A, **102,** 7013 (1998).

[4] N. Akiya and P. E. Savage, *Chem. Rev.*, **102**, 2725 (2002).

[5] Y. Yasaka, K. Yoshida, C. Wakai, N. Matubayasi, and M. Nakahara, *J. Phys. Chem.* A, **110**, 11082 (2006).

[6] Physicochemistry of Water in Geological and Biological Systems, edited by S. Nakashima et al., University Academy Press, Inc., Tokyo (2004).

[7] S. Morooka, C. Wakai, N. Matubayasi, and M. Nakahara, *J. Phys. Chem.* A, **109**, 6610 (2005).

[8] N. Matubayasi, C. Wakai, and M. Nakahara, *Phys. Rev. Lett.*, **78**, 2573 (1997).

[9] N. Matubayasi, C. Wakai, and M. Nakahara, *J. Chem. Phys.*, **107**, 9133 (1997).

[10] M. M. Hoffman and M. S. Conradi, *J. Am. Chem. Soc.*, **119**, 3811 (1997).

[11] A. K. Soper, F. Bruni, and M. A. Ricci, *J. Chem. Phys.*, **106**, 247 (1997).

[12] K. Yamanaka, T. Yamaguchi, and H. Wakita, *J. Chem. Phys.*, **101**, 9830 (1994).

[13] Y. E. Gorbaty and A. G. Kalinichev, *J. Phys. Chem.*, **99**, 5336 (1995).

[14] G. E. Walrafen, Y. C. Chu, and G. J. Piermarini, *J. Phys. Chem.*, **100**, 10363 (1996).

[15] N. Matubayasi, N. Nakao, and M. Nakahara, *J. Chem. Phys.*, **114**, 4107 (2000).

[16] K. Yoshida, C. Wakai, N. Matubayasi, and M. Nakahara, *J. Chem. Phys.*, **123**, 164506 (2005).

[17] A. S. Quist and W. L. Marshall, *J. Phys. Chem.*, **72**, 684 (1968).

[18] T. Hoshina, N. Tsuchihashi, K. Ibuki, and M. Ueno, *J. Chem. Phys.*, **120**, 4355 (2004).

[19] L. Hnedkovsky, R. H. Wood, and V. N. Balashov, *J. Phys. Chem.* B, **109**, 9034 (2005).

[20] M. Nakahara, Proceedings of the 14th International Conference on the Properties of Water and Steam, Kyoto, 12, (2004), edited by M. Nakahara et al., Maruzen Co., Ltd, Tokyo, (2005).

[21] K. Yoshida, N. Matubayasi, and M. Nakahara, *J. Chem. Phys.*, **125**, 074307 (2006).

[22] K. Yoshida, C. Wakai, N. Matubayasi, and M. Nakahara, Final Program and Abstracts for the 14th International Conference on the Properties of Water and Steam, 48 (2004).

[23] Release on the IAPWS Formulation 1995 for the Thermodynamic Properties of Ordinary Water Substances for General and Scientific Use, URL: http://www.iapws.org.

[24] E. O. Stejskal and J. E. Tanner, *J. Chem. Phys.*, **42**, 288 (1965).

[25] P. Stilbs, Progress in *NMR Spectroscopy*, **19**, 1 (1987).

[26] R. Hausser, G. Maier, and F. Noack, *Z. Natureforsch. Teil* A, **21**, 1410 (1966).

[27] K. Krynicki, C. D. Green, and D. W. Sawyer, *Faraday Discuss. Chem. Soc.*, **66**, 199 (1979).

[28] W. J. Wilber, G. A. Hoffman, and J. Jonas, *J. Chem. Phys.*, **74**, 6875 (1981).

[29] D. J. Wilbur, T. DeFries, and J. Jonas, *J. Chem. Phys.*, **65**, 1783 (1976).

[30] K. Yoshida, N. Matubayasi, and M. Nakahara, in preparation.

[31] R. Mills and K. R. Harris, *Chem. Soc. Rev.*, **5**, 215 (1976).

[32] H. Weingärtner, *Z. Phys. Chem., Neue Folge*, **132**, 129 (1982).

[33] Y. Marcus and A. Ben-Naim, *J. Chem. Phys.*, **83**, 4744 (1985).

[34] R. A. Kuharski and P. J. Rossky, *J. Chem. Phys.*, **82,** 5164 (1985).

[35] B. Guillot and Y. Guissani, *J. Chem. Phys.* **108**, 10162 (1998); B. Guillot and Y. Guissani, *Fluid Phase Equilibria*, **151**, 19 (1998).

[36] G. Némethy and H. A. Scheraga, *J. Chem. Phys.*, **41**, 680 (1964).

[37] M. Nakahara, M. Zenke, M. Ueno, and K. Shimizu, *J. Chem. Phys.*, **83**, 280 (1985).

[38] J. Buchhauser, T. Groß, N. Karger, and H. -D. Lüdemann, *J. Chem. Phys.*, **110**, 3037 (1999).

[39] L. Chen, T. Groß, H. Krienke, and H. -D Lüdemann, *Phys. Chem. Chem. Phys.*, **3**, 2025 (2001).

[40] Y. Yasaka et al. in preparation.

High Utility of Electro- and Cold-Spray Ionization Time-of-Flight Mass Spectra in Development of Functional Metalloenzyme Models: Detection of Labile Metal Complexes and Reactive Intermediates

Masahito Kodera

Department of Molecular Science and Technology, Faculty of Engineering, Doshisha University

Introduction

Metalloenzymes catalyze biological reactions, much more selective and efficient than reactions in a flask in synthetic chemistry [1a]. Aiming at clarifying enzymatic reaction mechanisms and artificially applying the highly selective biological reactions, relationship between the structures and functions of the metalloenzymes has been studied. As a synthetic approach, attempts have been made to develop functional models, which mimic the structures and functions of the active centers of the metalloenzymes by using simple metal complexes. This method has a great advantage that the functional models with small molecular size can be much more easily handled than the enzymes, leading to providing some insights into the enzymatic reaction mechanisms. Furthermore, from these studies, practical biomimetic catalysts may be developed, which resemble the vital functions of the biological system. Thus, research and development on the metal complexes as functional models of metalloenzymes are important from the viewpoint of biological chemistry as well as coordination chemistry and industrial chemistry. We have been interested in the structures and functions of metalloproteins having two metal ions at the active center, and developed highly functionalized polynuclear metal complexes that reproduce the functions of the metalloproteins. In this article, we first introduce several non-heme iron monooxygenases and further introduce soluble methane monooxygenase (sMMO) in detail, application of which is expected as a practical oxidation catalyst. In addition, we present our approach to the development of highly functionalized metal complexes as functional models of these metalloenzymes [1b]. Furthermore, we demonstrate the effectiveness of Electro- and Cold-Spray Ionization Time-of-Flight mass spectra in these studies.

Kyotanabe, Kyoto 610-0321, Japan
E-mail: mkodera@mail.doshisha.ac.jp

Non-heme iron monooxygenase

Monooxygenase is an enzyme that reductively activates dioxygen molecules and oxygenizes a substrate, where one oxygen atom is incorporated into a substrate and another is converted to water molecule [2]. Owing to its unique reaction mechanism, this enzyme has been attracting interests in various fields such as biochemistry, bioinorganic chemistry, organic chemistry, medical science and pharmaceutical science. Up to 1980s, studies were mainly performed for heme proteins, such as cytochrome P-450, horseradish peroxidase, chloroperoxidas, having heme iron at the active site [3]. Recently, various non-heme iron oxidases have been found [4]. Here, I briefly introduce soluble methane monooxygenase (sMMO) having a non-heme diiron center and pterin-dependent hydroxylase (phenylalanine hydroxylase (PAH) and tylosin hydroxylase (TH)) and isopenicillin N synthetic enzyme (IPNS) having a non-heme monoiron center [5].

Pterin-dependent hydroxylase adopts two electrons and two protons of dihydropterin to reductively activate dioxygen molecule to hydroxylate an aromatic ring of a substrate (**Scheme 1**). PAH catalyzes the first reaction of the phenylalanine metabolism to convert phenylalanine to tylosin [6]. PAH, found in rat liver and in bacteria, exists as 33 kDa in monomer and 200 kDa in tetramer, respectively, and is known to have a Fe ion in its active center [6]. Crystal structure of PAH revealed that the Fe ion is coordinated with two His imidazole and a Glu carboxylate groups (**Figure 1**). TH catalyzes conversion of tyrosine to 3,4-dihydroxyphenylalanine in the biosynthesis of catecholamine [7]. TH, present in brain and in adrenal medulla, consists of a subunit of 60 kDa and has an active center similar to that of PAH (**Figure 1**) [8].

As shown in **Scheme 2**, in the oxidative ring-closing reaction, isopenicillin N synthetic enzyme (IPNS) catalyzes a reaction in which a β-lactam ring and a thiazolidine ring are simultaneously formed, [9] where one dioxygen molecule receives four electrons and four protons from ACV, generating two water molecules. IPNS has a Fe ion and its molecular mass is 37-40 kDa. It is known that at the active center, the Fe ion is coordinated with two His imidazole and a Glu carboxylate groups, being almost the same as that of the pterin-dependent hydroxylases (**Figure 1**) [10].

In the catalytic reaction of pterin-dependent hydroxylase (PAH, TH), a cofactor of pterin is indispensable, whereas soluble methane monooxygenase (sMMO) catalyzes dioxygen activation using two Fe ions, making a cofactor unnecessary. Thus, sMMO may be highly applicable as a practical catalyst.

Soluble methane monooxygenase (sMMO)

$$CH_4 + O_2 + NADH + H^+ \xrightarrow{\text{sMMO}} CH_3OH + H_2O + NAD^+ \quad \text{(eq. 1)}$$

sMMO converts CH_4 to CH_3OH in methanotroph (eq. 1) [11], [12]. Methanotroph uses methane as a sole carbon source and energy source, and does not incorporate any hydrocarbons other than methane. Interestingly, however, sMMO catalyzes monooxygenation of various organic compounds in vitro, and converts alkane to alcohol, olefin to epoxide, and aromatic compound to phenol [13]. sMMO is so far isolated from two kinds of methanotroph, *methylococcus capsulatus* (Bath) and *methylosinus trichosporium* OB3b, and consists of three protein components, hydroxylase (MMOH), control protein B (MMOB) and reductase (MMOR). Combination of these three components realizes methane oxidation via reductive dioxygen activation [14]. MMOH obtained from *methylococcus capsulatus* (Bath) has a molecular mass of 210 kDa and it is revealed that MMOH possesses diiron center by spectroscopic and magnetic measurements. When hydrogen peroxide is used as an oxidant, MMOH catalyzes the monooxygenation of various substrates in the absence of MMOB and MMOR [15].

Lippard *et al*. reported crystal structures of MMOH isolated from *methylococcus capsulatus* (Bath) with both its reduced and oxidized forms [16]. These structures are shown in **Figure 2**. Both reduced and oxidized forms contain two Fe ions, which are coordinated with two His imidazole, four Glu carboxylate groups, and one or two water molecules. Hemerthyrin (Hr), a non-heme diiron protein structurally similar to sMMO, is a O_2-transport protein [17]. In the active center of Hr, two Fe ions are coordinated with five His imidazole and two Glu carboxylate groups. When comparing the active site structures between sMMO and Hr (**Figure 3**), it is clear that the diiron center of sMMO is located in a carboxylate-rich coordination environment. Lippard et al. pointed out that the binding mode of a carboxylate group in sMMO changes between the reduced and oxidized forms, where a monodentate binding mode in the reduced form changes to a bidentate bridging mode in the oxidized form. This structural change in the carboxylate group is called carboxylate-shift. It is propsed that the carboxylate-shift plays a essential role in controlling Fe-Fe distance in the dioxygen activation [18].

Furthermore, Lippard *et al*. revealed that, by trapping Xe, which is nonpolar and water-soluble gas similar to methane, into the cavities of sMMO, the cavities appear to exist near the active center of sMMO (**Figure 4**) [19]. It was shown that these cavities surrounded by plural non-polar amino acid residues, valine, phenylalanine, leucine and methionine, to be a very hydrophobic environment where no water molecule is present. From this fact, a possibility was suggested that sMMO uses a substrate-binding moiety as a reaction site and selectively monooxygenates hydrocarbones.

Lipscomb et al. proposed a dioxygen activation mechanism using sMMO isolated from *Methylosinus trichosporium* OB3b, where the reduced form of MMOH binds dioxygen molecule to form an intermediate P, then this intermediate P is transformed to an active species Q, which oxidizes substrate (**Scheme 3**) [20]. P is relatively stable and its structure is estimated to be μ-peroxodiiron(III) complex, but the active species Q is very unstable. The active species Q was detected as a transient species by Moessbauer and EXAFS studies using a rapid freeze-quench technique for the reaction of dixoygen molecule with the reduced form of MMOH to reveal that it is a diiron(IV) and these two Fe ions possess symmetrical structures. In addition, Lipscomb et al. clarified that strong antiferromagnetic interactions operate between the Fe ions. Furthermore, detailed spectroscopic studies of both sMMO itself and model compounds estimated that active species Q has a Fe_2O_2 diamond core structure in which two Fe(IV) ions are bridged by two oxo (O^{2-}) and a carboxylate group. The oxidation reaction of C-H by the active species Q is considered to progress via a radical rebound mechanism, as found by product analysis and study of the kinetic isotope effect [21], [22].

Development of a highly functionalized metal complex

It is still difficult to use sMMO as a catalyst for the purpose of synthetic and/or industrial application due to complexity of the enzyme composed of three components. In addition, from the viewpoint of clarification of the dioxygen activation mechanism, we have to recognize that there is a limitation in studies using sMMO itself due to instabilities of reaction intermediates. Thus, if we can synthesize a simple metal complex as a functional model, which reproduces the function of sMMO, it can be applied to highly selective oxidation reactions of various organic compounds. Moreover, detailed spectral studies of the dioxygen activation and the substrate oxidation with the functional model may give some insights into the mechanism of sMMO.

Diiron complexes obtained by accumulation of monoiron complexes or diiron complexes supported by dinucleating ligands having an endogenous bridge group have been used so far as a functional model of sMMO. However, in both cases, there are problems in which the diiron core of the accumulated diiron complexes easily dissociate to monoiron in a solution and the iron-iron distance in the diiron complexes of dinucleating ligands having an endogenous bridge group is not flexible. Thus, these diiron complexes did not produce significant achievements as a functional model of sMMO, except for some spectral evidences as structural models of intermediates P and Q. We considered that the requirements for the functional model of sMMO are (1) a stable diiron core structure in a solution under the reaction conditions, and (2) the structural flexibility of the diiron core. To meet these requirements, we thought that it is effective to use a diiron complex supported by dinucleating ligands which do not possess any endogenous bridging group. Then, we synthesized various new dinucleating ligands, all of which have a common 1,2-bis(2-pyridyl)ethane moiety, and we revealed what kind of structure is stabilized by this type of ligands in a solution and a solid-state. Finally, we synthesized a stable diiron complex in a solution by using this type of ligands, resulting in a successful synthesis of a highly functionalized metal complex that reproduces the functions of sMMO.

In the second chapter, we describe the synthesis of various dinucleating ligands, all of which have a 1,2-bis(2-pyridyl)ethane common moiety, and the synthesis, structure and a phosphoester hydrolytic activity of the copper complexes supported by this type of ligands. In the third chapter, we demonstrate the synthesis of a diiron complex supported by dinucleating ligands having a 1,2-bis(2-pyridyl) ethane common moiety, and reveal the oxygen activation mechanism by using the diiron complex. Finally, we introduce recent studies of highly functionalized metal complexes that catalyze highly efficient and selective oxidation reactions.

Utilization of Electro- and Cold-Spray Ionization Time-of-Flight mass spectra

To obtain the functional models of the

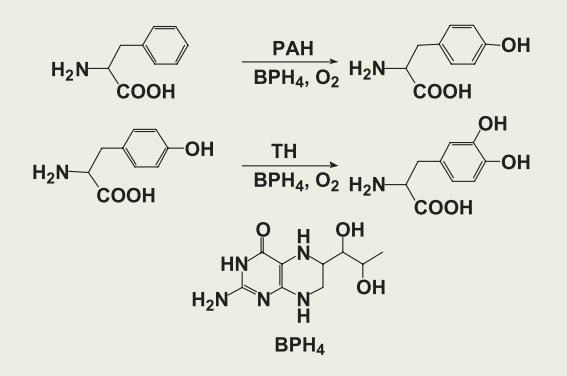

Scheme 1

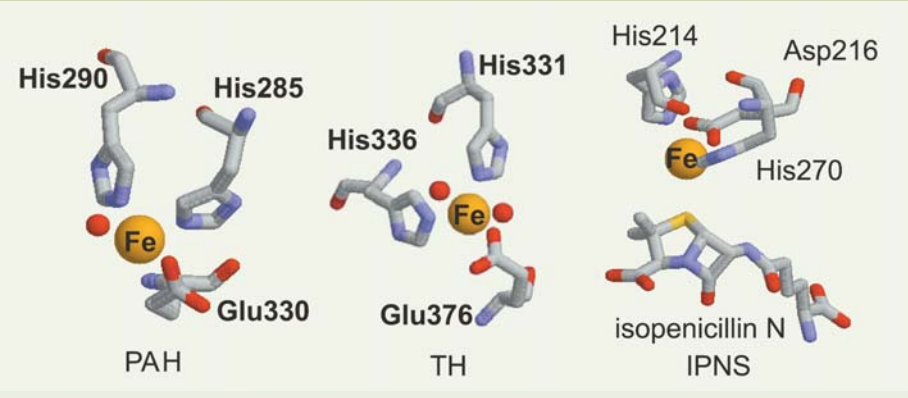

Fig. 1 Crystal structures of active site for PAH, TH, and IPNS.

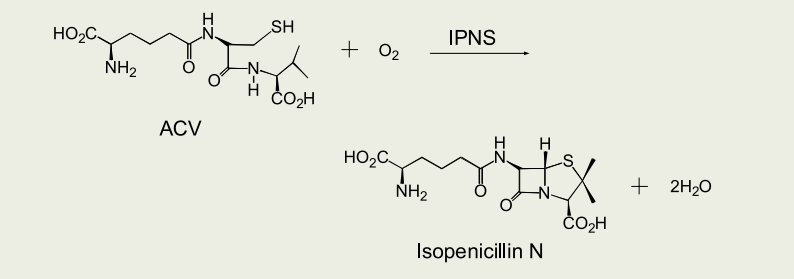

Scheme 2

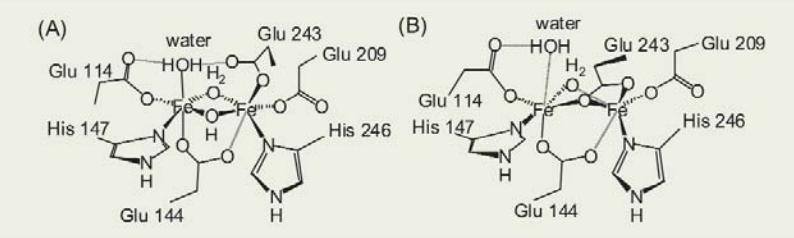

Fig. 2 The X-ray structures of the active site diiron center of MMOH from *M. capsulatus* (Bath): (A) the diferric form at –160 °C, and (B) the diferrous form at –160 °C.

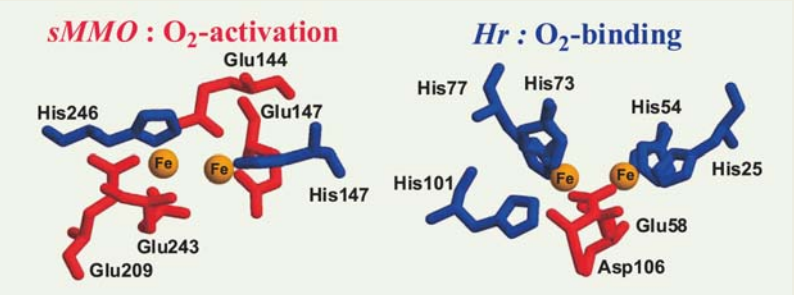

Fig. 3 Active sites of sMMO and Hr, carboxylate and imidazole are depicted as red and blue, respectively.

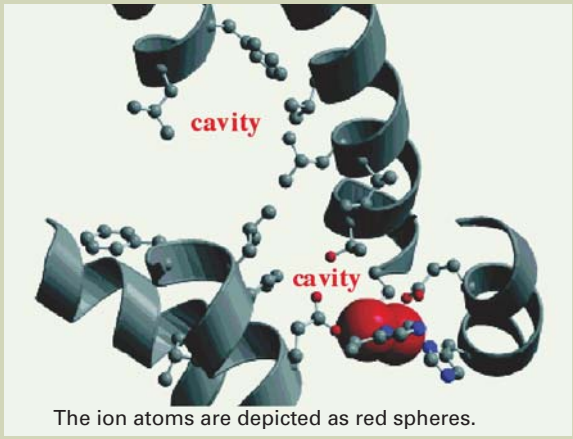

Fig. 4 Active site and cavities present in the α-subunit of sMMO.

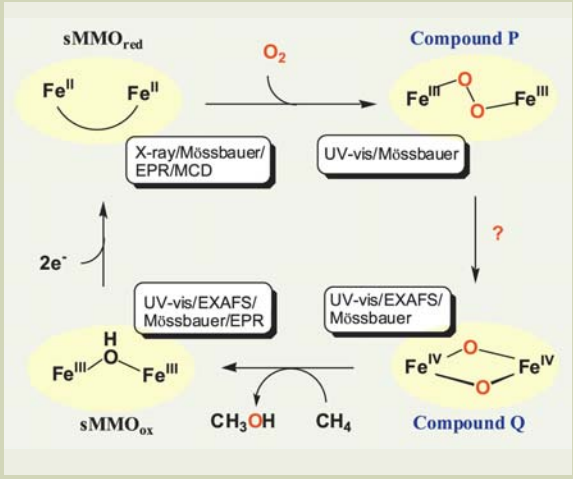

Scheme 3

metalloenzymes, we need mimic not only the active center structure but also the functions, and the structures must be preserved even in a solution under the reaction conditions. Consequently, in such a study, it is essential to determine structures of the metal complexes in a solution as well as to determine the crystal structures. In addition, it is widely recognized that, because a transition metal complex takes various structures depending on type and valence of metal and its coordination-binding form differs greatly, it is required for a newly synthesized metal complex to be subject to a single crystal X-ray structural analysis for the determination of its coordination structure and binding form. Furthermore, even when its crystal structure is revealed, its structure in a solution is not always the same as the crystal structure; therefore, clarification of the structure of the metal complex in a solution is also needed. In general, to determine the structure in a solution, NMR is the most effective method, but many transition metal complexes exhibit paramagnetic property, making the use of NMR difficult compared to the cases of analyzing organic compounds. On the other hand, mass spectrometry (MS) by soft ionization can determine masses of metal complexes regardless of metal property, giving very useful information in the structural determination of metal complexes. In particular, Electro- and Cold-Spray Ionization Time-of-Flight mass spectra can detect molecular ion peaks even from short-life complexes such as labile metal complexes and reactive intermediates. Thus, this method is significantly useful for the study of structures and functions of metal complexes.

Development of highly functionalized metal complexes supported by dinucleating ligands having a 1,2-bis(2-pyridyl)ethane common moiety [23]

In this chapter, we show synthetic studies of dinucleating ligands L1, L2 and L3, all of which have a 1,2-bis(2-pyridyl)ethane moiety as a common motif, and describe the synthesis, structure, and a phosphoester hydrolytic activity of the copper complexes supported by such ligands. We also show that Electro- and Cold-Spray Ionization Time-of-Flight mass spectra are effective for structural characterization of polynuclear metal complexes in a solution and the active species for the phosphoester hydrolysis.

Synthesis of new ligands L1, L2 and L3 having a 1,2-bis (2-pyridyl)ethane common moiety

As synthetic intermediates for obtaining ligands L1, L2 and L3, we synthesized 1,2-bis (2-formyl-6-pyridyl)ethane and 1,2-bis(2-bromomethyl-6-pyridyl)ethane. Syntheses of these compounds were already reported, but conventional methods required many reaction steps and the total yield was hopelessly low [23], [13]. To solve these problems, we developed a new synthetic route. **Scheme 4** shows the reaction pathway of the new synthesis. Compounds shown in **Scheme 4** are useful synthetic intermediates that can also be applied to various polydentate ligands having a 1,2-bis(2-pyridyl)ethane common moiety.

First, 1,2-bis(2-bromo-6-pyridyl)ethane was prepared by homo-coupling of 2-bromo-6-picoline. Next, after treating 1,2-bis(2-bromo-6-pyridyl)ethane with *n*-butyl lithium, an excess amount of DMF was added, then 1,2-bis(2-formyl-6-pyridyl)ethane was obtained in a 86% yield. Furthermore, 1,2-bis(2-formyl-6-pyridyl)ethane was reduced by $NaBH_4$ to the alcohol, the hydroxy groups of which was converted to Br groups to afford 1,2-bis(2-bromomethyl-6-pyridyl)ethane quantitatively. In the conventional synthesis, eight step reactions starting with 2,6-lutidine were required, and the total yield was less than 1% [24].

Schemes 5 and **6** show the reactions in which amines are introduced into both sides of the 1,2-bis(2-pyridyl)ethane moiety. An excess amount of dimethylamine or piperidine was added to 1,2-bis(2-bromomethyl-6-pyridyl) ethane to give L1 and L3 almost quantitatively. In the synthesis of L3, 1,2-bis(2-formyl-6-pyridyl)ethane was reacted with 2-aminomethylpyridine, and the Schiff's base

generated was reduced to give 1,2-bis (2-((*N*-pyridylmethyl) aminomethyl-6-pyridyl)ethane. Finally, the resultant amine was methylated. The total yield for L1-L3 was 40 to 60% starting with 2-bromo-6-picoline. As mentioned before, the total yield for L1-L3 by the conventional synthesis is less than 1%, demonstrating that new method is significantly effective compared to conventional ones.

Synthesis of copper complexes with L1, L2 and L3 and their structures

L1 and L2 form monocopper complexes $[Cu(L1)(Cl)](ClO_4)$ **(1)** and $[Cu(L2)(Cl)](ClO_4)$ **(2)**. On the other hand, L3 binds two Cu(II) ions. At this synthesis, L3 incorporates phosphodiester and phosphomonoester, forming a dicopper(II) complex $[Cu_2(L3)((PhO)_2PO_2)_2](ClO_4)_2$ **(3)** and a hexacopper(II) complex $[Cu_6(L3)_3(PhOPO_3)_4](ClO_4)_4$ **(4)**, respectively. Complex **4** is a hexanuclear complex that consists of three L3 ligands and six Cu(II) ions, as is found from its composition. Its crystal structure is shown in an ORTEP diagram (**Figure 5**).

The structures of complexes **3** and **4** in a solution were examined by Electro- and Cold-Spray Ionization Time-of-Flight mass spectra. In the Electrospray Ionization (ESI) mass spectra of complex **3**, only the peaks corresponding to dicopper complex were observed, revealed that the dinuclear structure is preserved in a solution and the structure is the same as the crystal structure. The Cold-Spray Ionization (CSI) mass spectra of complex **4** (**Figure 6**) showed a relatively sharp molecular ion peak at *m/z* 2724.9 which is attributed to $[M - ClO_4]^+$ and the main peak at m/z 1085.9 which is attributed to $[L3+3Cu+2(PhO)PO_3 + ClO_4]^+$. From the fact that a molecular ion peak with a relatively high intensity was observed, under this acquisition conditions, a hexanuclear structure of complex **4** is considered to be preserved even in a solution. The crystal structures and mass spectra of complexes **3** and **4** revealed that L3 ligand specifically stabilizes the dinuclear structures. On the other hand, copper complexes with L1 and L2 ligands were shown to be monocopper complexes from the result of a single-crystal X-ray structural analysis. In the ESI mass spectra of these complexes, however, the mass peaks corresponding to free L1 and L2 ligands where Cu ions were released from **1** and **2** were observed as the main peak, indicating that L1 and L2 ligands can not stabilize the copper coordination structure in a solution though they could form mononuclear copper complexes in the solid state.

As described above, CSI mass spectra have following some advantages. (1) If the stability of a complex is sufficiently high, even a complex with considerably large mass can be easily detected. (2) Depending on the stability of complex in a solution, mass peaks that correspond to the state of presence of chemical species in a solution can be detected. Moreover, if the stability of a complex in a solution is low even when this complex binds metal ions in the solid state, like complexes **1** and **2**, a free ligand was observed as the main peak in our present study. This result demonstrates that CSI mass spectra precisely show the structure in a solution. Consequently,

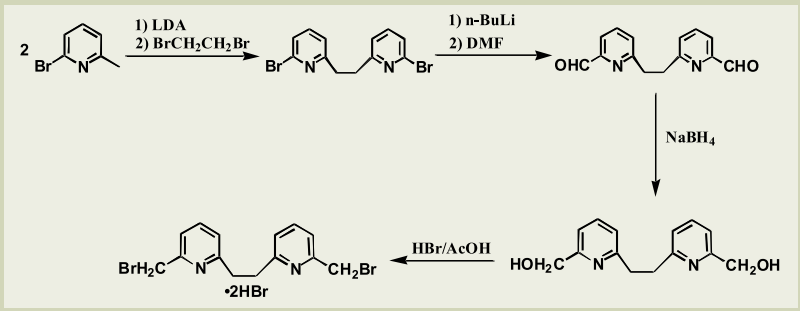

Scheme 4

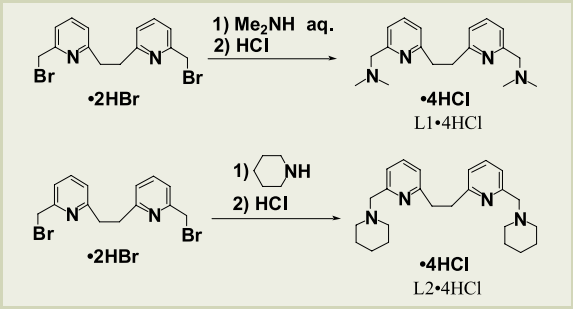

Scheme 5

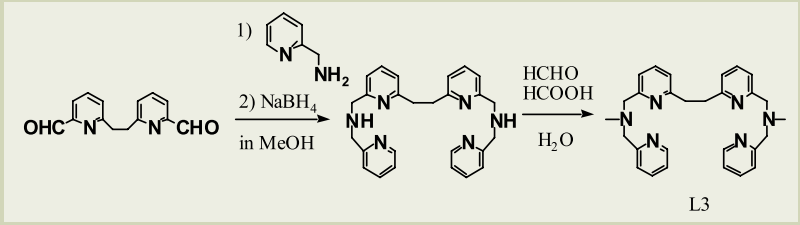

Scheme 6

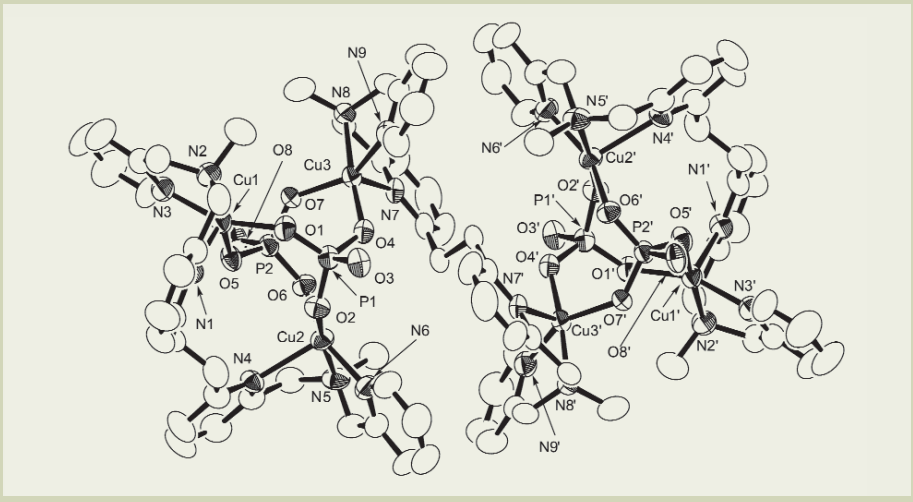

Fig. 5 ORTEP diagram of complex **4**.

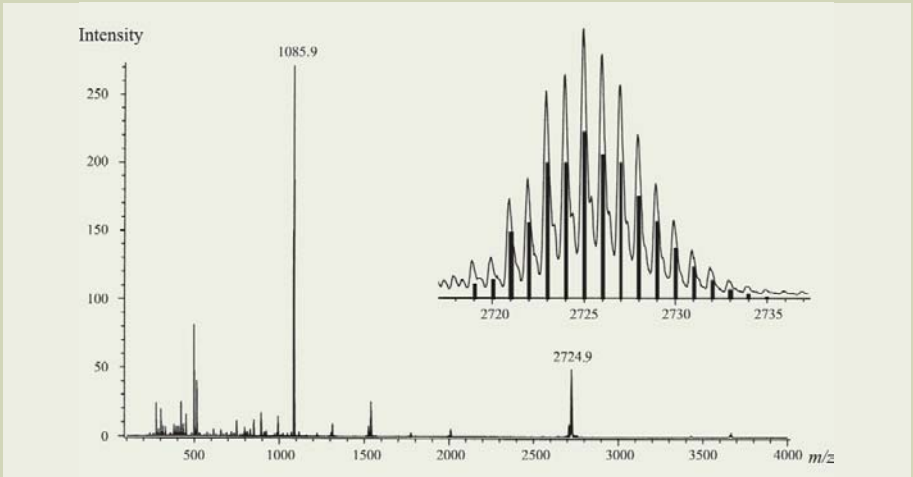

Fig. 6 CSI mass spectra of complex **4** in a MeCN solution at –30°C.

Electro- and Cold-Spray Ionization Time-of-Flight mass spectroscopy is a very effective analytical method that exactly shows the complex structure in a solution. It can be stated that this method is a powerful tool for determining the structures of metal complexes in a solution.

Hydrolysis of phosphoester by a dicopper complex supported by L3

The result of the CSI mass spectra of complexes **3** and **4** indicated that L3 ligand incorporates two Cu ions into it and forms a stable dinuclear structure in a solution. In this section, we demonstrate that L3 type dinucleating ligand is effective for developing highly functionalized metal complexes to model metalloenzymes having a dimetal center. Alkaline phosphatase (AP), which is an enzyme to hydrolyze phosphomonoester, has two Zn ions at the active center and these two Zn ions operate cooperatively for hydrolysis. We used a dicopper complex supported by L3 as a highly functionalized metal complex to reproduce the structure and functions of AP. Through this study, we found that CSI mass spectra are significantly effective for detecting reactive intermediates.

A dicopper(II) complex supported by L3 was synthesized upon addition of L3 and copper perchlorate(II) (1 : 2, mol/mol) into a 30% MeCN-H_2O mixed buffer solution (pH 7.0-10). The structure of the complex was estimated from CSI mass spectra. **Figure 7A)** and **B)** show the CSI mass spectra of the dicopper complex supported by L3 measured in the positive mode and the negative mode. In the all of CSI mass spectra in **Figure 7A)** and **B)**, only dinuclear complexes were detected but free ligands or mononuclear Cu(II) complex were not detected at all. These results clearly indicate that, at pH 7.0-10.0, L3 ligand specifically stabilizes the dinuclear structure under the reaction conditions shown above. Furthermore, we carried out detailed examination of CSI mass spectra obtained under conditions where pH of the solution was increased from 7 to 10, and we clarified what complex was formed due to the change of pH. The positive mode spectra in **Figure 7A**) firstly showed that, at pH 7, the main peak appeared at *m/z* 793 which corresponds to $\{[Cu_2(L3)(OH)](ClO_4)_2\}^+$ having a complex composition where one OH ion is incorporated into a dicopper complex of L3. Under the conditions where pH > 8, a large peak appeared at *m/z* 711 which corresponds to $\{[Cu_2(L3)(OH)_2](ClO_4)\}^+$ having a composition where two OH ions are incorporated into a dicopper complex. Moreover, looking at the negative mode spectra shown in **Figure 7B**), a large peak appeared at *m/z* 809 which corresponds to $\{[Cu_2(L3)(O)(OH)](ClO_4)_2\}^-$ having a composition where both a OH and a O^{2-} are incorporated into a dicopper unit. As is presented here, under the conditions where pH is 7 or more, the formation of complexes in a solution can be evaluated quantitatively to some extent.

In order to examine the hydrolytic activity of a monocopper complex **2** supported by L2 and of a dicopper(II) complex supported by L3 as a functional model of AP, the hydrolysis rate of tris(p-nitrophenyl)phosphate (TNP) was measured. **Figure 8** shows the pseudo-first order TNP hydrolysis rate constants k_{obs} plotted against pH in the range of pH 7.0-10 for the dicopper(II) complex of L3 and the monocopper complex **2** of L2. The dicopper(II) complex of L3 greatly accelerated the TNP hydrolysis for pH 8.0-10, leading to a rapid increase of the rate constant k_{obs} along with the increase of pH. On the other hand, the TNP hydrolysis rate constant k_{obs} for the monocopper complex **2** was almost constant to be 3.09 to 3.72 $\times 10^{-3}$ s^{-1} for pH 8.0-10. Since the TNP hydrolysis rate constants k_0 measured with buffer solutions in blank experiments are 1.20 to 1.30$\times 10^{-3}$ s^{-1} for pH 7.0-10, the acceleration of the TNP hydrolysis rate constant k_{obs} for the monocopper complex **2** is only approximately three times as compared with that obtained in the blank experiment. Furthermore, as a blank experiment, the hydrolysis rate constant was measured under conditions where only L3 or $Cu(ClO_4)_2$ was added. In this experiment, the rate constants for pH 9.0 were 1.24 $\times 10^{-3}$ s^{-1} and 1.30 $\times 10^{-3}$ s^{-1}, respectively, indicating that these values were almost the same as k_0 shown above. Thus, the dicopper complex of L3 accelerates the TNP hydrolysis by ca. 50 times at most as compared to the blank experiment. These results show that the dicopper(II) complex of L3 peculiarly accelerates TNP hydrolysis.

In order to examine what complexes were formed in the hydrolysis with the dicopper(II) complex of L3 when increasing pH, the pH change of a solution was measured when an aqueous NaOH solution was gradually added to the solution containing the dicopper(II) complex of L3. **Figure 9** shows a pH titration curve obtained at this measurement. It is found that 1, 2, 3, and 4 equivalent NaOH was consumed at pH up to 6.0, 7.5, 9.0, and 11, respectively. This suggests that, at pH 6.0, 7.5, 9.0, and 11, 1, 2, 3, and 4 equivalents of OH^- ions were incorporated into a dicopper complex $[Cu_2(L3)]^{4+}$, suggesting formation of four kinds of dicopper(II) complexes.

As was shown in the CSI mass spectra in **Figure 7**, at pH 7.0, 8.0, 9.0, and 10, three main peaks were detected. In the positive mode spectrum at pH 7.0, a large peak appeared at *m/z* 793 which corresponds to

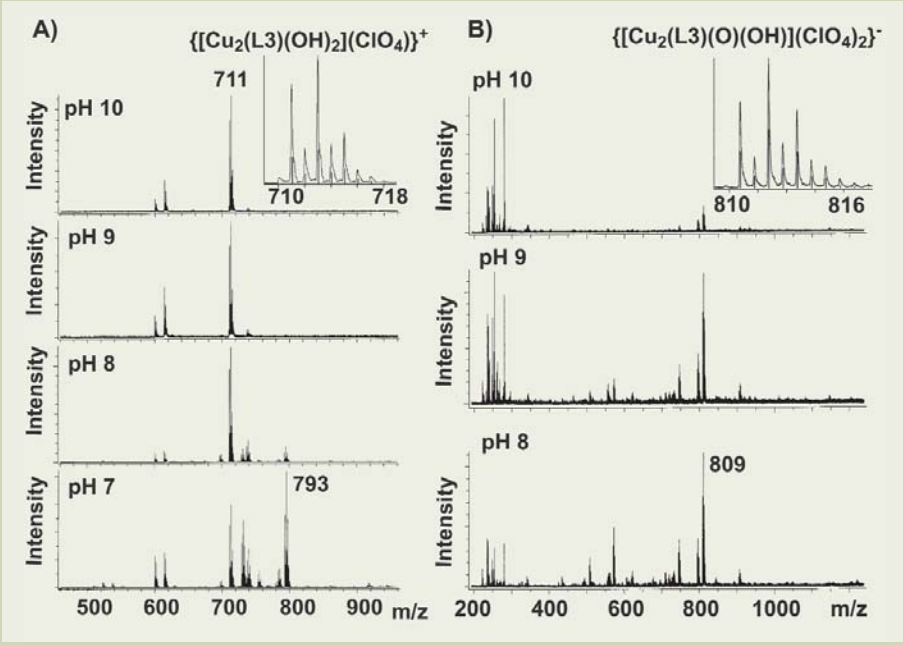

Fig. 7 CSI mass spectra of a dicopper complex with L3 ligands in a 30% MeCN/H_2O solution at 0°C. (A was obtained in the positive mode, and B was obtained in the negative mode.)

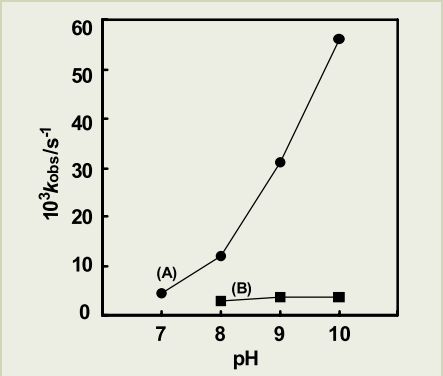

Fig.8 The pH dependence of TNP hydrolysis rate constant in a 30% MeCN/H_2O solution at 25°C. [(A) dicopper complex with L3 ligands, (B) complex **2** supported by L2]

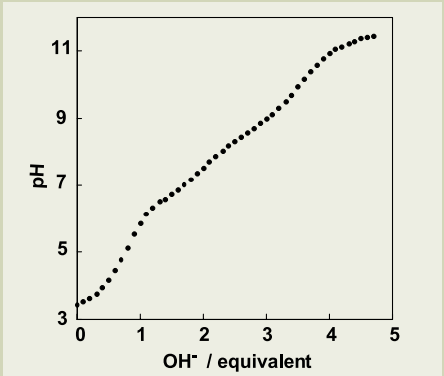

Fig.9 The pH titration curve of dicopper(II) complex in a 30% MeCN/H_2O solution at 25°C. The pH change was measured when an aqueous NaOH solution was added dropwise to the solution containing the dicopper complex of L3.

$\{[Cu_2(L3)(OH)](ClO_4)_2\}^+$, and a small peak appeared at *m/z* 711 which corresponds to $\{[Cu_2(L3)(OH)_2](ClO_4)\}^+$. At pH 8.0 or more, in the positive mode spectra, only a large peak was observed at *m/z* 711. In the negative mode spectra, at pH 8.0 or more, a large peak was detected at *m/z* 809 which corresponds to $\{[Cu_2(L3)(O)(OH)](ClO_4)_2\}^-$. These results imply that three species, $\{[Cu_2(L3)(OH)](ClO_4)_2\}^+$, $\{[Cu_2(L3)(OH)_2](ClO_4)\}^+$, and $\{[Cu_2(L3)(O)(OH)](ClO_4)_2\}^-$, are formed when 1, 2, and 3 equivalents of OH^- ions are incorporated into $[Cu_2(L3)]^{4+}$ complexes, respectively. This result agrees with the result of the pH titration where 3 equivalents of OH^- ions are consumed at pH 9.0. In these CSI mass spectra, two large peaks, which were observed at m/z 711 and *m/z* 809 for pH 8.0 and 9.0, decrease at pH 10. This suggests that a dicopper(II) complex that incorporated 4 equivalents of OH^- ions is present at pH 10. However, we could not detect the peak of this complex in CSI mass spectra presumably due to the fact that this complex is unstable and an electrically neutral complex. From the results of the pH titration and the measurement of the CSI mass spectra, the active species for the TNP hydrolysis at pH 8.0 and 9.0 is estimated to be $[Cu_2(L3)(O)(OH)]^+$. Since the TNP hydrolysis rate further accelerates at pH 10, a dicopper(II) complex $[Cu_2(L3)(O)(OH)_2]$ that incorporated 4 equivalents of OH^- ions into $[Cu_2(L3)]^{4+}$ may be formed as a more highly active complex. As was described so far, CSI mass spectra give significantly useful information for identifying generally reactive species.

Development of a highly functionalized metal complex as a functional model of sMMO [25]

As shown in the first chapter, soluble methane monooxygenase (sMMO) is an enzyme that catalyzes monooxygenation of various hydrocarbons via dioxygen activation at the non-heme diiron center. Its high oxidation ability and unique dioxygen activation mechanism have been attracting interests of chemists and biochemists. We have developed various dinucleating ligands having a common 1,2-bis(2-pyridyl)ethane moiety to stabilize dinuclear complexes both in the solid state and in a solution. Such metal complexes can reproduce both structures and functions of metalloproteins having a dimetal center at the active site, and we call them highly functionalized metal complexes. Recently, we synthesized a diiron complex of a new dinucleating octadenetate ligand 6-hpa, which shows an efficient catalytic activity for epoxidation of alkene with H_2O_2 and forms a peroxodiiron complex as an intermediate, being a promising functional model of sMMO.

Synthesis of a dinucleating ligand 6-hpa and diiron complexes 5, 6, 7

In the second chapter, it was described that a hexadentate ligand having a 1,2-bis(2-pyridyl)ethane common moiety forms a dicopper complex, and the dinuclear structure is stable in a solution. Thus, the multidentate ligands having a 1,2-bis(2-pyridyl)ethane moiety

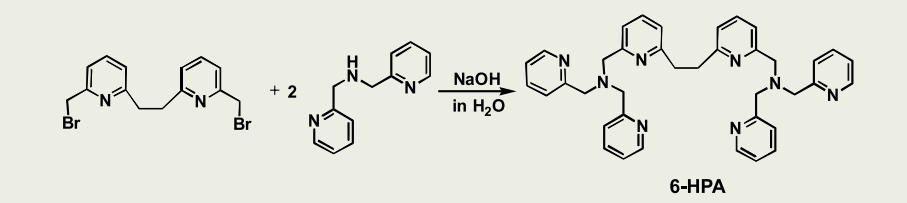

Scheme 7

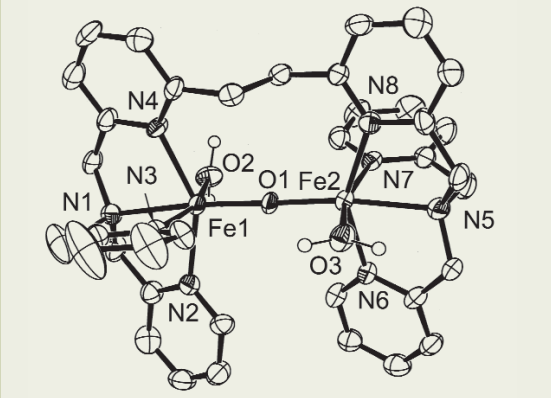

Fig. 10 ORTEP diagram of $[Fe_2(O)(H_2O)_2(6\text{-hpa})](ClO_4)_4$ (**5**)

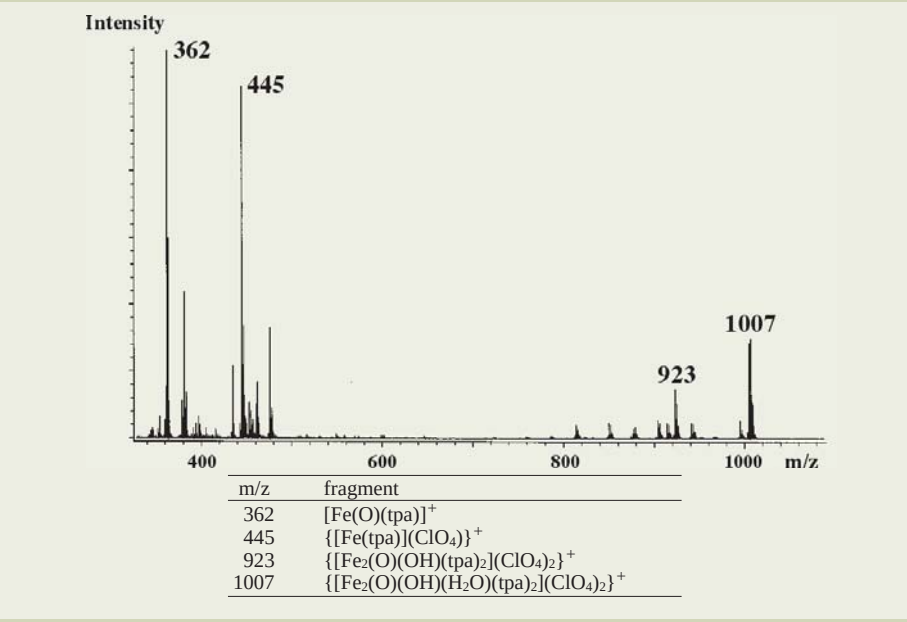

m/z	fragment
362	$[Fe(O)(tpa)]^+$
445	$\{[Fe(tpa)](ClO_4)\}^+$
923	$\{[Fe_2(O)(OH)(tpa)_2](ClO_4)_2\}^+$
1007	$\{[Fe_2(O)(OH)(H_2O)(tpa)_2](ClO_4)_2\}^+$

Fig. 11 ESI mass spectrum of diiron complex $[Fe_2(O)(H_2O)(tpa)_2](ClO_4)_4$ in a MeCN solution.

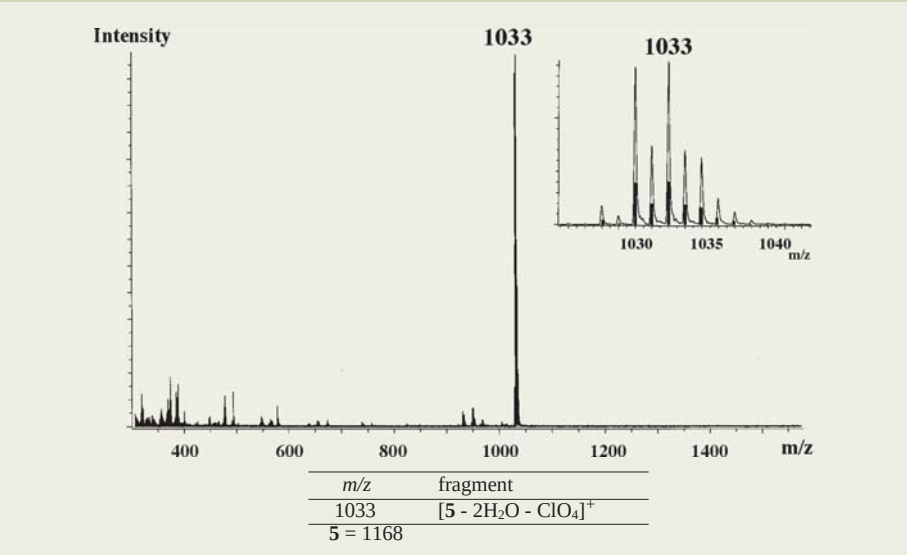

m/z	fragment
1033	$[\mathbf{5} - 2H_2O - ClO_4]^+$

5 = 1168

Fig. 12 ESI mass spectrum of diiron complex **5** in a MeCN solution.

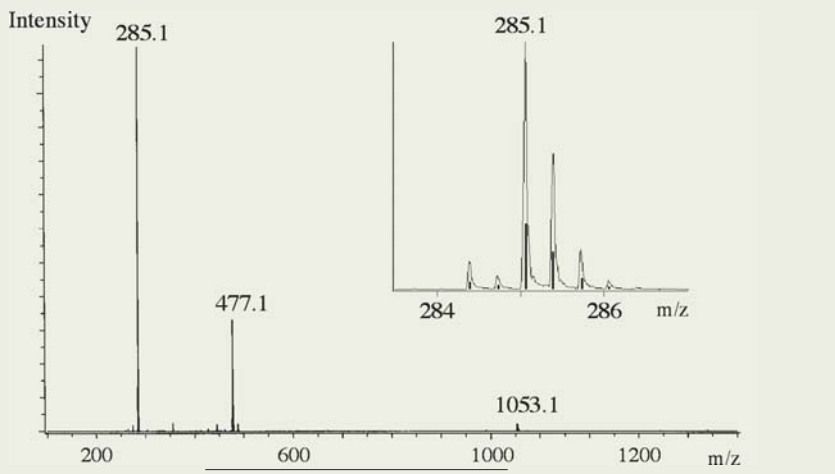

m/z	fragment
285.1	[**6** - 3ClO_4]$^{3+}$
477.1	[**6** - 2ClO_4]$^{2+}$
1053.1	[**6** - ClO_4]$^{+}$

6 = 1152

Fig. 13 ESI mass spectrum of diiron complex **6** in a MeCN solution.

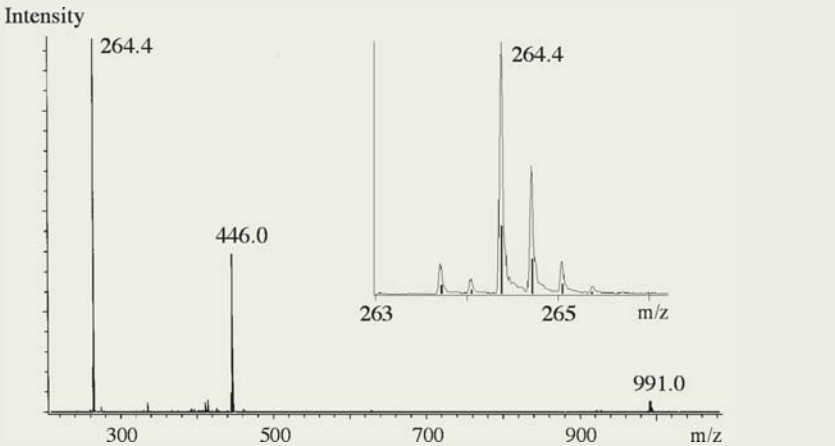

m/z	fragment
264.4	[**7** - 3ClO_4]$^{3+}$
446.0	[**7** - 2ClO_4]$^{2+}$
991.0	[**7** - ClO_4]$^{+}$

7 = 1090

Fig. 14 ESI mass spectrum of diiron complex 7 in a MeCN solution.

Table 1 Epoxidation reaction of cyclooctene by hydrogen peroxide where diiron complexes catalyze cyclooctene a)

H_2O_2	yield based on H_2O_2			total turnover	
complex	(equiv.)	epoxide	diol	number	ref.
[Fe^{III}_2(O)(H_2O)$_2$(6-hpa)](ClO_4)$_4$	10	75	2	8	this work
	40	72	3	30	this work
	150	70	2	110[b)]	this work
[Fe^{III}_2(O)(H_2O)$_2$(tpa)$_2$](ClO_4)$_4$	10	40	41	8	27e
[Fe^{II}(tpa)(MeCN)$_2$] (ClO_4)$_2$	10	34	40	7	27e
	40	26	37	25	27e
[Fe^{II}(6-Me_3-tpa)(MeCN)$_2$](ClO_4)$_2$	10	7	49	6	27e
	40	4	55	24	27e
[Fe^{II}(mep)(MeCN)$_2$](ClO_4)$_2$[c)]	50	30	0	15	28
[Fe^{II}(mep)(MeCN)$_2$](ClO_4)$_2$	10	75	9	8	27e
[Fe^{II}(mep)(MeCN)$_2$](SbF_6)$_2$	50	57	0	28	28

a) 0.7 mM complex, 7 mM H_2O_2 and 0.7 M cyclooctene in MeCN at r. t. H_2O_2 solution added by syringe pump over 30 min. b) Water generated was removed with molecular sieves. c) In the presence of 10 eq. of acetic acid.

may be useful for a functional model of sMMO. So we prepared a new dinucleating octadentate ligand 6-hpa, which was obtained from 1,2-bis(6-bromomethyl-2-pyridyl)ethane and bis(2-pyridylmethyl)amine almost quantitatively as shown in **Scheme 7**. The 6-hpa ligand has a structure that two tris(2-pyridylmethyl)amine (tpa) are connected by a -(CH_2CH_2)- spacer.

Three diiron complexes [Fe_2(O)(H_2O)$_2$(6-hpa)](ClO_4)$_4$ **(5)** and [Fe_2(O)(X)(6-hpa)](ClO_4)$_3$ (**6**: X = BzO, **7**: X = AcO) were synthesized with the 6-hpa ligand. The crystal structures of **5**-**7** were determined by X-ray analysis. The ORTEP diagram of **5** is shown in **Figure 10**.

As found from the ORTEP diagram of **5** shown in **Figure 10**, a 6-hpa ligand stabilizes a diiron core where two Fe ions are incorporated with an m-oxo-bridge. Similarly, for **6** and **7**, the crystal structures revealed that an μ-oxo-μ-carboxylatodiiron core is stabilized by a 6-hpa ligand. It is known that a tpa ligand that has a half-size structure of 6-hpa forms various diiron complexes similar to **5**-**7** [26]. In order to prove a structural similarity of **5**-**7** to the diiron complexes of tpa, their crystal structures are compared. The Fe•••Fe distances and the Fe-O-Fe angles of **5**-**7** were as follows: **5** (3.607Å, 179.0°), **6** (3.301Å, 132.7°), and **7** (3.287Å, 132.4°). These data are almost equal to the Fe•••Fe distances and the Fe-O-Fe angles of the corresponding diiron complexes of tpa with a small difference within 0.04Å and 4°, respectively, [26] demonstrating that **5**-**7** are similar to the corresponding diiron complexes of tpa in the crystal structures.

On the other hand, the diiron complexes of tpa are easily converted to monoiron complexes in a solution because the tpa ligand does not have any structural feature to stabilize dinuclear structure. We measured an ESI mass spectrum of a diiron(III) complex of tpa [Fe_2(O)(H_2O)(tpa)$_2$](ClO_4)$_4$ in a MeCN solution, which has a diiron core structure similar to that of **5** in the solid state. The ESI mass spectrum is shown in **Figure 11**. Mass peaks at 923 and 1007 correspond to diiron complexes, and those at 362 and 445 to monoiron complexes. Intensities of the mass peaks of the mononuclear species were much larger than those of dinuclear ones. This result indicates that the tpa complex exsits as a mixture of mono- and di-iron complexes in a MeCN solution and monoiron complexes rather than diiron complexes are present as the main species.

In order to examine the stability of the dinuclear structures of **5**, **6**, and **7**, their ESI mass spectra were measured in a MeCN solution (see **Figures 12**, **13** and **14**). In the ESI mass spectra, main peaks appears at *m/z* 1033 [**5**-2H_2O - ClO_4]$^{+}$, 285.1 [**6**-3ClO_4]$^{3+}$, and 264.4 [**7**-3ClO_4]$^{3+}$. These cations preserve the diiron core where counter cations are released from **5**-**7**. The observed isotope patterns of these peaks agree well with isotope patterns calculated from chemical compositions of {[Fe_2(O)(6-hpa)](ClO_4)$_3$}$^{+}$, [Fe_2(O)(BzO)(6-hpa)]$^{3+}$, and [Fe_2(O)(AcO)(6-hpa)]$^{3+}$. These results demonstrate that a 6-hpa ligand stabilizes the dinuclear structure in a MeCN solution.

Epoxidation of alkene with H_2O_2 catalyzed by the diiron complex 5

In the presence of **5**, 10 equivalents of

H_2O_2 were added to a MeCN solution of cyclooctene to give cyclooctene epoxide in a 75% yield based on H_2O_2 used. In the case of **6** and **7**, the epoxide was produced in a 51% and 63% yield, respectively. The reason why **5** gives the high yield in the epoxide production as compared with **6** and **7** is probably that H_2O ligand in 5 is replaced by H_2O_2 more easily than the BzO^- or AcO^- ligands binding in a bidentate bridging mode in **6** and **7**.

Reported data for cyclooctene oxygenation with H_2O_2 catalyzed by iron complexes of tpa, mep, and 6-Me_3-tpa ligands are shown in comparison with the results of **5** in **Table 1** [27], [28]. For the reaction of cyclooctene catalyzed by **5**, the epoxide and the 1,2-*cis*-diol were obtained in a 75% and a 2% yields based on H_2O_2 used, respectively. For the yield of epoxide, **5** is as good as an iron complex of mep ligand $[Fe^{II}(mep)(MeCN)_2](ClO_4)_2$ known as an excellent epoxidation catalyst [27]. Que et al. reported that the epoxide and the 1,2-*cis*-diol were formed in a 40% and a 41% yields based on H_2O_2 used when 10 equivalents of H_2O_2 was added to $[Fe^{III}_2(O)(H_2O)_2(tpa)_2](ClO_4)_4$ [27f]. As described above, the diiron complex of tpa exists as a mixture of mono- and di-iron complexes in a MeCN solution. This may be the reason for the formation of both epoxide and 1,2-*cis*-diol in a 1:1 ratio. In the case of an iron complex of 6-Me_3-tpa ligand having a steric hindrance, the yield of the epoxide is decreased to 7 % and that of the 1,2-*cis*-diol is slightly increased to 49% [27f]. It is considered that the 6-Me_3-tpa ligand prefers mononuclear structure because the steric hindrance destabilizes dinuclear structure. Thus, a dinuclear structure stable in a solution may be essential for the predominant epoxidation. Next, in order to examine the durability of **5** as an epoxidation catalyst, the epoxidation of cyclooctene was carried out using a large excess amount of H_2O_2. When 150 equivalents of H_2O_2 were stepwise added to a MeCN solution of cyclooctene in the presence of **5**, the epoxide is formed predominantly and the total turnover number is increased up to 110. Que et al. reported that for the oxygenation of cyclooctene catalyzed by the iron tpa complexes using 40 equivalents of H_2O_2, total turnover number is at most 24 [27f]. Jacobsen et al. reported that total turnover numbers of the epoxidation of various alkene catalyzed by the mep complexes with 50 equivalents of H_2O_2 are in a range of 15-28 [27f]. The large turnover number of **5** as compared with the iron complexes of tpa and mep ligands indicates that the 6-hpa ligand can preserve the dinuclear structure even under the catalytic oxidation conditions.

Cyclooctene, octene, 1-octene, styrene, *cis*-β-methylstyrene and *trans*-β-methylstyrene were used as substrates for the reaction catalyzed by **5**, and the corresponding epoxides were obtained predominantly. In particular, when using *trans*-β-methylstyrene, the epoxide was formed in a yield exceeding 90% based on H_2O_2 used. On the other hand, for the iron complexes of tpa-type ligands, 1,2-*cis*-diol is mainly produced [27f]. Consequently, it can be stated that **5** is an excellent functional model of sMMO that catalyzes a predominant epoxidation. In epoxidation catalyzed by **5**, the lower the ionization potential of alkene is, the higher the yield is. The ionization potential means energy necessary for one electron oxidation [29]. Thus, the rate-determining step of the epoxidation by **5** may be one-electron oxidation of alkene, suggesting that a cation radical of alkene is generated as an intermediate in the reaction. We examined a stereo-selectivity in the epoxidation catalyzed by **5**. When using *cis* or *trans* alkene as substrates, *cis* or *trans* epoxides can be produced. RC is a parameter that shows how much stereo is preserved in the epoxide when *cis* or *trans* alkene is used. A 100% RC indicates that the epoxidation is completely stereospecific. A 0% RC shows that both the *trans* and *cis* epoxides are formed in a 1:1 ratio. In the case of *trans*-β-methylstyrene, RC was 99% or more. On the other hand, RC was 63% in the case of *cis*-β-methylstyrene, indicating that part of *cis*-β-methylstyrene was converted to a *trans* form in the epoxidation process. This result supports the proposed mechanism for the radical cation intermediate. 63% of the RC value implies that a conversion to the *trans* form is not completed and O-atom transfer rate is almost comparable to a rotation rate of the carbon-carbon bond in the cation radical intermediate.

Mechanisms for dioxygen activation and epoxidation catalyzed by the complex 5

From the epoxidation, it is found that **5** is an excellent functional model that reproduces the reactivity of sMMO. Thus, through mechanistic studies of the epoxidation catalyzed by **5**, we may give new insights into the dioxygen activation mechanism for sMMO. The reaction of **5** with H_2O_2 was monitored by spectroscopic methods to detect reactive intermediates. Upon addition of H_2O_2 to a MeCN solution of **5** at –40°C, the solution turned green. The UV-vis spectrum of the green species shows absorption bands at 490 nm (ϵ; 1130 dm^3 mol^{-1} cm^{-1}), 670 nm (ϵ; 1060 dm^3 mol^{-1} cm^{-1}), and 882 nm (ϵ; 370 dm^3 mol^{-1} cm^{-1}), similar to that of a μ-peroxodiiron(III) complex of 6-Me_3-tpa $[Fe_2(O)(O_2)(6\text{-}Me_3\text{-}tpa)_2](ClO_4)_2$ reported by Que et al. [30]. In addition, both the green species and the peroxodiiron complex of tpa are ESR silent. Thus, it is suggested that the green species generated from **5** is a μ-peroxodiiron(III) complex

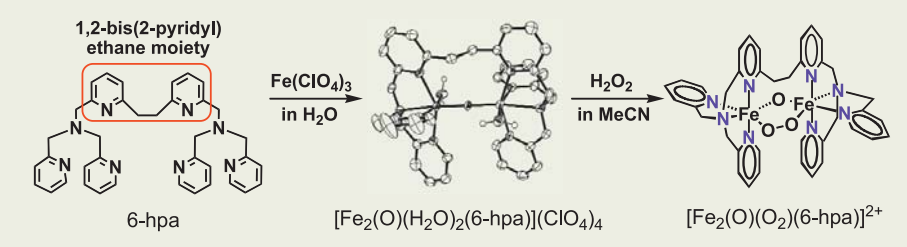

Scheme 8

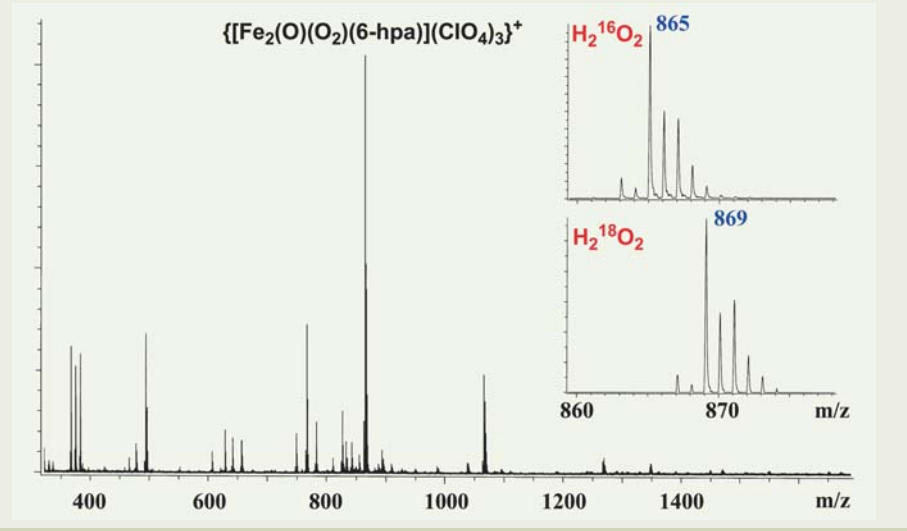

Fig. 15 CSI mass spectrum of peroxodiiron complex **8** in a MeCN solution at -40°C.

Table 2 ^{18}O-label experiment result of the epoxidation reaction of *trans*-β-methylstyrene supported by hydrogen peroxide affording the catalytic reaction of complex **5**.

	H_2O_2 equiv.	epoxide - ^{18}O%
$[Fe_2(O)(H_2O)_2(6\text{-}hpa)]^{4+}$ (**5**)	10 eq.	93.7 ±1.5
theoretical value		95
$[Fe_2(^{18}O)(H_2{}^{18}O)_2(6\text{-}hpa)]^{4+}$ (m-^{18}O-**5**)	1 eq.	31.4±1.5
theoretical value		33
$[Fe_2(^{18}O)(H_2{}^{18}O)_2(6\text{-}hpa)]^{4+}$ (m-^{18}O-**5**)	3 eq.	16.6 ±2.0
theoretical value		16

$[Fe_2(O)(O_2)(6\text{-hpa})](ClO_4)_2$ **(8)**. The formation of **8** via **5** is schematically shown in **Scheme 8**.

We measured a CSI mass spectrum of the peroxodiiron complex **8**. In the CSI mass spectrum, the main peak appears at *m/z* 869 corresponding to $\{[Fe_2(O)(O_2)(6\text{-hpa})](ClO_4)\}^+$. This peak shifts by +4 units when $H_2{}^{18}O_2$ was used instead for $H_2{}^{16}O_2$ (**Figure 15**). In addition, the isotope pattern of this peak agrees well with an isotope pattern calculated from $\{[Fe_2(O)(O_2)(6\text{-hpa})](ClO_4)\}^+$. These spectral data strongly indicate that the peroxodiiron(III) complex **8** was generated from **5** and H_2O_2 in a MeCN solution. Generaly, peroxodiiron complexes are unstable and cannot be detected with conventional MS methods. On the other hand, the CSI MS is a very effective soft-ionization method and it can directly measure reactive composites. Since **5** forms the peroxo intermediates and catalyzes an efficient epoxidation of alkene, it can be said that **5** is a highly functionalized metal complex to reproduce the functions of sMMO.

In order to clarify the mechanism for the activation of the peroxo intermediate **8**, ^{18}O-labeling experiments with $H_2{}^{18}O_2$ were carried out for epoxidation catalyzed by **5**. The results are shown in **Table 2**. When 10 equivalents of $H_2{}^{18}O_2$ was added to a MeCN solution of *trans*-β-methylstyrene in the presence of **5**, ^{18}O-atom was incorporated into 94% of epoxide. This result clearly showed that the O-atom of H_2O_2 is incorporated into epoxide but it is not 100%. This suggested that the O-atom of μ-oxo bridge in **5** is incorporated into the epoxide. So, the μ-oxo bridge of **5** was labeled with ^{18}O-atom to obtain μ-^{18}O-5, and *trans*-β-methylstyrene was epoxidized with μ-^{18}O-**5** and $H_2{}^{16}O_2$. Upon addition of 1 and 3 equivalents of $H_2{}^{16}O_2$ to μ-^{18}O-**5**, the yields of ^{18}O-epoxide were 31% and 17%, respectively. These results indicate that three O-atoms composed of an μ-oxo and a μ-peroxo become equivalent in the active species formed from **8** and one of the three O-atoms is incorporated into the epoxide. The active species possesses a structure where the three O-atoms can be scrambled. Possible active species is a dioxo-μ-oxodiiron(IV) complex $[FeIV_2(O)_2(\mu\text{-}O)(6\text{-hpa})]^{2+}$ that can be formed by homolytic scission of the O-O bind of **8**. The incorporation of 33% ^{18}O-atom into the epoxide using μ-^{18}O-**5** and $H_2{}^{16}O_2$ is schematically shown in **Scheme 9**. Considering from the chemical structure of dioxo-μ-oxodiiron(IV) complex, it seems reasonable that the three O-atoms scramble one another.

In order to investigate the epoxidation mechanism, two different ^{18}O-labeling experiments were performed for the epoxidation of *trans*-β-methylstyrene catalyzed by **5**. In an experiment, an excess amount of ^{18}O-labeled water ($H_2{}^{18}O$) was added, whereas another one was carried out under an $^{18}O_2$-atmosphere. The results are shown in **Table 3**. For the experiment under an Ar atmosphere where 10 equivalents of $H_2{}^{16}O_2$ and 1000 equivalents of $H_2{}^{18}O$ were added to **5**, only 1.5% of epoxide was ^{18}O-labeled. This suggests that O-atom exchange between H_2O and either μ-peroxo complex **8** or dioxo-μ-oxodiiron(IV) active species is much slower than the O-atom transfer from the active species to the alkene. Similar experiment was carried out with the iron complex of tpa, ^{18}O-atom is incorporated into epoxide in a much more high rate [27c]. This fact suggests that a catalytic reaction of **5** progresses in a mechanism different from that for iron complex of tpa. Since μ-oxodiiron core structure of the active species generated from **5** is stabilized by 6-hpa, the O-atom exchange with H_2O might become difficult. Next, when an epoxidation reaction was performed under an $^{18}O_2$ atmosphere, ^{18}O-atom was incorporated into 5% of epoxide upon addition of 10 equivalents of $H_2{}^{16}O_2$ to 5. This demonstrates that some species, which can react with $^{18}O_2$ molecule, exist in this epoxidation system. One of possible candidates is a cation radical generated by one-electron oxidation of alkene. Practically, the incorporation of ^{18}O is as low as 5%, and thus, the most O-atom transfer reaction proceeds via an O-atom rebound mechanism in a solvent cage including both alkene and the active species. It is considered that an extremely small amount of the cation radical departs from the solvent cage to react with $^{18}O_2$ molecule, resulting in a generation of ^{18}O labeled epoxide.

Scheme 10 shows an epoxidation mechanism that satisfies these results. We can estimate the following reaction mechanism. First, a diiron(III) complex **5** reacts with H_2O_2 to form a peroxo intermediate **8**. Then, the O-O bond of the peroxo intermediate is homolytically cleaved, generating a dioxo-μ-oxoiron(IV) complex as an active species. The substrate alkene is one-electron oxidized by the active species to give diiron(III, IV) complex and the cation radical in a solvent cage. The O-atom transfer from the diiron(III, IV) complex to the cation radical occurs in the solvent cage to afford the epoxide.

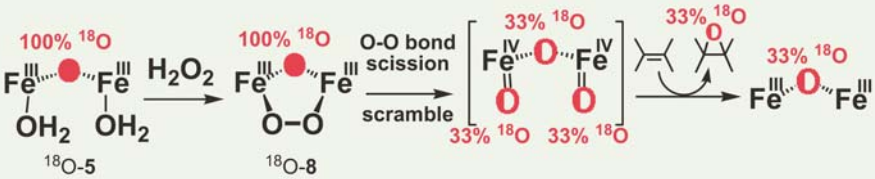

Scheme 9

Table 3 ^{18}O-isotope label experiment result of the epoxidation reactions of alkene supported by $H_2{}^{18}O_2$, $H_2{}^{18}O$ and $^{18}O_2$ that afford the catalytic reaction of various iron complexes.

	epoxide - ^{18}O%		
complex	10eq. of $H_2{}^{18}O_2$	1000eq. of $H_2{}^{18}O$	$^{18}O_2$
$[Fe^{III}_2(O)(H_2O)_2(6\text{-hpa})]^{4+}$ a) (**5**)	93.7±1.5	1.5±0.5	4.9±0.5
$[Fe^{II}(tpa)(MeCN)_2]^{2+}$ b)	90	9	1
$[Fe^{II}(6\text{-Me}_3\text{-tpa})(MeCN)_2]^{2+}$ b)	54	3	43
sMMO c)		0.5 d)	99 e)

a) substrate: trans-β -methylstyrene 10 eq. of H_2O_2. b) substrate: cyclooctene. 10 eq. of H_2O_2. c) substrate: methane. d) The potassium phosphate buffer containg [^{18}O]water(19.0 atom% excess of ^{18}O)was used. e) The reaction was carried out under 55.93 atom% excess of $^{18}O_2$ atmosphere.

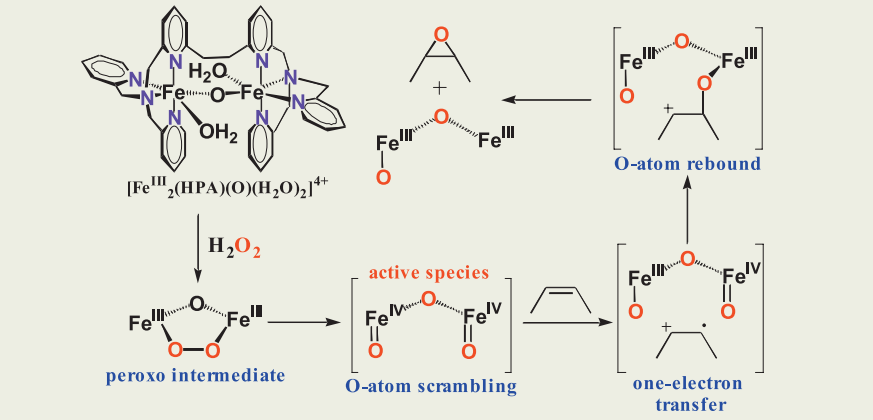

Scheme 10

Conclusion

As shown in the second chapter, a dinucleating ligand L3, which has a 1,2-bis(2-pyridyl)ethane moiety, binds two Cu ions, and stabilizes the dinuclear structure both in the solid-state and in a solution. The dicopper complex of L3 greatly accelerates a phosphoester hydrolysis. When pH of a solution of this complex is increased, the dicopper complex incorporates OH^- ions, forming some active

species. In particular, the complexes that incorporate three or four OH^- ions are very reactive, resulting in high activity for the hydrolysis of the phosphoester at pH 9 and 10. On the other hand, when mononuclear copper complex is used, the hydrolysis is hardly accelerated. Therefore, we can say that the dinuclear copper complex of L3 is a highly functionalized metal complex to reproduce the functions of alkaline phosphatase (AP).

In the third chapter, a 6-hpa ligand having a 1,2-bis(2-pyridyl)ethane moiety is used, and it is described that a diiron complex of 6-hpa **(5)** is an excellent functional model of sMMO. The complex **5** catalyzes oxygenation of alkene by H_2O_2, to afford epoxide predominantly, and gives a high turnover number of 110. Moreover, for epoxidation of *trans*-β-methylstyrene, the yield is as high as 91%. The dinuclear structure of **5** is preserved even under the catalytic conditions. Upon addition of H_2O_2 to **5** at –40°C, a μ-oxo-μ-peroxodiiron(III) complex **8** is quantitatively generated. From the ^{18}O-labeling experiments, it is revealed that **8** is converted to an active species, dioxo-μ-oxoiron(IV) complex $[FeIV_2(O)_2(m\text{-}O)(6\text{-}hpa)]^{2+}$, via a homolytic O-O bond scission. In addition, it is suggested that the epoxidation proceeds via a radical cation intermediate. The present diiron complexes of 6-hpa are different from conventional sMMO models. That is, they can stabilize a μ-oxodiiron core without any endogenous bridging group. Consequently, we can say that the diiron complex of 6-hpa is a highly functionalized metal complex capable of reproducing the functions of sMMO. Through these studies, we revealed a dioxygen activation mechanism via a μ-peroxo complex and proposed a dioxo-μ-oxoiron(IV) complex as an active species.

Through our studies, it is demonstrated that Electro- and Cold-Spray Ionization Time-of-Flight mass spectra are significantly useful for the characterization of the structures of polynuclear metal complexes in a solution. We found that the utility of the spectra is very high, making it possible not only to investigate the stability of these metal complexes, but also to provide conclusive evidence in the detection of reactive intermediates. Thus, these spectra can be widely applied as powerful measurement tool in the research and development of highly functionalized metal complexes to reproduce the functions of metalloenzyme.

References

[1] (a) Handbook of Metalloproteins in A. Messerschmidt, R. Huber, T. Poulos, and K. Wieghardt, Ed., 2, Wiley, New York, 2001. (b) Kodera, M. and Kano, K., *Bull. Chem. Soc., Jpn., Accounts*, **80**, 662 (2007).

[2] Malmstrom, B. G. *Annu. Rev. Biochem.*, **51**, 21 (1982).

[3] (a) Dawson, J. H.; Sono M. *Chem. Rev.*, **87**, 1255 (1987). (b) Sono, M.; Roach, M. P.; Coulter, E. D.; Dawson, J. H., *Chem. Rev.*, **96**, 2841 (1996).

[4] (a) Feig, A. L.; Lippard, S. J. *Chem. Rev.*, **94**, 759 (1994). (b) Lippard, S. J. *Angew. Chem. Int. Ed. Engl.*, **27**, 344 (1989).

[5] M. Kodera, K. Kano, and T. Funabiki, "Nonheme Monooxygenases"; ed by T. Funabiki, KLUWER ACADEMIC PUBLISHERS, **19**, pp. 283 (1997).

[6] (a) Marota, J. J. A.; Shiman, R. *Biochemistry*, **23**, 1303 (1984). (b) Kaufman, S. *Adv. Ensymol.*, **35**, 245 (1971). (c) Fisher, D. B.; Kirkwood, R.; kaufman, S. J. *Biol. Chem.*, **247**, 5161 (1972). (d) Wallick, D. W.; Bloom, L. M.; Gaffney, B. J.; Benkovic, S. J. *Biochemistry*, **23**, 1295 (1984).

[7] Levitt, M.; Spector, S.; Sjoerdsma, A.; Udenfriend, S. *Pharmacol. Exp. Ther.*, **148**, 1 (1965).

[8] Haavik, J.; Petersson, L.; Flatmark, T. *Biochim. Biophys. Acta*, **953**, 142 (1988).

[9] (a) Baldwin, J. E.; Bradley, M. *Chem. Rev.*, **90**, 1079 (1990). (b) White, R. J.; John, E.-M. M.; Baldwin, J. E.; Abraham, E. P. *Biochem. J.*, **203**,791 (1982). (c) Bainbridge, Z. A.; Scott, R. I.; Perry, D. J. *Chem. Tech. Biotechnol.*, **55**, 233 (1990).

[10] (a) Fujishima, Y.; Nordland, P.; Pelosi, G.; Schofield, C. J.; Cole, S. C.; Baldwin, J. E.; Hajdu, J. *J. Mol. Biol.*, **242**, 712 (1994). (b) Roach, P. L.; Schofild, C. J.; Baldwin, J. E.; Clifton, I. J.; Hajdu, J., *Protein Sci.*, **4**, 1007 (1995). (c) Roach, P. L.; Clifton, I. J.; Fulop, V.; Harlos, K.; Barton, G. J.; Hajdu, J.,; Andersson, I.; Schofild, C. J.; Baldwin, J. E., *Nature*, **375**, 700 (1995).

[11] (a) Colby, J.; Dalton, H.; Whittenbury, R. *Ann. Rev. Microbiol.*, **33**, 481 (1979). (b) Dalton, H. In Biotechnology Handbook 5 "Methane and Methanol Utilizers"; J. C. Murrell and H. Dalton, Ed.; Plenum Press: New York, (1992); Vol. Biotechnology Handbook 5; pp 85.

[12] (a)Colby, J.; Dalton, H. *Biochem. J.*, **171**, 461 (1978). (b) Patel, R. N.; Savas, J. C. *J. Bacteriol.*, **169**, 2313 (1987). (c) Fox, B. G.; Froland, W. A.; Dege, J. E.; Lipscomb, J. D. *J. Biol. Chem.*, **264**, 10023 (1989). (d) Pilkington, S. J.; Dalton, H. *FEMS Microbiol. Lett.*, **78**, 103 (1991). (e) Nakajima, T.; Uchiyama, H.; Yagi, O.; Nakamura, T. *Biosci. Biotech. Biochem.*, **56**, 736 (1992).

[13] Higgins, I. J.; Best, D. J.; Hammond, R. C. *Nature*, **286**, 561 (1980).

[14] Woodland, M. P.; Dalton, H. *J. Biol. Chem.*, **259**, 53 (1984).

[15] (a) Andersson, K. K.; Froland, W. A.; Lee, S.-K.; Lipscomb, J. D. *New J. Chem.*, **15**, 411 (1991). (b) Jiang, Y.; Wilkins, P. C.; Dalton, H. *Biochim. Biophys. Acta*, **1163**, 105 (1993).

[16] (a) Rosenzweig, A. C.; Frederick, C. A.; Lippard, S. J. *J. Mol. Biol.*, **227**, 583 (1992). (b) Rosenzweig, A. C.; Frederick, C. A.; Lippard, S. J.; Nordlung, P. *Nature*, **366**, 537 (1993).

[17] Whittington, D. A.; Lippard, S. J., *J. Am. Chem. Soc.*, **123**, 827 (2001).

[18] (a) Rosenzweig, A. C.; Brandstetter, H.; Whittington, D. A.; Nordlund, P.; Lippard, S. J.; Frederick, C. A. PROTEINS: *Struct., Funct., Genet.*, **29**, 141 (1997). (b) Whittington, D. A.; Rosenzweig, A. C.; Frederick, C. A.; Lippard, S. J., *Biochemistry*, **40**, 3476 (2001).

[19] (a) Lee, S.-K.; Nesheim, J. C.; Lipscomb, J. D. *J. Biol. Chem.*, **268**, 21569 (1993). (b) Lee, S.-K.; Fox, B. G.; Froland, W. A.; Lipscomb, J. D.; Münck, E. *J. Am. Chem. Soc.*, **115**, 6450 (1993). (c) Liu, K. E.; Wang, D.; Huynh, B. H.; Edmondson, D. E.; Salifoglou, A.; Lippard, S. J. *J. Am. Chem. Soc.*, **116**, 7465 (1994).

[20] (a) Barton, D. H.; Beviere, S. D.; Chavasiri, W.; Csuhai, E.; Doller, D.; Liu, W.-G. *J. Am. Chem. Soc.*, **114**, 2147 (1992). (b) Feig, A. L.; Lippard, S. J. *Chem. Rev.*, **94**, 759 (1994). (c) Fox, B. G.; Froland, W. A.; Dege, J. E.; Lipscomb, J. D. *J. Biol. Chem.*, **264**, 10023 (1989). (d) Priestley, N. D.; Floss, H. G.; Froland, W. A.; Lipscomb, J. D.; Williams, P. G.; Morimoto, H. *J. Am. Chem. Soc.*, **114**, 7561 (1992). (e) Nesheim, J. C.; Lee, S.-K.; Lipscomb, J. D. *Biochemistry*, **35**, 10240 (1996). (f) Choi, S.-Y.; Eaton, P. E.; Kopp, D. A.; Lippard, S. J.; Newcomb, M.; Shen, R. *J. Am. Chem. Soc.*, **121**, 12198 (1999).

[21] (a) Siegbahn, P. E. M. *Inorg. Chem.*, **38**, 2880 (1999). (b) Basch, H.; Mogi, K.; Musaev, D. G.; Morokuma, K. *J. Am. Chem. Soc.*, **121**, 7249 (1999). (c) Dunietz, B. D.; Beachy, M. D.; Cao, Y.; Whittington, D. A.; Lippard, S. J.; Friesner, R. A. *J. Am. Chem. Soc.*, **122**, 2828 (2000).

[22] (a) Lee, S.-K.; Lipscomb, J. D. *Biochemistry*, **38**, 4423 (1999). (b) MacMurdo, V. L.; Zheng, H.; Que, L., Jr. *Inorg. Chem.*, **39**, 2254 (2000).

[23] Itoh, M.; Nakazawa, J.; Maeda, K.; Kano, K.; Mizutani, T.; Kodera, M. *Inorg. Chem.*, **44**, 691-702 (2005).

[24] Baker, W.; Buggle, K. M.; McOmie, J. F. W.; Watkins, D. A. M. *J. Chem. Soc.*, 3594 (1958).

[25] Kodera, M.; Itoh, M.; Kano, K.; Funabiki, T.; Reglier, M.; *Angew. Chem. Int. Ed.*, **44**, 7104 (2005).

[26] (a) Whittlesey, B. R.; Pang, Z.; Holwerda, R. A. *Inorg. Chim. Acta*, **284**, 124 (1999). (b) Hazell, A.; Jensen, K. B.; McKenzie, C. J.; Toftlund H. *Inorg. Chem.*, **33**, 3127 (1994). (c) Norman, R. E.; Yan, S.; Que, L. Jr.; Backes, G.; Ling, J.; Sanders-Loehr, J.; Zhang, J. H.; O'Connor, C. J. *J. Am. Chem. Soc.*, **112**, 1554 (1990). (d) Norman, R. E.; Holz, R. C.; Menage S.; O'Connor, C. J.; Zhang, J. H., Que, L. Jr. *Inorg. Chem.*, **29**, 4629 (1990).

[27] (a) Dong, Y.; Fujii, H.; Hendrich, M. P.; Leising, R. A.; Pan, G.; Randall, C. R.; Wilkinson, E. C.; Zang, Y.; Que, L. Jr.; Fox, B. G.; Kauffman, K.; Münck, E. *J. Am. Chem. Soc.*, **117**, 2778 (1995). (b) Ryu, J. Y.; Kim, J.; Costas, M.; Chen, K.; Nam, W.; Que, L. Jr. *Chem Commun.*, 1288 (2002). (c) Chen, K.; Costas, M.; Que, L. Jr., *J. Chem. Soc., Dalton Trans.*, 672 (2002). (d) Costas, M.; Que, L. Jr., *Angew. Chem. Int. Ed.*, **41**, 2179 (2002). (e) Chen, K.; Costas, M.; Kim, J.; Tipton, A. K.; Que, L. Jr., *J. Am. Chem. Soc.*, **124**, 3026 (2002). (f) Costas, M.; Tipton, A. K.; Chen, K.; Jo, D.-H.; Que, L. Jr., *J. Am. Chem. Soc.*, **123**, 6722 (2001).

[28] White, M. C.; Doyle, A. G.; Jacobsen, E. N. *J. Am. Chem. Soc.*, **123**, 7194 (2001).

[29] (a) Miyaura, N.; Kochi, J. K., *J. Am. Chem. Soc.*, **105**, 2368 (1983). (b) Che, C.-M.; Li, C.-K.; Tang, W.-T.; Yu, W.-Y., *J. Chem. Soc., Dalton Trans.*, 3153 (1992). (c) Kobayashi, T; Arai, T; Sakuragi H; Tokumaru K; Utsunimiya, C. *Bull. Chem. Soc. Jpn.*, **54**, 1658 (1981). (d) Freeman, F.; Kappos, J. C. *J. Org. Chem.*, **54** 2730 (1989).

[30] Dong, Y.; Zang, Y.; Shu, L.; Wilkinson, E. C.; Que, L., Jr. *J. Am. Chem. Soc.*, **119**, 12683 (1997).

Failure Analysis of Cu/Low-k Interconnects Using Electron Beam Absorbed Current Images

Y. Mizushima, T. Kimura, M. Sato† and T. Nakamura

ADVANCED MATERIALS Lab., DEVICE & MATERIALS LABORATORIES, FUJITSU LABORATORIES Ltd., †PROCESS DEVELOPMENT Dept., DEVICE DEVELOPMENT Div., FUJITSU Ltd.

In the 65 nm node interconnects process development, Test Elements Group (TEG) patterns, which have one million or more vias with 100 nm half pitch and an electric resistance of the order of 1E+7 Ω or more, are used. Along with the development of TEG patterns, for failure analysis, a technique which can specify a high-resistance defect, with a spatial resolution of 0.1 μm or more and little damage to low-k film, is needed. The spatial resolution of optical failure analysis methods, like IR-OBIRCH, is limited by the wavelength of IR-laser (limited to 1 μm). On the other hand, the electron beam voltage contrast method has some disadvantages: for example, image contrast depends on the observation conditions, such as magnification.

Absorbed current image observations were performed on a high resistance defect in the Cu/Low-k interconnects by using a scanning electron microscope equipped with a high performance current amplifier and a probe manipulation system. By adopting the most suitable observation conditions found by simulations and experiments, we could successfully specify a high resistance (R=3E+9 Ω) defect in eight million via chains (L/S=1:3.5) covered with a dielectric film of 100 nm thickness.

Keywords: absorbed current, Cu interconnects, low-k film, high resistance, defect.

Introduction

In the course of a development of a LSI device, failure analysis methods are generally used to improve the performance and manufacturing yield of the devices. These methods consist of a specification of a defect which cannot be expected to arise in the semiconductor manufacturing process, and an analysis of the cause of the defect. These techniques are regarded as significantly important in the development of the process.

However, along with the recent accelerated miniaturization and integration of the devices, the TEG for the interconnects process are also miniaturized and contain increasing number of patterns such as vias and lines. Now, it is very difficult to specify failure sites in a large number of these patterns. The application of optical failure analysis methods to the fine patterns, for example, IR-OBIRCH (Infrared-optical beam induced resistance change), has a limitation in specifying defects, because the spatial resolution for these methods is approximately 1 μm. Without special techniques, these methods cannot analyze the defects on the fine patterns with a line width far below 1 μm.

In terms of a electrical resistivity of a defect, IR-OBIRCH is rather effective for specifying failure sites on a sample that has a relatively low resistance and the electron beam voltage contrast image is suitable for finding open sites. In recent years, the demand for specifying a defect showing high resistivity, i.e., between a low and open, has increased.

It has been reported that the absorbed current method, which observes an absorbed current generated by the irradiation of an electron beam, is very effective for specifying the differences in the thickness of residual films at the bottom of via-holes and actually can be utilized for process monitoring [1].

A two dimensional imaging of the absorbed current intensity obtained by this method was applied successfully to failure analysis [2]. Thus, recently, this innovative method has drawn attention in the specification of failure sites.

We performed absorbed current image observations of a high-resistance defect in the 65 nm node TEG patterns having one million or more vias with 100 nm half pitch for fine Cu/Low-k interconnects. In this observation, we could successfully specify a high-resistance defect sites by optimizing the measurement conditions. Our experimental results, together with our instrument, are reported in this paper.

Overview of the Instrument

Figure 1 shows the configuration of our instrument. We used a JEOL JSM-7000F FE-SEM for detecting an absorbed current. The specimen chamber and stage for the SEM are maintained at ground potential and the specimen holder can be either electrically isolated from the chamber or maintained at the same ground potential. Tungsten probes, which are driven by a piezoelectric device, are placed in the specimen chamber (up to four probes can be connected). It is possible to electrically contact with the arbitrary points on the specimen while observing a SEM image. The absorbed current detected by the probe is extracted to the outside of the specimen chamber through a co-axial cable and feedthroughs. Then, this current is subjected to a current-voltage conversion by a preamplifier directly attached on

50 Fuchigami Akiruno-shi, Tokyo 197-0833, Japan
E-mail : kimura.takahiro@jp.fujitsu.com

the specimen chamber (gain: 1GV/A, frequency band: 7 kHz), then amplified to one hundred times, and imaged by synchronizing to the electron-beam scanning signal from the SEM.

Optimizing the Observation Conditions

Upper dielectric film

A TEG pattern of an interconnect usually has a dielectric film with a thickness of several microns as the most upper protection layer. If we increase the accelerating voltage of SEM, it enables us to observe an interconnect beneath a thick dielectric film.

However, for a sample which is considered to be relatively weak for electron damage, such as a low-k film, it is desirable to be observed with an accelerating voltage as low as possible.

In such a case, it may be possible to observe the interconnect after etching off the entire dielectric film. However, if a defect is present on the top surface of the pattern, there is a possibility that a true (actual) defect can not be distinguished from the damage on the surface caused by the etching. Thus, it is desirable to obtain an absorbed current image under a condition where a dielectric film as thin as possible remains on the pattern. The presence of the dielectric film also has an advantage for protecting the pattern from the ion-beam irradiation damage, which arises from cross-sectional milling by FIB after the specification of failure sites.

Primary electron energy and spatial resolution

To find the optimum observation condition for detecting the defect in the interconnect with its surface being protected by the dielectric film, the absorbed-current generation region was estimated. Since this region is considered to be confined within the electron range, we carried out a Monte Carlo calculation on the electron range about the several primary electron energies [3].

The result of the calculation is shown in **Fig. 2**. It is found that when the primary electron energy is 2 keV, electrons do not reach the Cu interconnect beneath the dielectric film with a thickness of 100 nm, resulting in few generation of the absorbed current in the Cu interconnect. When the primary electron energy is 4 keV, the absorbed current is generated on the Cu interconnect. However, the absorbed current generation volume in the interconnect is so large that the spatial resolution is too poor. Consequently, we selected a primary electron energy around 3 keV for the optimum observation condition, with which a spatial resolution of 200 nm sufficient for the present measurement can be obtained.

Probing geometry of the absorbed current and its signal intensity

Sample

The sample used for the present measurement was a Cu via chain with a line width of 3 μm. Prior to the absorbed current measurement, a high-temperature overload testing (200°C, 540 h) was applied and the resistance increased from the initial value of $R=2 \times 10^5\ \Omega$ to $R=1.8 \times 10^7\ \Omega$. Then the dielectric film on the via chain was thinned by dry etching, down to a thickness of 100 nm. To confirm an appearance of high-resistance defect that is localized on the sample, IR-OBIRCH measurement using an IR-laser with an excitation wavelength of 1.3 μm was performed. **Figure 3** shows the result of measurement. An OBIRCH signal, which shows the high-resistance defect site (indicated by an arrow in Fig. 3), is superimposed on an optical microscope image.

Measurement result

Absorbed current images were obtained from the same sample used for the measurement shown in Fig. 3 and the result of observation is presented in **Fig. 4**. An accelerating voltage of 3 kV and a probe current of 400 pA were used for taking the images of Fig. 4. Absorbed current images clearly showing the via chain were not obtained at the accelerating voltage less than 3 kV.

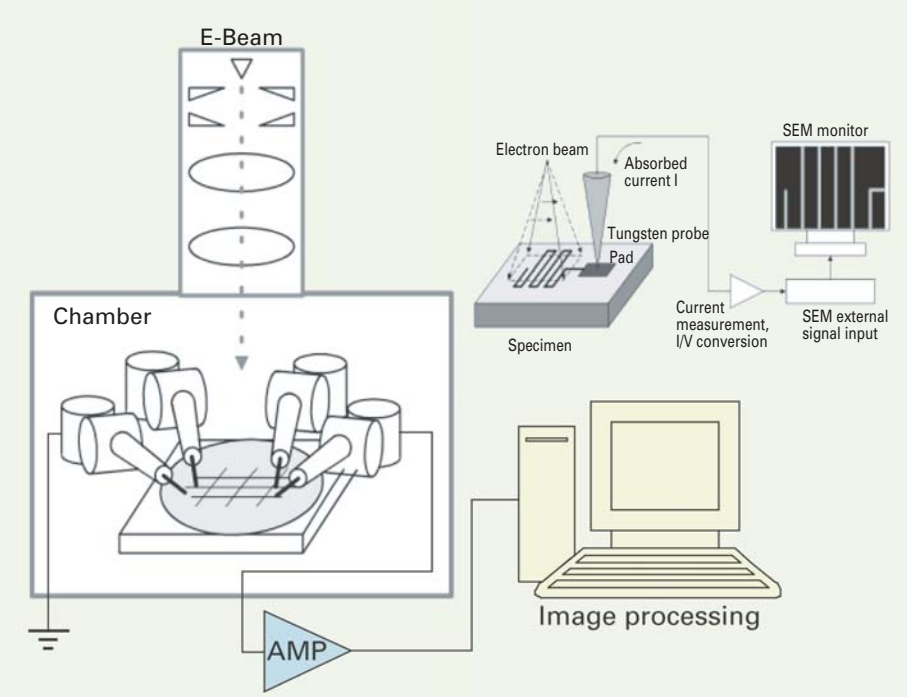

Fig. 1 Configuration of the instrument.

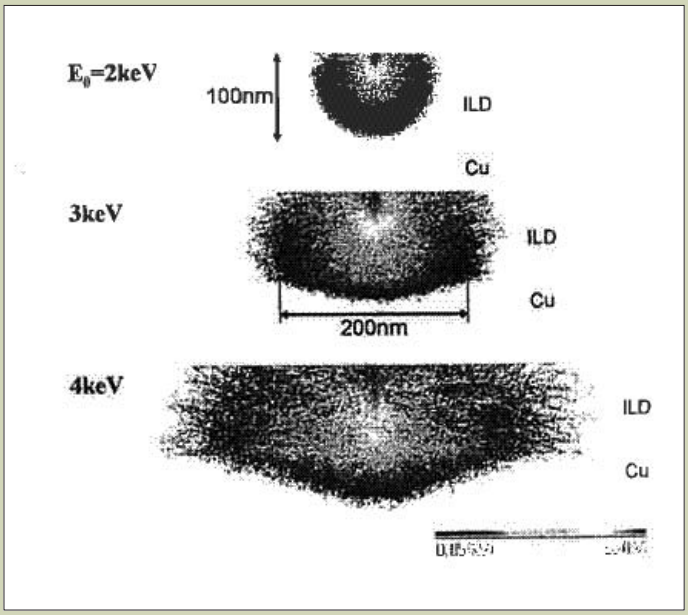

Fig. 2 Monte Carlo calculation on the electron range by the use of the primary electron energy.

Figure 4A is an absorbed current image that was obtained under a condition where one of the pad on the via chain was connected to a current amplifier, another pad to the ground, and the sample stage was electrically isolated. A high-resistance defect is considered to exist on the border of bright and dark contrast of the image (indicated by an arrow). This defect site coincided with that detected by IR-OBIRCH in Fig. 3. The graph below Fig. 4A plots the variations of absorbed current when an electron beam was scanned across the defect site (from left to right on the bright and dark contrast). The graph reveals that the difference between the bright and dark contrast corresponds to a 100 pA change of the absorbed current.

Figure 4B shows an absorbed current image and a plotted graph, which were obtained under the same condition as Fig. 4A except that the sample stage was connected to the ground. Due to the change of this condition, the variations of absorbed current at the defect site were found to be 40 pA (in the graph below the image). This implies that the change of the current is drastically reduced, less than one-half the change when the sample stage was electrically isolated.

A SEM image of a metallic interconnect beneath a dielectric film is known to be influenced by the surface charge distribution which is affected by the capacitively coupled potentials of the interconnect [4]. A similar phenomenon is considered to occur in the change of the absorbed current when the sample stage is electrically isolated.

The electron yield of the dielectric film covering the via chain is considered to be negative according to the used accelerating voltage of the electron beam and the composition of the dielectric film (Si, C) [5]. Therefore the surface of the covering film is considered to be negatively charged during the electron-beam

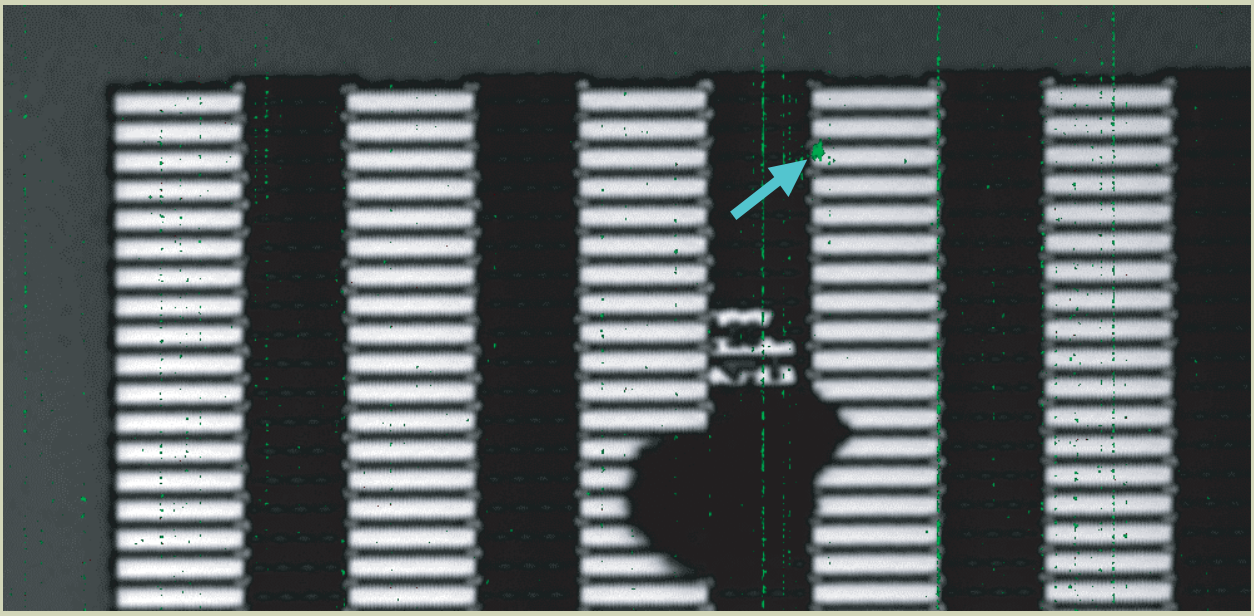

Fig. 3 Detection of a high-resistance defect site by IR-OBIRCH.

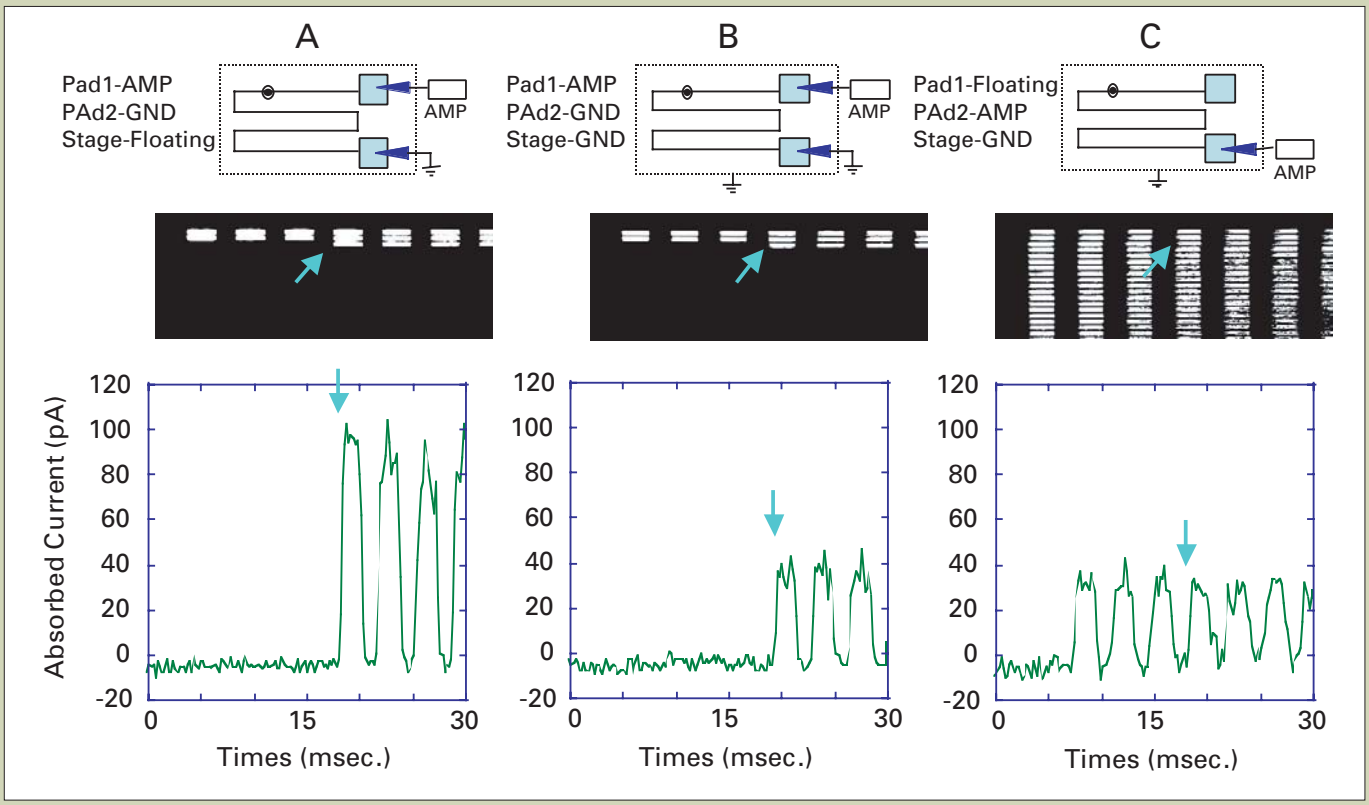

Fig. 4 Probe positions and absorbed current images.

irradiation. An electric field generated by this negatively charged potential acts as a retarding electric field for the secondary electrons emitted from the interconnect, and contributes to the increase in the absorbed current. However, if the backside surface of the sample is connected to the ground potential, the potential on the surface of the dielectric film passes through the sample surface to the ground and its potential is reduced, and as a result, the retarding electric field is weakened. This phenomenon could be used to explain the absorbed current generated from the interconnect.

Figure 4C is an absorbed current image that was obtained under a condition where the distant pad from the defect site was connected to a current amplifier, the pad near the defect was electrically floated, and the sample stage was connected to the ground. In Fig. 4C, the contrast border of the defect site clearly shown in Fig. 4A, almost disappeared. This is considered to be caused by the following phenomena: A) a voltage was generated between the high-resistance defect site and the electrically floated pad by the charges that was present on the via chain, B) an electric current generated by this voltage flowed to the amplifier with a low impedance, through the high-resistance defect, C) the flowing current was accidentally almost the same value as that of the absorbed current on the amplifier side. Thus, no contrast was formed on the defect site. It is noted that the voltage generated from a flowing absorbed current of 30 pA was –5.4 mV because the resistance on the localized defect was 1.8×10^{-7} Ω.

From the present measurement described above, it was found that the following two conditions are effective for detecting a high-resistance defect beneath a dielectric film with a better contrast.

1) (If a dielectric film is negatively charged,) Electrically float the backside surface of the sample from the ground, in order to easily make it charged up. This increase the absorbed current in the interconnect by a generated retarding electric field.
2) Connect the pad, which is distant from the high-resistance defect, to the ground, so that a reverse electromotive force is not generated.

Examples of Analysis

Based on the above observation conditions, we applied the absorbed current method to the specification of the defect in 65 nm Cu/Low-k interconnects. The examples of our analysis are reported below.

Eight million via chains (normal resistance: R=3×10^7 Ω) of a line width 0.1 µm (L/S=1:3.5)

The sample via chain contained a high-resistance defect ($R=3 \times 10^{11}$ Ω). The upper layer of the dielectric film on the via chains was thinned down to 50 nm by dry etching, and was subjected to SEM observation at an accelerating voltage of 3 kV and a probe current of 400 pA. **Figure 5** shows the obtained SEM image and absorbed current image.

The SEM image, which is influenced by the surface potential, is known to change its quality depending on the observation conditions (scan speed, magnification, etc.) [5]. In the present analysis, the voltage contrast of the defect site was obtained at a low magnification; however, when the magnification was increased in order to determine the precise defect site, this contrast disappeared. On the other hand, the absorbed current image showed no contrast change depending on the magnification, enabling the precise determination of the defect site.

The present instrument can make a precise marking, by way of an electron-beam assisted carbon-gas deposition, even on a 0.1 µm width interconnect (**Fig. 6**). Using this marking as a reference, it is possible to perform high-precision FIB milling.

Figure 7 shows the result of analysis of the via chains. The specified defect site in the via chains was subjected to cross-sectional FIB milling and STEM observation. The STEM image revealed an open failure where a via portion was not opened.

The absorbed current method was also applied to a high-resistance defect ($R=1.5 \times 10^{11}$ Ω) in the TEG patterns in the same via chains, on which the upper dielectric protective film was thick (660 nm). **Figure 8** shows the result of observation. An image could not be obtained at an accelerating voltage of 3 kV. When the voltage was increased to 10 kV

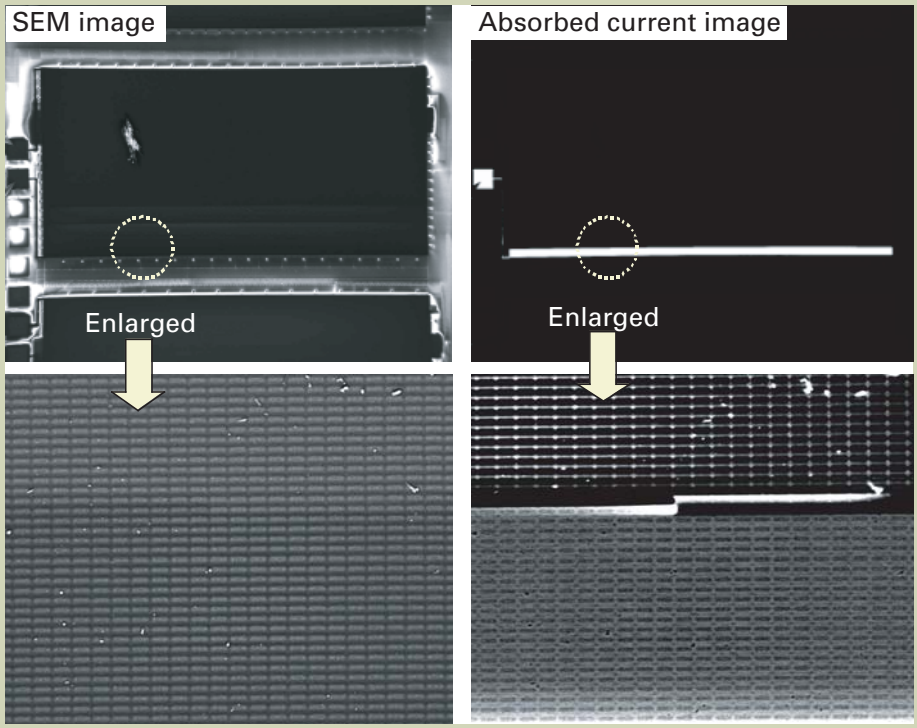

Fig.5 Example of analysis: W=0.1 µm (L/S=1:3.5, R=3×10^{11}Ω)

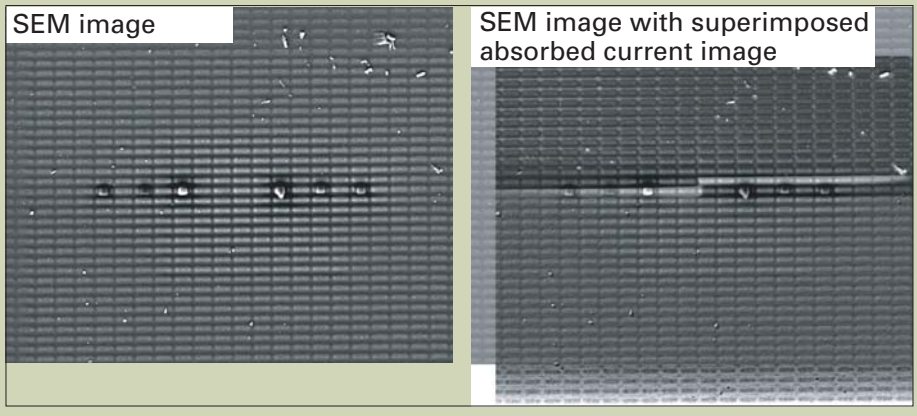

Fig. 6 Example of analysis: W=0.1 µm (L/S=1:3.5, R=3×10^{11}Ω)

(probe current: 180 pA), an absorbed current image was obtained, but the spatial resolution of the image was so poor that enable us to determine only a rough location of the defect. This defect site could be managed to be prepared for a STEM observation by confirming a SEM image while milling it in FIB-SEM.

Eight thousand via chains (normal resistance: R=5×10^4 Ω) of a line width 3 μm

The sample via chain contained a high-resistance defect (R=9.6 × 10^{11} Ω). The upper layer of the dielectric film on the via chains was thinned down to 350 nm by dry etching and observed at an accelerating voltage of 5 kV and a probe current of 40 pA. **Figure 9** shows obtained SEM images and absorbed current images.

We mutually exchanged the position of the two probe contacted the pads, one was connected to the current amplifier and the other to the ground, and observed the same sample. In this observation, although the dark and bright contrast were reversed, but the position of the contrast border of the absorbed current image was the same. This implies that there is only one failure site in the via chain.

Normally, the absorbed current image shows a dark contrast where the site ahead of the high-resistance defect. Thus, if multiple failure sites are present in the same chain, when the connection of the two pads to the current amplifier and to the ground is exchanged, two failure sites should be detected.

Utilizing this fact enables one to not only specify a defect site by an absorbed current image, but also estimate the frequency of failure from the specified defect site (distance from the pad).

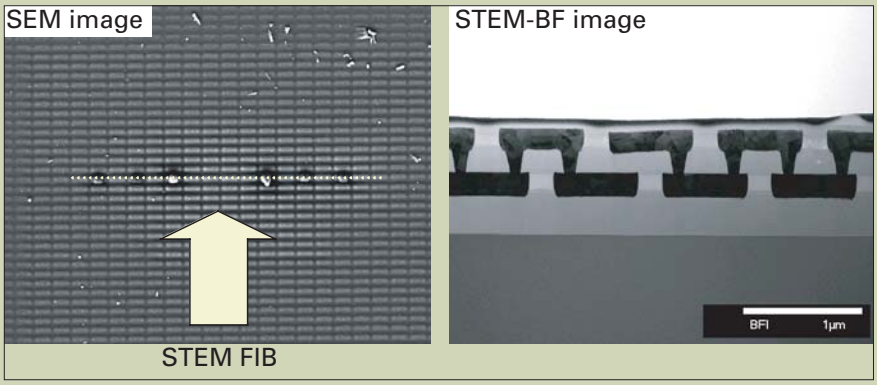

Fig. 7 Example of analysis: W=0.1 μm (L/S=1:3.5, R=3×10^{11}Ω)

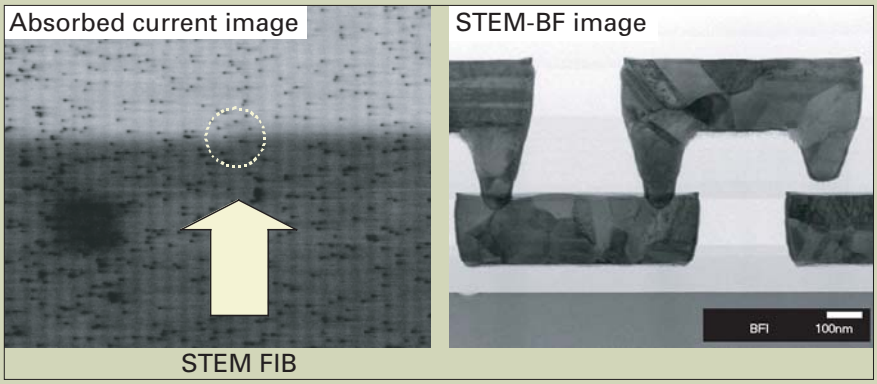

Fig. 8 Example of analysis: W=0.1 μm (L/S=1:3.5, R=1.5×10^{11}Ω)
Accelerating voltage: 10 kV, Upper dielectric film: 660 nm thick

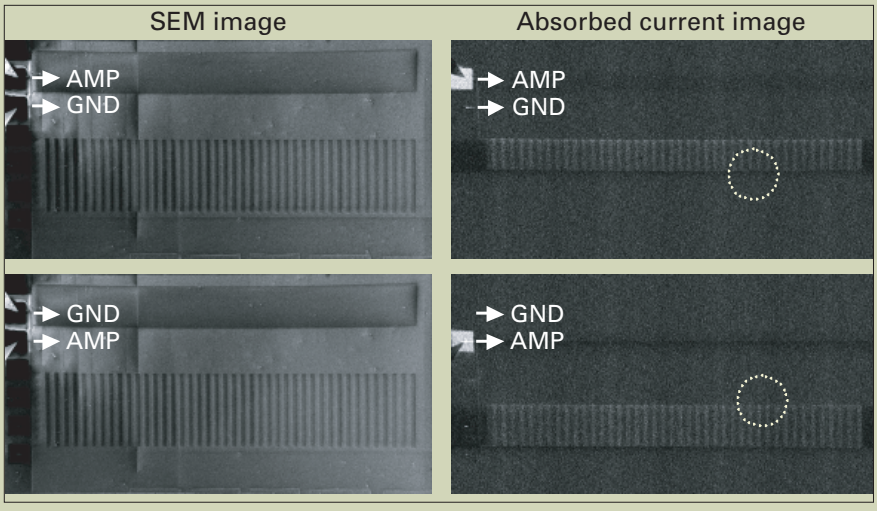

Fig. 9 Example of analysis: W=0.3 μm, L=20 μm (R=3×10^{11}Ω)

Summary

We confirmed that the absorbed current image observation combined with a probing capability is effective to specify failure sites of a high-resistance defect (R=3 × 10^9 Ω) on the 65 nm node Cu/Low-k interconnects in one million or more via chains (L/S=1:3.5) with a line width of 0.1 μm. By introducing this method, it becomes possible to analyze a high-resistance defect in a narrow-width via chain. Since this method opens the possibility of a correct analysis of a defect which is previously difficult to specify, it will contribute to the development of future high-end semiconductor processes in which integration and miniaturization of devices are increasingly progressing.

In the future, we will examine the applications of this absorbed current method for the specification of a leakage failure.

Acknowledgement

We are grateful to Mr. Takeshi Nokuo of SM Group, Metrology Inspection Division, JEOL Ltd., for his support for our experiments.

References

[1] S. Ota, T. Ishimoto and Y. Tanaka, *JEOL news* **Vol. 37E**, No. 1, 54-58 (2002).
[2] K. Mizukoshi et al., Identification of Failure Sites on LSI Interconnects by Electron Beam Absorbed Current Analysis, Proc. LSI Testing Symposium 2003, 213-218.
[3] K. Kanda, "Monte Carlo Simulation (Bulk with thin films)", V. 2.38, 1997-2004.
[4] H. Seiler, *J. Appl. Phys.*, **54**, R1-R18 (1983).
[5] K. Ura and S. Aoyagi, *J. Electron Microsco.*, **49**, 163-172 (2000).

Corresponding author

Organization: ADVANCED MATERIALS Lab., DEVICE & MATERIALS LABORATORIES, FUJITSU LABORATORIES Ltd.

New Development of DOSY-NMR – Application to Structure Elucidation of Unstable Intermediates–

Masamichi Nakakoshi

Chemical Analysis Center, Yokohama National University

Introduction

Diffusion-Ordered Spectroscopy (DOSY) methods [1, 2] are based on pulse-field gradient spin-echo NMR experiments.

The DOSY pulse-sequences consist of various methods: Pulse Field Gradient Longitudinal Eddy current Delay (PFGLED) [3], Bipolar Pulse Pairs STimulated spin Echo (BPPSTE) [4], Gradient Compensated STimulated spin Echo (GCSTE) [5], Bipolar Pulse Pair-Longitudinal Eddy current Delay (BPPLED) [6] and GCSTESL (GCSTE with Spin-Lock pulse) [7]. The BPPLED method has been used to cancel the adverse effects of eddy currents using two gradient pulses with identical areas but different polarities. Its effects have been reported by Wu, *et al* [6] and this method has most been used to the DOSY pulse-sequences. In addition, the 3D-DOSY method which refines the 2D-DOSY method have been reported, including DOSY-COSY [8], DOSY-HMQC [9], DOSY-HMBC and DOSY-NOESY [10]. However, there has been almost no report on the applications of the 3D-DOSY method.

As application examples of the DOSY method, several reports have been presented. Sobolev, *et al* [11] applied DOSY in NMR to examine tomato juice, and Groves [12] analyzed oligosaccharides by this method. However, no report has been published on the application of this method to organic synthesis. The great advantage of the DOSY NMR measurement is thought to be the structural elucidation of each component in mixed samples without isolating the components. In particular, this method is effective in the analysis of unstable intermediates in a reaction mixture. This measurement offers a high possibility of direct structural observation of an unstable compound, by which synthetic reaction of the compound is made in a sample tube and its reaction-mixture solution is measured. In order to clarify the reaction mechanism, the DOSY measurement was applied to the unstable intermediates. In this paper, we report on application examples of DOSY NMR to structural elucidation of unstable intermediates in the radical reactions of triethylborane (Et_3B) and oxime ethers. The success of the elucidation of the structure of the unstable intermediate by ^{1}H- and 3D-DOSY methods, for the first time, is clearly demonstrated.

79-5, Tokiwadai, Hodogaya-ku, Yokohama, Japan
E mail : m-nakako@ynu.ac.jp

Sample Preparation and Measurement Method

For preparing the sample for measurement, 100 µL of a 0.013 M solution of Et_3B in CH_2Cl_2 was added to 100 µL of a 0.013 M solution of oxime ether in a 3-mm NMR sample tube, and then, this tube was encapsulated under a reduced pressure.

^{1}H- and 3D-DOSY spectra were measured on a JEOL JNM-ECA500 instrument equipped in a TH5FG probe head with an actively shielded Z-gradient coil. ^{1}H–DOSY used the BPPSTE-LED (Bipolar Pulse Pairs Stimulated Echo-Longitudinal Eddy current Delay) pulse sequence. The gradient amplitude (g) was changed from 1 to 30 G cm^{-1} in 32 steps. Eddy-current delay was set to 50 ms.

The BPP-STE-COSY, GC-STE-HMQC and -HMBC were measured for 3D-DOSY. The gradient amplitude (g) was changed from 1 to 30 G cm^{-1} in 8 steps. The SPLMOD (SPLine MODel) algorithm was used for DOSY processing.

Results and Discussion

In this paper, we report on the analysis results with R=H, Bn=Ch_2Ph, and oxime ether **1b** with R=$COOCH_3$, Bn=Ch_2Ph.

On the basis of our related work with radical reaction, a reaction pathway for triethylborane (Et_3B) and oxime ethers **1a**, **b** is proposed in Scheme 1 [13].

The first step is the generation of an ethyl radical by the reaction of Et_3B with oxygen. The ethyl radical formed can extract an iodine atom from the radical precursor to produce an alkyl radical. The iodine transfer is fast and efficient when the alkyl radical is more stable than the ethyl radical. The alkyl radical is

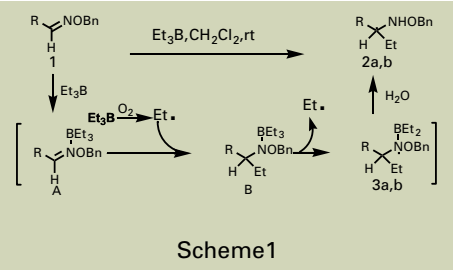

Scheme1

added to triethylborane-activated oxime ether **A** to form aminyl radical **B** as the intermediate, which is then trapped with triethylborane as a radical terminator to give the complexes **3a**, **b** and the ethyl radical. The alkyl radical formed again enters into the radical chain process. The alkylated product **2a**, **b** is obtained as a result of the hydrolysis of **3a**, **b**.

After the reaction of **1a** with Et_3B, the reaction mixture was concentrated at reduced pressure. However, intermediate **B**, **3a** could not be found in the ^{1}H-NMR spectrum of the residue, therefore, the intermediate was confirmed to be unstable. In order to find borane complexes **A**, **B** and **3**, an attempt was made to isolate signals from the unstable intermediate by the following way: The mixture was reacted in the NMR sample tube, and then the reaction mixture solution was subjected to direct DOSY measurement without purification procedures such as extraction. Although **A** and **B** could not be found, chemical compounds which are estimated to be **3a**, **b** were observed. We attempted to clarify their structures.

Reaction of 1a and Et_3B

In the DOSY data obtained by the BPP-STE-LED method (**Fig. 1**), the spectra of **2a** and **3a** were separated extremely well owing to their different diffusion coefficients. Slice **C** of **Fig. 2** is suggested as the intermediate **3a**.

The chemical structure of the intermediate **3a** can be deduced from the 3D-DOSY results.

The DOSY-COSY slice spectrum (**Fig. 4**) shows the cross peaks between 1”-H to 2”-H and 1-H to 2-H. In the DOSY-HMQC slice spectrum (**Fig. 5**), cross peaks were observed between 2-H and 2-C, 3-H and 3-C and 1-H and 1-C. In the DOSY-HMBC slice spectrum

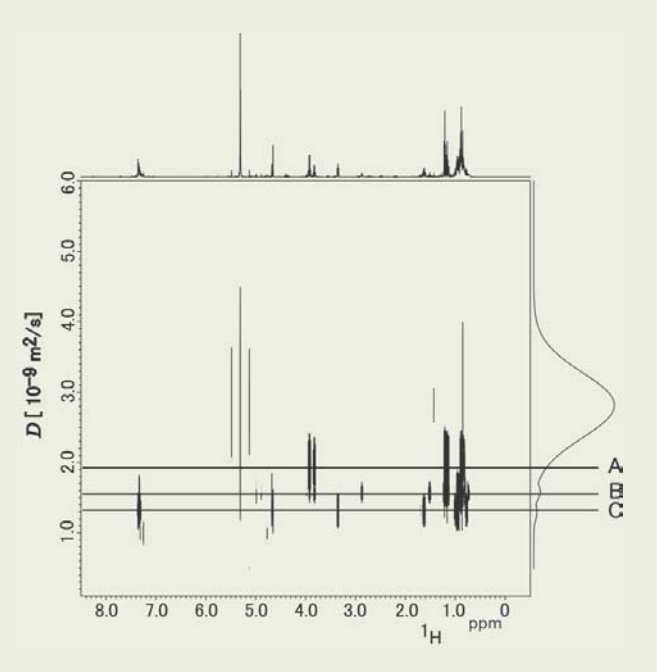

Fig. 1 ^{1}H-DOSY spectrum of reaction mixture.

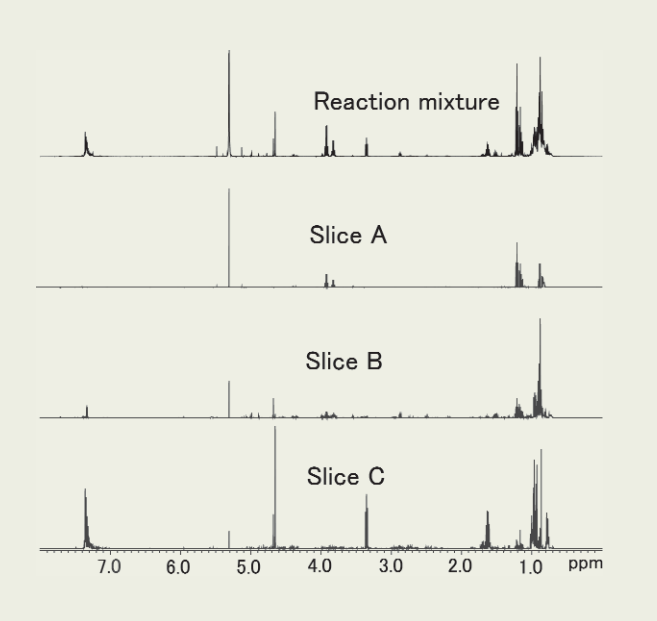

Fig. 2 ^{1}H spectra of reaction mixture and each slice.
Slice A : Triethylborane (Et_3B)
Slice B : Derivative 2a
Slice C : Intermediate 3a

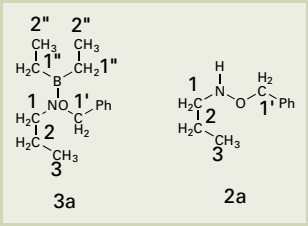

Fig. 3 Structure of 3a and 2a.

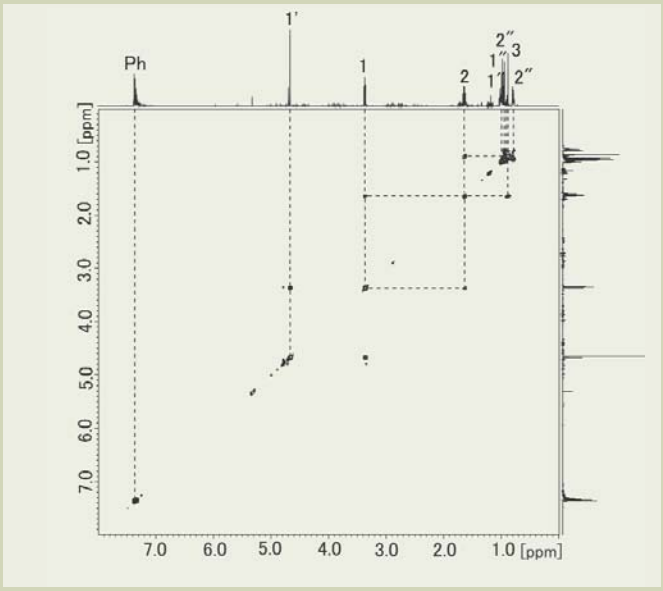

Fig. 4 DOSY-COSY slice spectrum of 3a in reaction mixture.

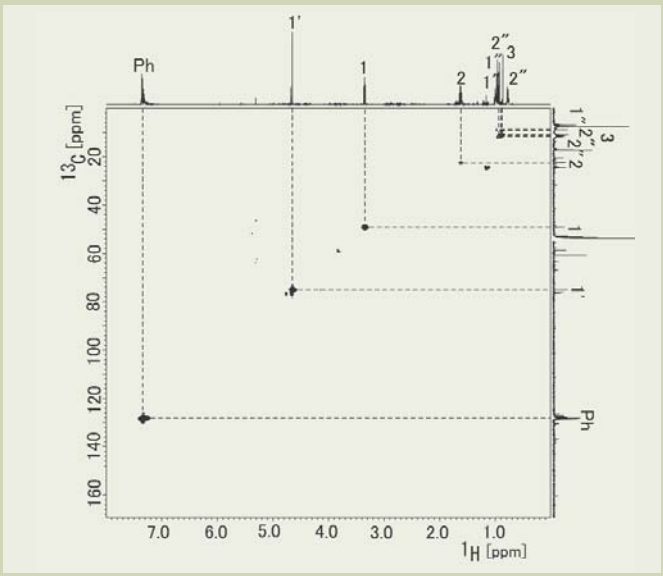

Fig. 5 DOSY-HMQC slice spectrum of 3a in reaction mixture.

(**Fig. 6**), cross peaks were observed between 2-H and 1-C and between 2-H and 3-C. Therefore, the intermediate **3a** would be an ethyl adduct, formed by addition of an ethyl radical to **1a**. **Table 1** shows the proposed assignment of 1H and ^{13}C of **2a** and **3a**, and **Fig. 3** presents the proposed structure of **2a** and **3a**.

The resonances of the 1-H and 2-H in the proposed intermediate **3a** are shifted downfield by 0.47 and 0.01 ppm, respectively, as compared with those of **2a**. These downfield shifts, as compared to the bonding borane group, suggest the formation of the borane complex **2a**.

In order to confirm the structure of the proposed intermediate **3a**, the ^{11}B NMR spectrum of the reaction mixture was analyzed. In the ^{11}B NMR spectrum of **2a**, the signal at 86.6 ppm due to triethylborane disappeared and instead, a new signal at 53.9 ppm was observed. In addition, ^{1}H–^{15}N HMBC shows, as expected, cross peaks between the ^{15}N signal at 202 ppm and the methylene signal (1"-H) at 0.78 ppm. Therefore, the proposed structure of **3a** in **Fig. 3** was confirmed.

Reaction of 1b and Et_3B

The signals of **2b** and **3b** separated clearly in the resulting DOSY (**Fig. 7**). Slice **C** of **Fig. 8** suggests **3b** as the intermediate, and slice B was correlated to the structure of **2b** (**Fig. 9**).

DOSY-COSY (**Fig. 10**) enabled the assignment of the ethyl groups connecting 2"-H to 1"-H. The chemical shifts of these two ethyl groups were different, and were differentiated by DOSY-COSY slice data. Cross peaks between 1-H and 2-H were also observed. In the DOSY-HMQC slice spectrum for **3b** (**Fig. 11**), all proton peaks have cross peaks to carbon and to each other: 1-H and 1-C, 2-H and 2-C and 1-H, 2'-H and 2-C, and 1"-H and 2"-C. Furthermore, in the DOSY-HMBC slice spectrum of **3b** (**Fig. 12**), some cross peaks were observed between 2-H and 3-C, 1"-H and

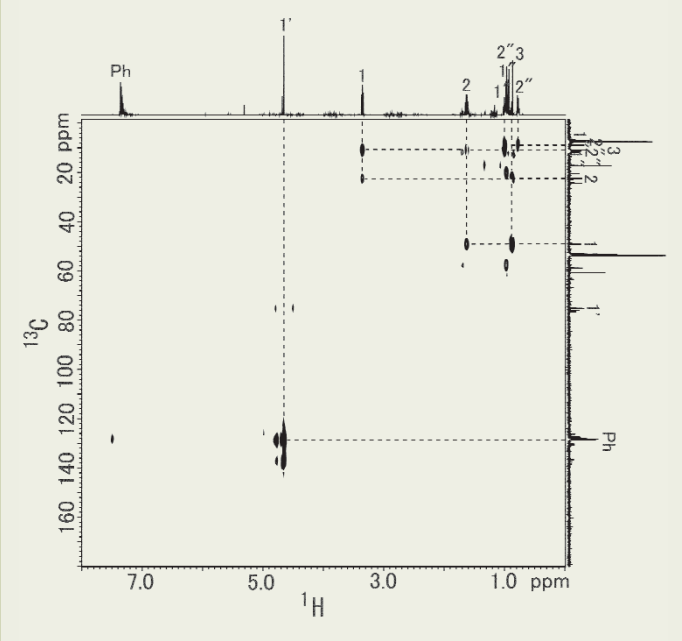

Fig. 6 DOSY-HMBC slice spectrum of 3a in reaction mixture.

Table 1 ^{1}H and ^{13}C NMR Data of 2a and 3a

^{1}H	3a (ppm)	2a (ppm)	^{13}C	3a (ppm)
1-H	3.37(1H,t,J=7)	2.90(1H,t,J=7.4)	1-C	49.1
2-H	1.64(2H,m)	1.54(2H,m)	2-C	22.4
3-H	0.89(3H,br t,J=7)	0.92(3H,t,J=7.3),	3-C	10.9
1'-H	4.67(2Hs)	4.70(2H,s)	1'-C	75.1
1''-H	0.78(2H,br q,J=8)			8.0(br)
	0.86(2H,m)			11.5(br)
2'-H	0.93(3H,m)		2''-C	8.9
	1.04(3H,br t,J=7)			

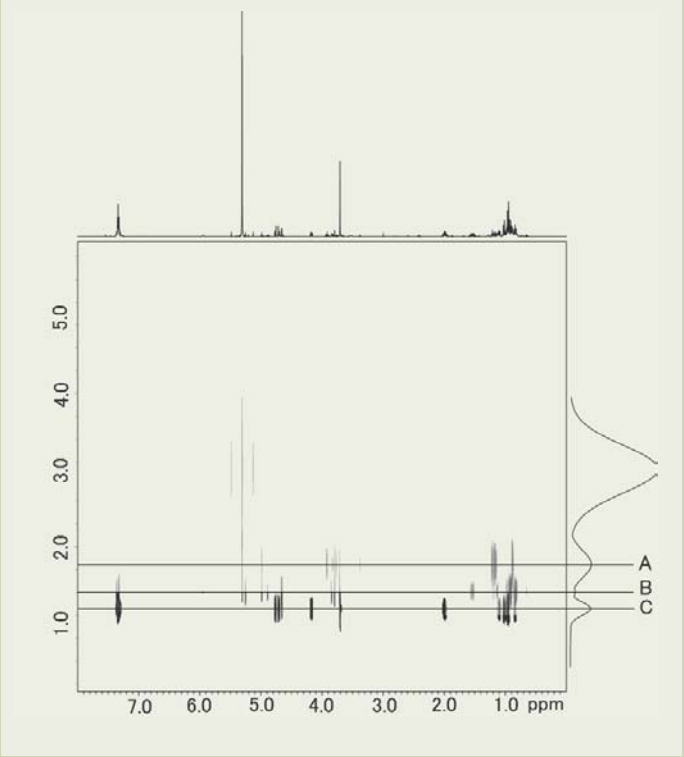

Fig. 7 ^{1}H-DOSY spectrum of reaction mixture.

2''-C, and 1'-H and phenyl C. **Table 2** shows the deduced assignment of ^{1}H and ^{13}C of **3b**, and **Fig. 9** presents the proposed structure of **2b** and **3b**.

In order to confirm the structure of the proposed intermediate **3b**, two-dimensional NMR experiments were carried out (^{1}H–^{15}N PFG-HMBC, ^{1}H–^{11}B PFG-HMBC and NOESY). In the NOESY spectrum, cross peaks between the 2-H signal at 4.18 ppm and the ^{1}H signal (1''-H) of the methyl group at 0.85 ppm were observed. In the ^{1}H–^{11}B HMBC spectrum, a cross peak between the ^{11}B signal at 53.8 ppm and the ^{1}H signal (1''-H) of the methyl group at 0.85 ppm were also observed. We also observed a cross peak between the ^{15}N signal at 195 ppm and the methyl signal (1''-H) at 0.85 ppm in the ^{1}H–^{15}N HMBC spectrum. Furthermore, the proposed structure of **3b** in Fig. 9 was unambiguously supported by the mass spectrum, which exhibits an ion peak of 292 $(MH)^{+}$ by the electrospray ionization (ESI) method.

Conclusion

Unlike LC-NMR, the DOSY method is very effective for the direct analysis of multi components, which does not require chromatography. In particular, the application of the DOSY method to the analysis of labile and nonisolable compounds provides the greatest advantage of this method. The structural determination of the unstable reaction intermediate demonstrated in this paper requires the assumption that the intermediate exists stably in the measured solvent during NMR analysis. This paper showed that we successfully applied the DOSY method to a new analysis field. This success will be expected to extend DOSY-NMR to a wider range of routine measurements.

This research was carried out with Dr. Naito, Dr. Miyata, Dr. Ueda and Dr. Sugiura at Kobe Pharmaceutical University. The author is very grateful to their support. The author also acknowledges Mr. Utsumi and Mr. Sakurai at Analytical Instruments Division of JEOL for their great collaboration in the DOSY-NMR measurements.

References

[1] Morris KF and Johonson CS. *J. Am. Chem. Soc*., **114**, 3139 (1992).
[2] Morris KF and Johonson CS. *J. Am. Chem. Soc*., **115**, 4291 (1993).
[3] Gibbs SJ and Johnson CS Jr. *J. Magn. Reson*., **93**, 395 (1991).
[4] Wu D, Chen A and Johnson CS Jr. *J. Magn. Reson., Ser. A*, **115**, 260 (1995).
[5] Pelta MD, Barjat H, Morris GA, Davis AL and Hammond SJ. *Magn. Reson. Chem.*, **36**, 706 (1998).
[6] Wu D, Chen A and Johnson CS Jr. *J. Magn. Reson., Ser. A*, **115**, 260 (1995).
[7] Provenvher SW and Vogel RH. Numerical Treatment of Inverse Problem in Differential and Integral Equations. DeuflhardP, Hairer E (eds). Birkhauser: Boston, 304 (1983).
[8] Wu D, Chen AD and Johnson CS Jr. *J. Magn. Reson., Ser. B* ,**121**, 88 (1998).
[9] Barjeat H, Morris GA and Swanson AG. *J. Magn. Reson*., **131**, 131 (1998).
[10] Gozansk EK and Gokenstes SG. *J. Magn. Reson., Ser. A*, **111**, 94 (1996).
[11] Soblev AP, Segre A and Lamanna R. *Magn. Reson. Chem*., **41**, 217 (2003).
[12] Groves P, Rasmussen MO, Molero MD, Samain E, Canada FJ, Driguez H and Jimenez-Barbero *J. Glycobiology*, **14**, 451 (2004).
[13] Miyabe H, Ueda M and Naito T. *Synlett*, 1140 (2004).

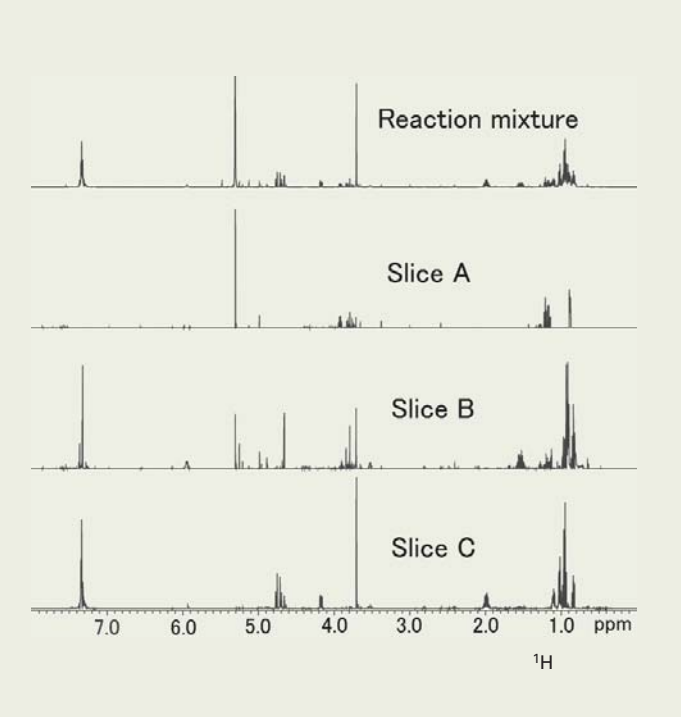

Fig. 8 ^{1}H spectra of reaction mixture and each slice.
Slice A : Triethylborane (Et_3B)
Slice B : Derivative 2b
Slice C : Intermediate 3b

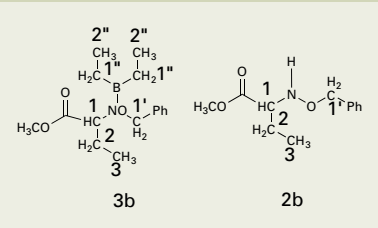

Fig. 9 Structure of 3b and 2b.

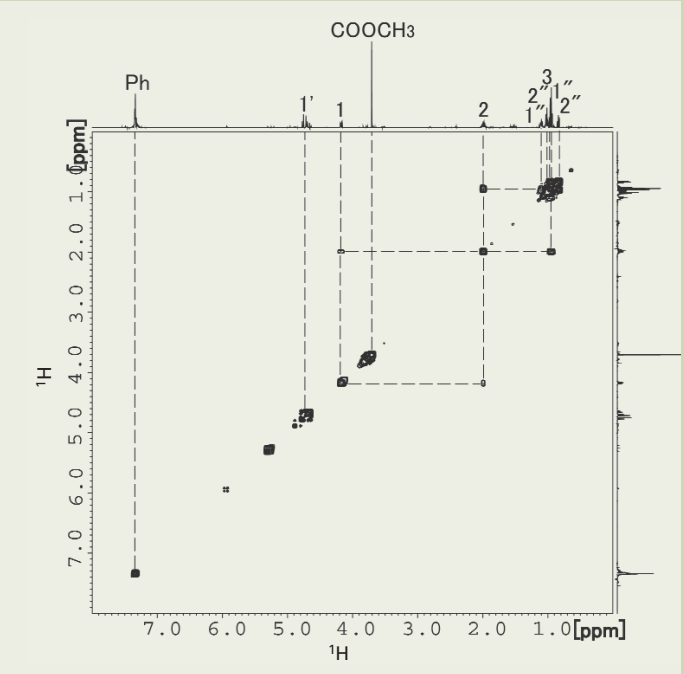

Fig. 10 DOSY-COSY slice spectrum of 3b in reaction mixture.

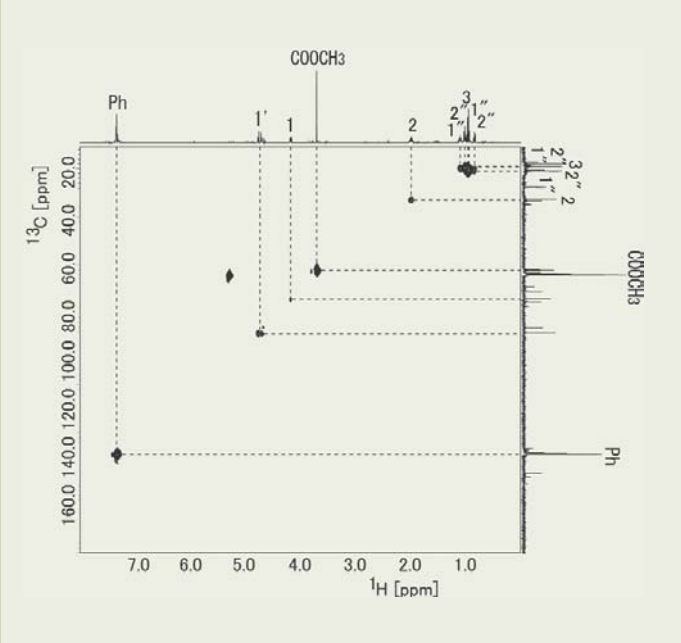

Fig. 11 DOSY-HMQC slice spectrum of 3b in reaction mixture.

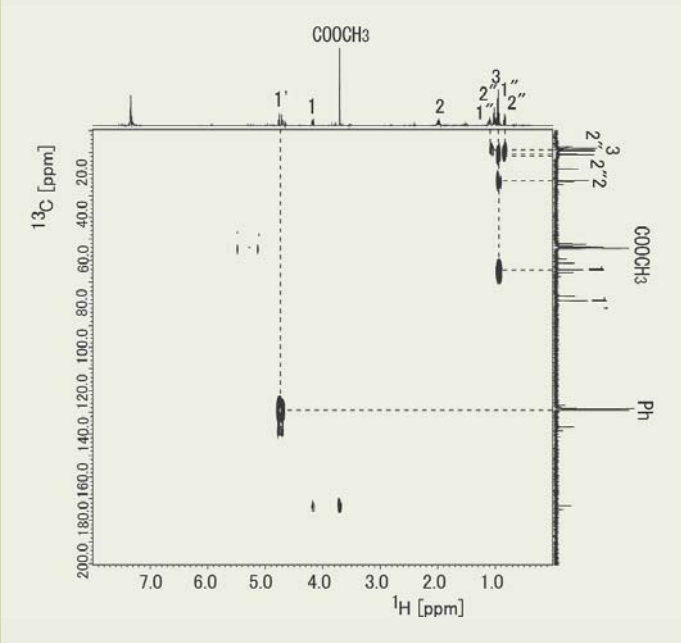

Fig. 12 DOSY-HMBC slice spectrum of 3a in reaction mixture.

Table 2 ^{1}H NMR Data of 3b and 2b.

^{1}H	3b (ppm)	2b(ppm)	^{13}C	3b (ppm)
2-H	4.18 (1H,dd,J=6.9)	3.53 (1H,t,J=7)	1-C	173.1
3-H	2.09-1.93 (2H,m)	1.60-1.48 (2H,m)	2-C	64.1
1'-H	4.76 and 4.72	4.67 and 4.66	3-C	22.8
	(2H,Abq, J=9.5)	(2H,Abq, J=11.5)	4-C	11
1"-H	0.85 (2H,br q,J=7)		1'-C	78.3
	1.12 (2H,m)		1"-C	9.06 8.9
2'-H	0.97 (3H,br t,J=7)	3.72(3H,s)	2"-C	10.3 9.38
	1.04 (3H,br t,J=7)			
HN		6.02-5.91 (1H,br s)		
O-CH_3	3.71(3H,s)	3.72 (3H,s)	O-CH_3	51.9

* Signal due to 3b in the reaction mixture

Auger Analyses Using Low Angle Incident Electrons

Kenichi Tsutsumi, Yuji Nagasawa and Toyohiko Tazawa

Electron Optics Division, JEOL Ltd.

Introduction

Auger Electron Spectroscopy (AES) is widely used, as well as X-ray Photoelectron Spectroscopy (XPS), for surface analyses such as foreign particle analysis and structure analysis, because it can analyze a shallow surface, for example, about a 6 nm deep region from the top surface of a sample. In recent years, many high-technology materials, including not only high-density storage media such as hard disks and DVDs but also functional materials with a special treatment processed in the 1 to 2 nm region from the surface, have been developed, ever increasing the requirement for analyzing a shallow surface of less than the 6 nm deep region. When analyzing such a sample, most researchers generally analyze it by applying a special XPS method such as Angular Resolved X-ray Photoelectron Spectroscopy (ARXPS) or Total Reflection X-ray Photoelectron Spectroscopy. When actually applying these methods, however, it is presupposed that the sample must have an extremely flat and homogeneous surface with a broad area of a few square millimeters. For this reason, if the sample does not have a homogeneous surface lacking in uniformity or the sample has a surface area too small to analyze, it is very difficult to measure and evaluate the sample. Consequently, there is great hope to establish a method for analyzing the thin film surface of a 1 to 2 nm deep region using an AES with a high special resolution. However, since the AES detects Auger electrons, unlike the XPS, by exciting the sample with electrons, it originally has a low PB ratio, and moreover, if one wants to analyze the sample using a shallow detection angle like the ARXPS, it becomes difficult to detect a peak itself because the sensitivity goes down. As a result, it was not possible to analyze the 1 to 2 nm deep thin film using the method of lowering the detection angle. Therefore, in the present article, we propose and introduce the low angle incident electron Auger analysis method, which enables one to analyze the surface of the 1 to 2 nm deep region by irradiating it with the low angle incident electrons, even though scarifying the spatial resolution a little.

Here, we observe the variation of the Auger spectra for the sample of tilted angles, by citing the sample of hard disk as an example; and then, we consider the principle and the depth resolution of the low angle incident electron Auger analysis.

Sample Angle Dependence for The Auger Spectra in a Hard Disk

Escape depth of Auger electron and the thin film structure of a hard disk

To start with, we describe the escape depth of an Auger electron. **Figure 1** shows a graph (left) representing the relationship between the kinetic energy of an electron and the mean free path (λ_0). **Figure 1** also shows another graph (right) representing the relationship between the escape depth of the Auger electron and the total detection amount by taking into account the fact that the energy of the Auger electron attenuates by being scattered inside the sample.

The mean free path represents the average distance that an electron having a definite energy in a substance can move without causing any energy loss by its interaction with other electrons, and its value does not greatly depend on the kind of the substance, but generally depends on the kinetic energy of the electron. Since the Auger electron is hardly distinguishable from other secondary electrons except for the fact, in particular, that it has a characteristic kinetic energy, it must escape from the surface of the substance without causing any energy loss after it is generated on the surface; so there is a close relationship between the escape depth and the mean free path of the Auger electron.

In addition, it is known that the number of the electrons, which can escape from the inside of the sample, decreases exponentially according to the depths of the generated electrons, because they are scattered inside the substance. **Figure 1** (**right**) shows the phenomenon described above. If one calculates the amount of escaped electrons by integrating them for the escape depth up to 3 times of the mean free path (λ_0) by letting the total amount of escapable Auger electrons to 1, it occupies 95% of the total amount; so the escape depth of the Auger electron corresponds to about 3 times of the mean free path.

More specifically, since the Auger analysis employs the electrons having energies from 0 to 2000 eV, the mean free path becomes about 2 nm at maximum according to **Fig. 1** (**left**); so the maximum escape depth of the Auger electron is considered to be about 6 nm.

As described above, since the escape depth of Auger electron becomes constant depending on the kinetic energy of the electron, one can selectively detect the element present near the surface more by decreasing the detection angle for the surface of the sample, To study it, we conducted the experiment of the sample tilt angle dependence in the AES using a sample of a hard disk whose structure is known.

Figure 2 illustrates the layer structure of the hard disk employed in the present experiment. Inside the hard disk, there exists a 15 to 25 nm thick magnetic layer containing Co for recording data, on the later, there exists a 3 to 5 nm thick diamond-like carbon (DLC) layer for protecting the magnetic layer, and on the top surface, a lubricant agent containing F is applied for a 1 to 2 nm thickness so that the slider for reading the magnetic information can move smoothly. The thickness of each layer introduced here is only applicable for hard disks produced a few years ago. The thickness of each layer in recently produced hard disks is made much thinner than this.

Looking at the layer structure of this hard disk, the depth from the surface to the magnetic layer is nearly equal to the escape depth of the Auger electron, indicating it is a most suitable sample for studying the sample tilt angle dependence of the Auger electron.

Instrument configuration (JAMP-9500F) employed in the experiment and the experimental results

The instrument employed in the present experiment is the JEOL Field Emission Auger Microprobe JAMP-9500F, having a structure as shown in **Fig. 3**. The JAMP-9500F is equipped with a eucentric stage in the ultra-high vacuum chamber, having a feature that the detector does not miss the analyzable region even though an operator moves the sample in the x or y direction, or tilts the sample, once the operator sets the sample surface in the eucentric allocation. The sample tilt angle is the angle θ, shown in **Fig. 3**, between the direction of the incident electrons and the normal to the sample surface. In addition, the angle between the direction of the incident electrons and the detecting direction of the electrostatic hemispherical analyzer is fixed at 60°; in this experiment, when one tilts the sample, both the incident angle of the electron beam and the detection angle change simulta-

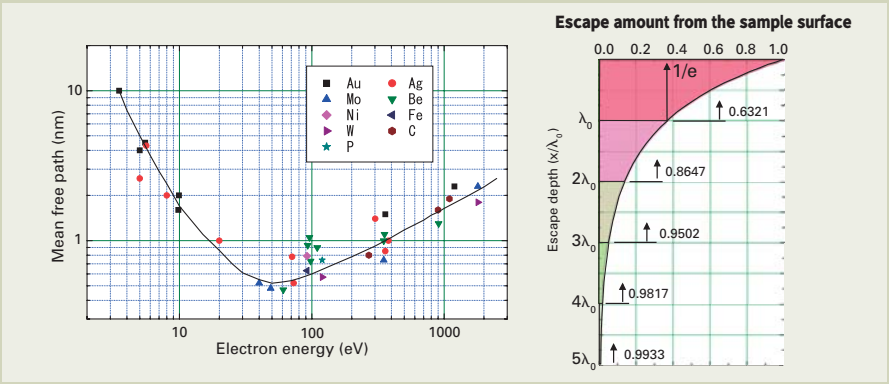

Fig. 1 Energy dependence of the electron mean free path (λ_0) and the relationship between the escape depth of Auger electron and the total detection amount.

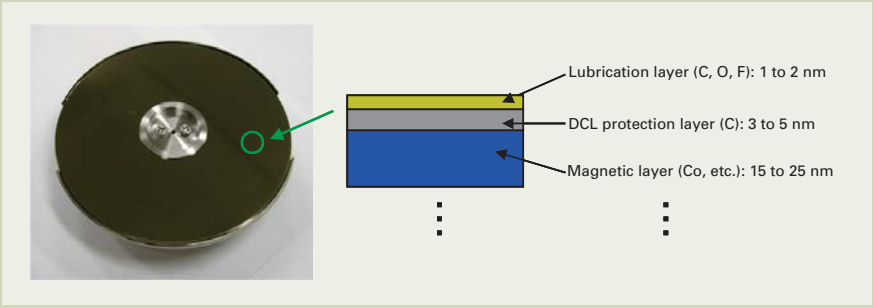

Fig. 2 Layer structure of the hard disk employed in the experiment.

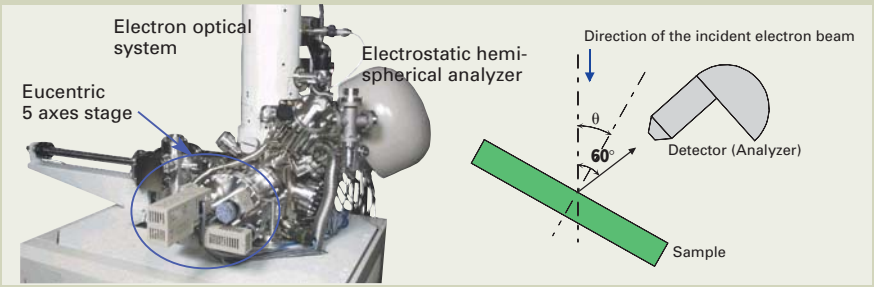

Fig. 3 Sample tilt angle and the detection angle of the analyzer in the JAMP-9500F.

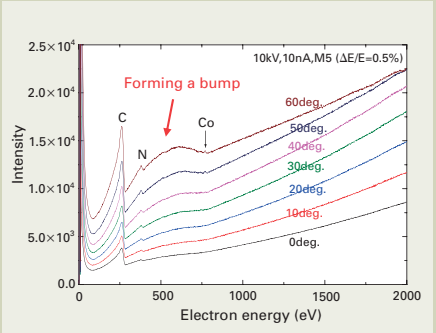

Fig. 4 Variation of the Auger spectra when changing the sample tilt angle from 0 to 60°.

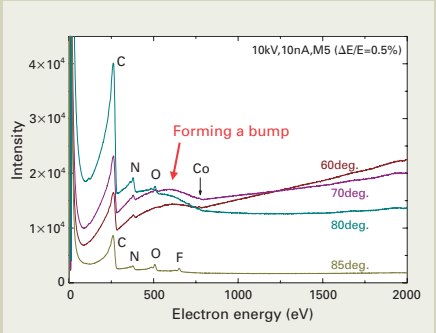

Fig. 5 Variation of the Auger spectra when changing the sample tilt angle from 60 to 85°.

neously.

By using this instrument, we studied the sample tilt angle dependence of the Auger spectra in the sample of the hard disk described in the section of "Escape depth of Auger electron and the thin film structure of a hard disk." **Figure 4** shows the variation of the spectra when changing the sample tilt angle from 0 to 60°. **Figure 5** shows the variation of the spectra when changing the sample tilt angle from 60 to 85°.

Looking at the spectra in **Fig. 4**, we can find that the C, N and Co peaks gradually grow larger and also the intensity of the entire spectrum increases as we change the sample tilt angle from 0 to 60°. At the same time, we can also find that a large bump is formed in the energy region from the Co peak (770 eV) to the lower energy side, and its size increases as the sample tilt angle increases.

Looking at the spectra in **Fig. 5**, we can find that the Co peak gets smaller and also the intensity of the entire spectrum decreases as the sample tilt angle increases, and that when the sample is tilted to 85°, the Co peak disappears and the F peak is detected instead. In the next section, we consider the cause for the variation of these spectra.

The cause for emerging a bump in the spectrum

In **Figs 4** and **5**, a bump appearing in the lower energy side than the energy of the Co peak is considered to be caused by the energy loss of the Co peak. We illustrate the reason for it in **Fig. 6**.

As shown in **Fig. 6**, if the electron beam enters into the sample and generates the Auger electron at the position of depth L, since the angle between the direction of the incident electron beam and the detector (analyzer) is 60°, the distance that the Auger electron actually passes through the inside of the sample until it is detected is Le. As this length of Le becomes the shorter, the deeper the Auger electron can be detected; when the sample is tilted to 60°, it becomes shortest. Therefore, when the sample tilt angle is 60°, the peak of Co in the magnetic layer that exists at the deepest region from the surface is most largely detected. However, not all the Auger electrons of Co are detected with their energies preserved, but some of them enter the detector by losing their energies. As a result, some of the Auger electrons of Co are not detected at the original peak energy position, but they form a bump having a broad energy distribution as shown in **Fig. 6**.

Sample tilt angle and its dependence on the Auger peak intensity

Next, by tilting the sample, we consider theoretically how the Auger peak intensity of each element varies [1].

For the instrument composition shown in **Fig. 3**, when the sample is tilted, both the incident angle of the electron beam and the detection angle of the Auger electron change simultaneously. Hence, we consider the variation of the generation amount of the Auger electrons depending on the incident angle of the electron beam and the variation of the detection amount depending on the detection angle for the surface, respectively.

Firstly, we consider the variation of the generation amount of the Auger electrons. Suppose that the sample is tilted θ for the incident angle of the electron beam, and the Auger electrons are generated from the sample element along the depth L as shown in **Fig. 7 (a)**. If we further suppose that the Auger electrons

generated at each point of the depth L are absorbed by the sample material attenuating its intensities until they escape from the sample surface, the number of the generated Auger electrons is expressed as Equation (1). From this equation, we can find that it is proportional to 1/cos θ.

$$N = \int_0^\infty n\, e^{-kx} dL = \int_0^\infty n e^{-kL\cos\theta} dL = \frac{n}{k}\frac{1}{\cos\theta} \quad (1)$$

N : Total amount of Auger electrons generated from the sample surface
n : Number of Auger electrons generated by unit length
k : Attenuation coefficient
x : Distance from the generation point of secondary electron to the sample surface (x=L·cos θ)

Next, we consider the variation of the detection amount by changing the detection angle for the surface. As shown in **Fig. 7 (b)**, the relationship between the detection amount of the Auger electrons and the detection angle is supposed to be compared to the situation that for a hypothetical sphere S, the chord length E at the detection angle ψ corresponds to the detection amount. In other words, the detection amount is largest in the direction perpendicular to the sample surface; conversely, the detection angle to the sample surface becomes the lower, the smaller the detection amount. Let E_0 (the detection amount at the tilt angle 0°) be the diameter of the hypothetical sphere S, the detection amount at the tilt angle y is expressed as Equation (2).

$$E = E_0 \cos\psi \quad (2)$$

In the actual instrument, if we suppose that there is an angle difference ϕ between the directions of the incident electron beam and the detector, and let θ be the sample tilt angle, the instrument geometry can be shown as **Fig. 8**. Consequently, by taking the generation amount and the detection amount of the Auger electrons into account, we define the amount of the measured Auger electrons. Calculating the product of Equation (1) and Equation (2) leads to Equation (3) as described below.

$$\text{From } N = \frac{n}{k}\frac{1}{\cos\theta} \text{ and } E = E_0\cos(\phi-\theta) \quad (\because \psi = \phi - \theta)$$

$$I_\theta = N\cdot E = \frac{nE_0}{k}\frac{\cos(\phi-\theta)}{\cos\theta} = C_0\frac{\cos\phi\cdot\cos\theta+\sin\phi\cdot\sin\theta}{\cos\theta}$$

$$= C_0(\cos\phi + \sin\phi\cdot\tan\theta) \quad (3)$$

$$\left(\because C_0 = \frac{N\cdot E_0}{k}\right)$$

Here, since the angle between the direction of the incident electron beam and the detector is ϕ = 60°, let I_0 be the detection amount at the sample tilt angle θ= 0° and obtain the intensity ratio at the sample tilt angle θ, then C_0 is eliminated and the intensity ratio becomes as given in Equation (4).

$$\text{(Intensity ratio)} \quad \frac{I_\theta}{I_0} = \sqrt{3}\tan\theta + 1 \quad (4)$$

Figure 9 shows the summary of the relationship between the sample tilt angle and the peak intensity by actually measuring the Auger spectra for the standard bulk samples. The measured samples are three pure metals Ag, Cu and Si; the differential Auger peak intensity ratios of Ag MNN (348 eV), Cu LMM (914 eV) and Si KLL (1614 eV) are plotted for the varied sample tilt angles.

Looking at this graph, we can find that any peak intensities satisfy Equation (4) very well up to the sample tilt angle of 60°. However, for the higher angle of 75° or more, they deviate from Equation (4). This should be considered to be due to the fact that when electrons enter the sample at a low angle for it, the fraction of the electrons that escape from the surface as backscattered electrons increase; the more they increase, the larger the atomic number of the metal composing the sample, decreasing the fraction of the electrons that excite the Auger electrons inside the sample.

Next, we calculate the peak intensity ratio from the analysis results of the hard disk described above and obtain its sample tilt angle dependence, which is shown in **Fig. 10**.

Looking at this result, we can find that the intensity variation of Co takes the maximum value at the tilt angle 60°, showing that the element Co exists in a deeper layer beneath the layer of C, N and O. As for the intensities of C, N and O, they take the maximum values at 80∞, and they decrease at 85°, indicating that these elements exist in the secondary layer from the surface. However, the element F in the lubricant agent that exists in the 1 to 2 nm deep region from the surface is detected for the first time at such a high tilt angle as 85°, and it is not detected at any other angles. In other words, it may be considered that the element present in the top surface is detected for the first time by inserting the electron beam at such a low angle.

As is clear from this measurement result, we can find that the tilt angle dependence of the Auger electron peak intensity reflects the layer structure of the sample surface, and in particular that we can obtain the Auger spectra of the element present in the top surface by inserting the electron beam at a low incident angle. In the next chapter, we consider these issues in more detail.

Auger Analyses Using the Low Angle Incident Electron Beam

Incident angle of the electron beam and the scattering region

As is shown in the previous chapter, when

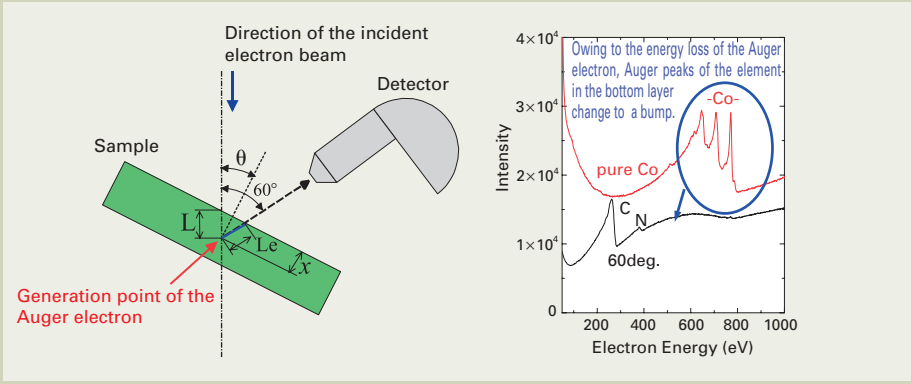

Fig. 6 The cause for forming a bump in the spectrum.

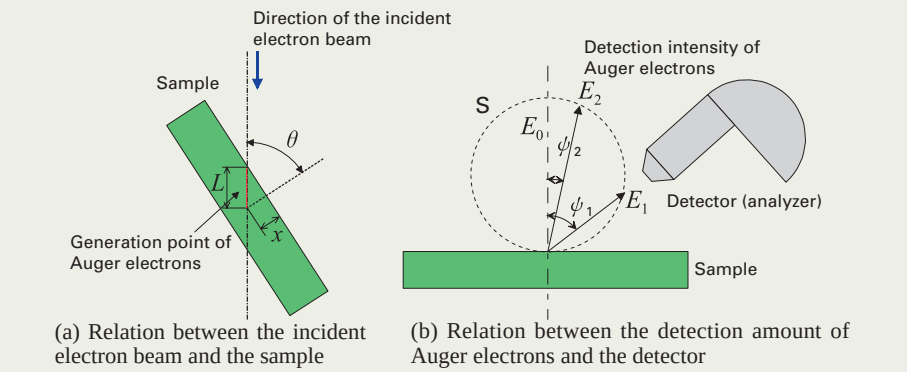

(a) Relation between the incident electron beam and the sample

(b) Relation between the detection amount of Auger electrons and the detector

Fig. 7 Relations between the incident electron beam and the sample, and the detection amount of Auger electrons and the detector.

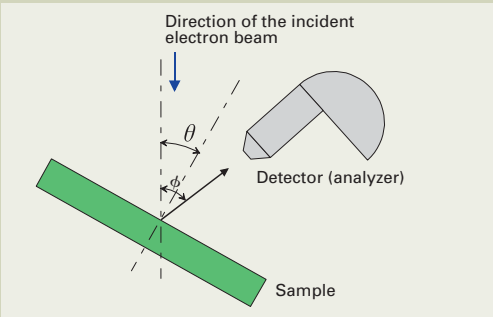

Fig. 8 Measuring the Auger electrons at the sample tilt angle θ.

using a low angle incident electron beam, it is possible to detect the elements present in a top surface region of the sample. Hence, we study the diffusion region of the electron beam when inserting it at a low angle by using the Monte Carlo simulation. **Figure 11** and **Table 1** show the results.

Figure 11 shows the scattering regions of the electron beam when the 10 kV electron beam enters the sample surface that is tilted to 0° and 80°. Looking at the results of this Monte Carlo simulation, we can assume that the region where the electron beam is scattered is a sphere, making it possible to regard the center of the sphere as the scattering center. **Table 1** shows the distance from the surface to the scattering center. At the same time, we show the fraction of the electrons that escaped from the surface as the backscattered electrons among the incident electrons.

Looking at this result, we can find that as the tilt angle increases more, the nearer the scattering center of the electron beam approaches the surface, resulting in the electron beam running the shallow region of the surface. When the sample is tilted to 85°, the scattering center comes to about 6 nm from the surface, the same escape depth of the Auger electron. In this state, since the Auger electron is more effectively generated and detected than that of the tilt angle 0°, it may be possible to obtain a spectrum sensitive to the surface element. In addition, it may also be evident from the fraction of the backscattered electron generation that the more the tilt angle increases, the greater the probability that electrons will escape from the surface as backscattered electrons among the incident electrons, decreasing the electrons diffusing inside the sample. With this, the number of high energy electrons that generate secondary electrons may decrease, conceivably resulting in reducing the background and enhancing the S/N.

Figure 12 shows the comparison of spectra at 30° and 85° shown in **Figs 4** and **5**, respectively in the section of "Instrument configuration (JAMP-9500) employed in the experiment and the experimental results."

As this result shows, the spectra at 30° and 85° appear quite differently from each other, even though they are measured with the same sample. When we compare these spectra, we can find that the spectrum measured using the low angle incident electron beam at the sample tilt angles of 85° has a lower background, and the peak of element F present near the surface is detected more intensely.

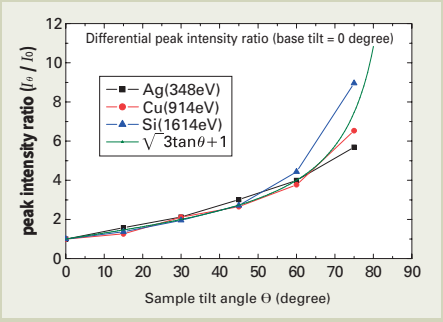

Fig. 9 Relation between the sample tilt angle and the differential Auger peak intensity (when the angle between the direction of incident electron beam and detector is ϕ = 60°).

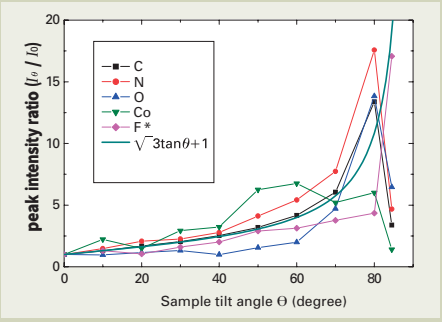

Fig. 10 Sample tilt angle dependence on the Auger peak intensity in a sample of hard disk.

* Intensity of F is calculated from the noise of the F peak position, because it is lower than the value of the statistical fluctuation noise within the range of 0° to 80°.

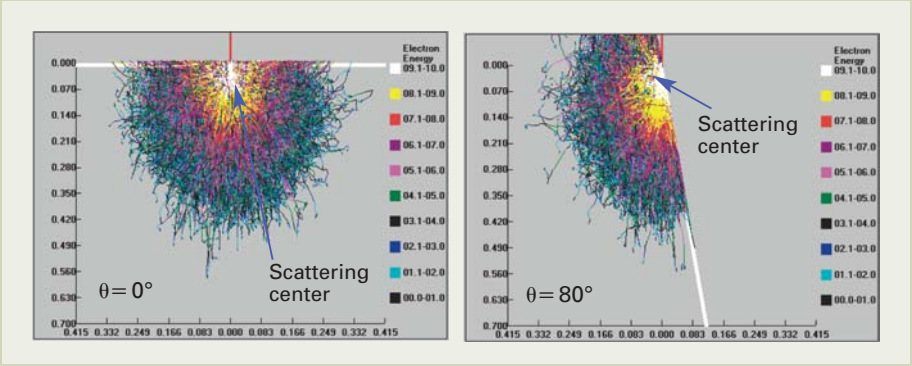

Fig. 11 Results of the Monte Carlo simulation for the diffusion region of the electron beam (θ = 0° and 80°).

Table 1 Distance from the surface to the scattering center and the fraction of the backscattered electron generation.

Sample tilt angle θ (degree)	0	10	20	30	40	50	60	70	80	85	89
Distance from the surface to the scattering canter (nm)	70	69	66	61	54	45	35	24	12	6.1	1.2
Generation of the backscattered electrons (%)	29	29	30	32	34	37	42	50	62	69	81

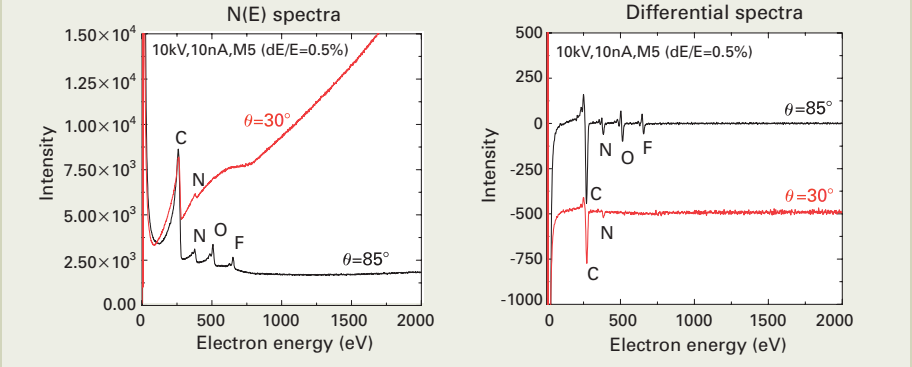

Fig. 12 Comparison of spectra at the sample tilt angles of 30° and 85°.

Low angle incident Auger analysis using a thin film sample (Cr/Si)

We have found that using the low angle incident electron beam makes it possible to excite the top surface element more effectively, enabling us to perform a more sensitive Auger analysis. Here, in order to check what kind of analysis is effective for a thin film sample, we fabricated the sample experimentally and studied the performance of the analysis.

We used a natural oxide removed Si wafer on which the Cr thin film is uniformly coated using the GATAN Precise Coating System (PECS) as a sample. We fabricated four kinds of Cr thin film by controlling the film thickness with the coating time of the PECS varied to 10 s, 20 s, 1 min and 2 min. **Figures 13** and **14** show the sample tilt angle dependence for the Auger spectra of the Si sample on which Cr is coated for 20 s and 2 min, respectively. Looking at these results, we can find that although for the spectrum with the Cr film of 20 s, the substrate Si is detected at any tilt angles, for the spectrum with the Cr film of 2 min, only a bump is finally formed at the tilt angles of 60° to 70°.

Figure 15 shows the summary of the tilt angle dependence for the peak intensity of each detected element. The vertical axis of the graph shown in **Fig. 15** is the normalized peak intensity ratio based on the peak intensity at

the sample tilt angle of 0°. The theoretical curve shown here represents Equation (4) for the peak intensity ratio that is obtained for the bulk sample as shown in **Fig. 9**.

The sample tilt angle dependence of C draws the same curve as the theoretical curve for any sample. This shows that the element C is present at the top surface without any layer above it.

Elements O and Cr draw the same curve, indicating that both elements exist in the same layer. We can infer from this that the sample may have been oxidized while coating Cr on it under an inappropriate environment. In addition, the maximum intensities of O and Cr appear near at 85° for any samples, indicating that the thicknesses of contamination (C) adhered to the surfaces are roughly the same.

The sample tilt angle dependence of the substrate Si differs largely by the film thickness of Cr present on the substrate. As the substrate becomes the thicker, the smaller the tilt angle at which the maximum intensity is obtained. However, as mentioned above, since the detection angle of the analyzer is 60°, the tilt angle of 60° is the lower limit; therefore if the maximum intensity is obtained at the tilt angle of 60°, as the film thickness increases, the tilt angle at which the maximum intensity is obtained cannot decrease, but the detection intensity decreases.

As mentioned above, it is found that if the sample tilt angle is larger than 60°, the thin film sample also gives the similar tilt angle dependence as is obtained using the XPS. The quantitative analysis like discussions such as obtaining the film thickness or other values from the graph that has the tilt angle dependence are left to future research challenges.

Resolution of depth profile in the low angle incident Auger analysis

In the previous sections, we have shown that utilizing a low angle incident electron beam enables one to perform a more sensitive Auger analysis. In this section, we study how much depth resolution is obtained if we apply this method to depth profile.

The sample used in the experiment is a 20 nm thick SiO_2 film that is formed on a Si substrate. As is generally known, a SiO_2 film formed on a Si wafer has not only a precise film thickness but also a very steep interface between SiO_2 and Si at the atomic level: so it is widely used as a reference sample for measuring the sputtering rate. For this SiO_2/Si interface, we studied how much the resolution of the depth profiles improves when using the tilt angle (30°) of normal measurement condition and when using the low angle incident electron beam (85°). **Figure 16** shows the result. In this experiment, we measured the depth profiles with a high energy resolution (ΔE/E=0.05%), and by splitting the metal and oxide peaks in chemically different states from the Si KLL and LVV peaks, we plotted these depth profiles independently.

Figure 16 shows that the depth profile using the low angle incident electron beam at the tilt angle of 85° is clearly more improved in the steepness of the interface than the other depth profile. When we obtain the difference between depths that become 16% and 84% of the maximum intensity for each peak, and define the width as the resolution of the depth profile, we can summarize the results as **Table 2.** When we compare these results, in the Si KLL (metal) peak of the depth profile with the worst resolution, the resolution at the tilt angle of 85° becomes 60% of that of 30°. Particularly, for the peaks in the high energy side, since the resolution of the depth profile deteriorates because the Auger electrons that escaped from the deep region with a long mean free path are detected, the effect of improvement by this method is significant.

As mentioned above, we proved that if we utilize the low angle incident electron beam, we can measure a higher resolution depth profile.

Comparing with X-ray photoelectron spectroscopy (XPS)

Before implementing the surface structure analysis using the low angle incident electron beam, we compared it with the already launched Angular Resolved X-ray Photoelectron Spectroscopy (ARXPS). We used the Si substrate with Cr film coated on it as the sample that is used in the section of "Low angle incident Auger analysis using a thin film sample (Cr/Si)" , employed the JEOL JPS-9010MX for the ARXPS, and compared the quantitative analysis results at each tilt angle. **Figures 17** and **18** show the compared results for Cr film (20 s) and Cr film (1 min), respectively. The left figure shows the result of the ARXPS and the right figure shows the result of the angle tilted Auger analysis.

Looking at each result, it shows that in the ARXPS, as the tilt angle varies, the intensity of each element gradually varies; on the other hand, in the angle tilted Auger analysis, it varies rapidly near from 70°. Insofar as this

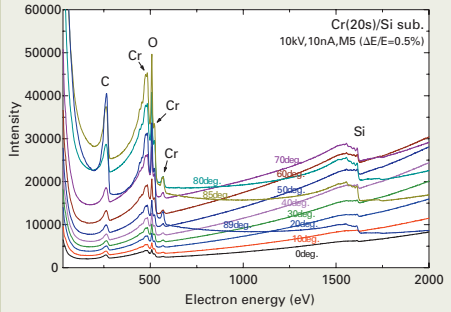

Fig. 13 Sample tilt angle dependence of the Si sample on which Cr is coated for 20 s.

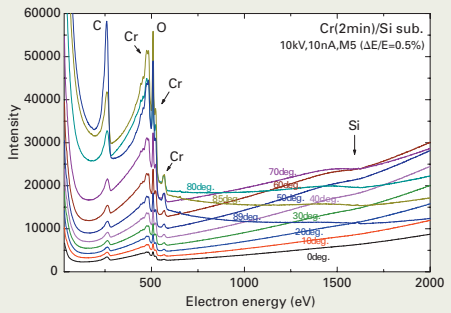

Fig. 14 Sample tilt angle dependence of the Si sample on which Cr is coated for 2 min.

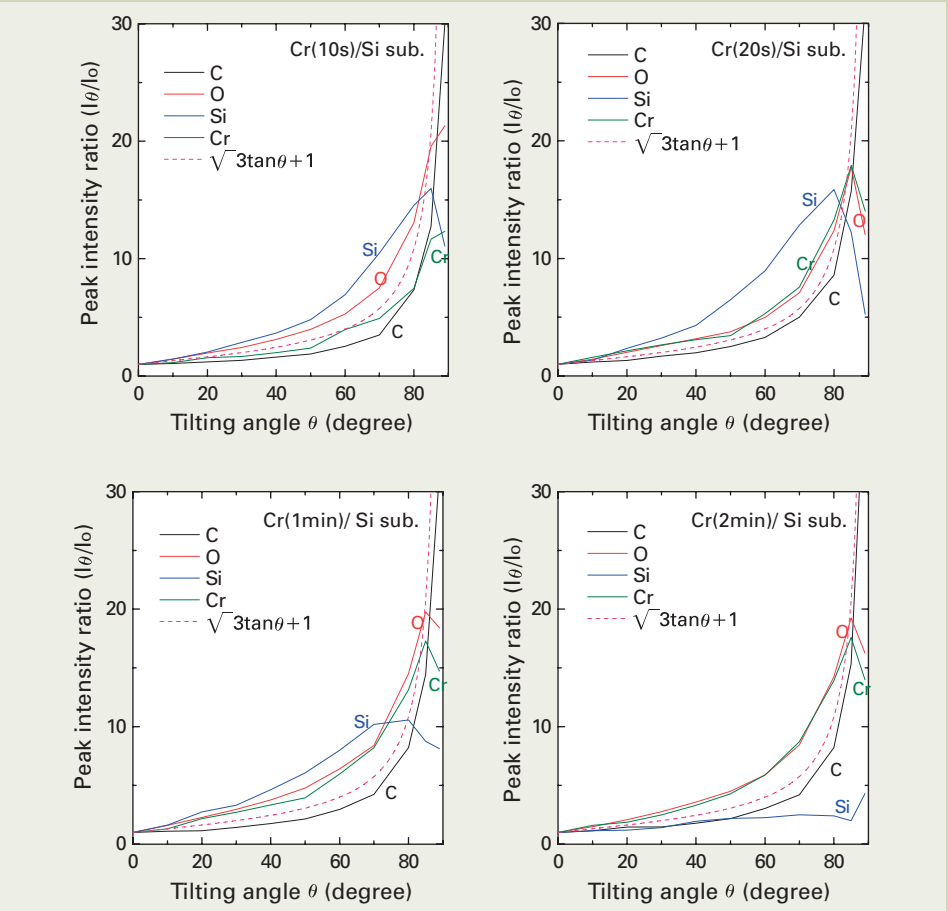

Fig. 15 Variation of peak intensity for each element in the Cr coated Si sample.

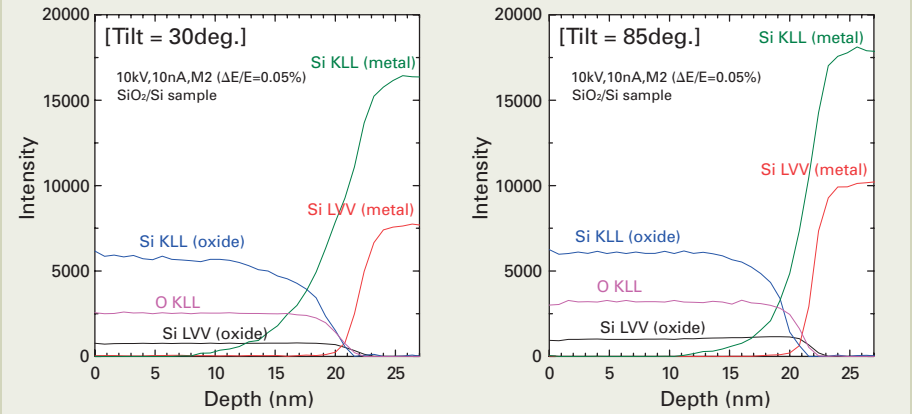

Fig. 16 Difference of depth profiles at the tilt angle of 30° and 85°.

Table 2 Variation of the resolution of depth profile in each peak (width of 16% - 84%).

Sample tilt angle (Elevation angle from the sample surface to the ion gun)	Tilt = 30deg. (49.5 °)	Tilt = 85deg. (35 °)
Si LVV (oxide) 76eV	2.2 nm	1.4 nm
Si LVV (metal) 92eV	2.0 nm	1.8 nm
O KLL 510eV	2.6 nm	2.1 nm
Si KLL (oxide) 1604eV	5.6 nm	3.5 nm
Si KLL (metal) 1615eV	6.2 nm	3.7 nm

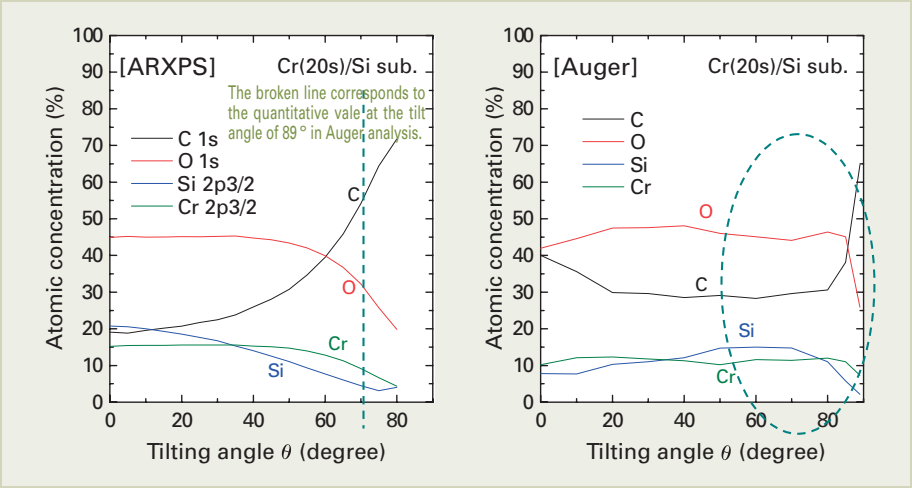

Fig. 17 Comparison of the quantitative results for the Si sample on which Cr is coated for 20 s.

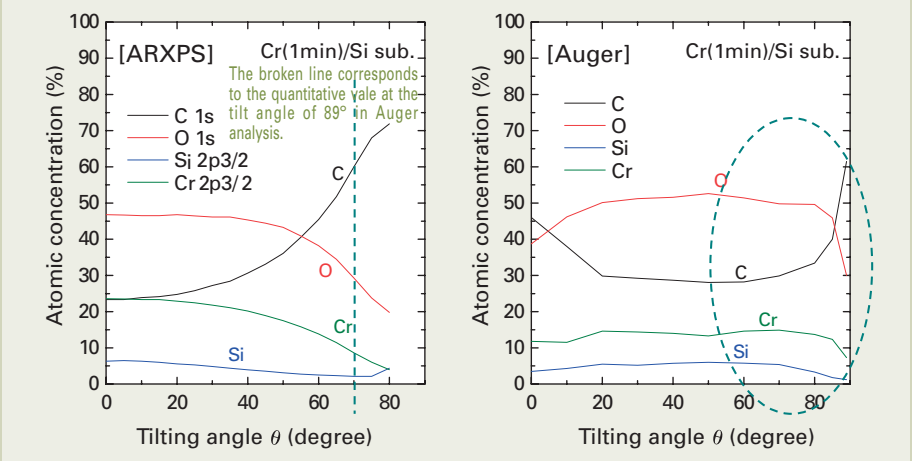

Fig. 18 Comparison of the quantitative results for the Si sample on which Cr is coated for 1 min.

experiment, we can find that the sample tilt angle dependence within the tilt angle range of 60° to 90° in the Auger analysis gives a similar performance as the result of the tilt angle range of 0° to 80° in the ARXPS.

In addition, if we compare only the quantitative analysis results, we can find that the quantitative analysis value in the low angle incident Auger analysis at the tilt angle of 89° corresponds to that value in the ARXPS at the tilt angle of nearly 70° to 73°. According to the theory of the ARXPS, at the tilt angle of 70° to 73°, it analyzes about a 30% (about 2 nm) shallower region from the surface compared with the detection depth at the tilt angle of 0°. Of course, since the kinetic energies of detecting electrons differ between the Auger analysis and the XPS, it may be unreliable to discuss the detection depth simply from the quantitative values, but we showed it here as a guideline.

As mentioned above, the low angle incident Auger analysis with the sample tilted by 70° or more gives a similar performance as the ARXPS, indicating the possibility of the surface structure analysis of a thin film with a thickness of a few nm.

Conclusion

It is said that the detection depth of the ordinary Auger electrons is about 6 nm; so it was very difficult to analyze a film thinner than 6 nm such as a 1 to 2 nm thick film. When we measure such a sample, we had to use the XPS and apply the ARXPS method or the TRXPS method. However, it is not possible to apply these methods to all the samples; it is very difficult to measure and evaluate a sample that has a surface irregularity or a too small region to analyze. Hence, we propose to study the low angle incident Auger analysis.

We showed that for the sample of a hard disk, when we tilt the sample by 70° to insert the electron beam at a low incident angle, we can measure the spectra of a 1 to 2 nm deep region from the surface of the lubricant layer. We also showed that by comparing the data with that of the ARXPS, the angular dependence of the sample tilt angle of 60° or more gives a similar performance as that of the ARXPS, making it possible to analyze the sample according to the structure of the thin film. We found that when we apply the low angle incident Auger analysis to the depth profile, it improves the steepness of the interface, enabling one to obtain a higher resolution depth profile. We showed that at the sample tilt angle of 89°, although the instrument analyzes the region that is expanded to about 60 times longer in the tilted direction than that when inserting the beam perpendicular to the surface, the instrument can analyze a shallow region less than or equal to 2 nm from the surface.

In the future, we will clarify the low angle incident Auger analysis theoretically, and study the analysis depth and the accuracy of the quantitative analysis.

Reference

[1] Kenichi Tsutsumi: JEOL EPMA•Surface Analysis Users' Meeting document (AP94)

Examination of Analytical Conditions for Trace Elements Based on the Detection Limit of EPMA (WDS)

Ayako Sato, Norihisa Mori, Masaru Takakura and Satoshi Notoya

Electron Optics Division, JEOL Ltd.

Introduction

The EPMA (Electron Probe Microanalyzer) with WDS (Wavelength Dispersive X-ray Spectrometer) is a typical instrument for surface analysis. This powerful instrument features high energy (wavelength) resolution and high capability for detecting trace elements and for analyzing light elements, compared to SEM-EDS (Scanning Electron Microscope with Energy Dispersive X-ray Spectrometer) that is also a common analytical instrument.

The advantage of WDS over SEM-EDS in energy resolution is well known: There are many cases where adjacent X-ray spectral peaks can be separated by WDS but these peaks overlap in the EDS spectra. Owing to its high energy resolution, WDS is advantageous over EDS in the analysis of trace elements and light elements. **Table 1** shows the general detection limits which mean the minimum concentrations which can be measured by WDS and EDS. These values are variable depending on elements to be measured, sample composition, and analytical conditions. Thus, the numerical values in **Table 1** do not necessarily correspond to the practical detection limits in trace elements analysis.

We obtained the detection limits in normal analytical conditions of EPMA and examined the practical concentration which can be measured. In addition, we will show applications of EPMA to magnetic materials to demonstrate the high capability of analyzing trace elements by the EPMA.

Detection Limits in Qualitative and Quantitative Analysis (Point Analysis)

Although there are many equations that give the detection limit, in this article, we define the detection limit by the following equation (1). This equation assumes that the peak should be detected if the net intensity of X-rays $P_{cnt} - B_{cnt}$ is more than three times of the standard deviation of background $\sqrt{B_{cnt}}$. Thus, this equation enables us to distinguish the significant difference between $P_{cnt} - B_{cnt}$ and $\sqrt{B_{cnt}}$ with 99.7% confidence level.

$$C_{DL} = \frac{3\sqrt{B_{cnt}}}{P_{cnt} - B_{cnt}} C_0 \quad \cdots\cdots (1)$$

C_{DL} : Detection limit (mass%)
P_{cnt} : X-ray intensity of spectral peak (count)
B_{cnt} : X-ray intensity of background (count)
C_0 : Concentration of the element of interest in the standard (mass%)

In equation (1), if we convert P_{cnt} and B_{cnt} into count rate per unit time and unit probe current, equation (2) can be obtained, showing that the detection limit improves in proportion to the square root of the probe current and the measurement time.

$$C_{DL} = \frac{3\sqrt{B}}{(P - B)\sqrt{i \cdot t}} C_0 \quad \cdots\cdots (2)$$

C_{DL} : Detection limit (mass%)
P : X-ray count rate of spectral peak (cps/μA)
B : X-ray count rate of background (cps/μA)
i : Current (μA), t: Time (sec)
C_0 : Concentration of the element of interest in the standard (mass%)

We actually measured the X-ray intensities under six types of analytical conditions normally used in EPMA. Then, we applied equation (1) to the measurement results and calculated the detection limits for each condition. **Table 2** lists the analytical conditions for obtaining the detection limits, and the details of each condition are explained below.

① Qualitative analysis of all elements (Qual.: all): This qualitative analysis condition is applied to the first analysis of unknown specimens. The wavelength range of all elements is measured and X-rays are detected. Since the wavelength-scanning range is wide, measurement time of every wavelength is set short and the total measurement time is long. Note that the total measurement time (5 minutes) is adopted with the EPMA instrument used in this examination, so this time differs depending on the configuration of X-ray spectrometers and analyzing crystals.

② Detection of trace elements (Qual.: trace): This qualitative analysis condition aims to mainly detect trace elements. The wavelength range of one or more specific elements is measured. Compared to condition ①, the measurement time of every wavelength is set long and the scanning steps are fine. Since the wavelength-scanning range is narrower than condition ①, the total measurement time is short.

③ Normal quantitative analysis (Quant.: normal): This is a normal quantitative analysis condition. The measurement time of the wavelength is longer than qualitative analysis. In order to suppress the counting loss, the probe current is set low compared to qualitative analysis. Measurement times are 20 seconds for peak and 10 seconds for background. The total measurement time including the time to move the analyzing crystals is set to about 1 minute.

④ Quantitative analysis of trace elements (Quant.: trace): This quantitative analysis condition is applied to the measurement of trace elements. Compared to condition ③, the probe current is set high.

⑤ EDS 5 minutes analysis (EDS: 5 min.): This condition is applied to the measurement of the full energy range by EDS. We set the measurement time to the time same as WDS analytical condition ① (5 minutes). Here, the measurement time means the real time in EDS analysis. We adjusted the probe current so that the dead time was optimized for the highest detection sensitivity and minimum detection limit.

⑥ EDS 1 minute analysis (EDS: 1 min.): The detection limits for this condition are calculated from the results of condition ⑤.

Using the above analytical conditions, we calculated the detection limits for a typical heavy element Ni and a typical light element

Table 1 General detection limits of WDS and EDS [1].

	WDS	EDS
Light elements (B to F)	0.01 to 0.05 mass% (100 to 500ppm)	1 to 10 mass%
Heavy elements (Na to U)	0.001 to 0.01 mass% (10 to 100ppm)	0.1 to 0.5 mass%

Table 2 Six analytical conditions for obtaining the detection limits.

	Analytical method	Name	Probe current	Time	Remarks
WDS	Qualitative analysis (spectral collection)	① Qual.: all	100nA	5minutes*2	Qualitative analysis condition for all elements.
		② Qual.: trace	100nA	1minute	Qualitative analysis condition for trace elements.
	Quantitative analysis	③ Quant.: normal	50nA	1minute*3	Normal quantitative analysis condition
		④ Quant.: trace	500nA	1minute*3	Quantitative analysis condition for trace elements
EDS	Spectral collection	⑤ EDS: 5 min.	*1	5minutes*4	Spectral collection by EDS
		⑥ EDS: 1 min.	*1	1minute*4	⑥ : Calculated from condition ⑤.

*1 Adjusted to optimize the detection limit.
*2 Measurement time is set depending on the configuration of X-ray spectrometers and analyzing crystals in the instrument used for measurement.
*3 Measurement time is set to 1 minute, including the time to move the analyzing crystals. (Peak : 20seconds, BG : 10 seconds)
*4 Real time

Table 3 Measured specimens

Specimen	Ni (mass %)
Ni	100.00
Ni_2Si	80.70
Stainless steel	10.40
Low-alloy steel	2.00
Cr-V steel	0.32

Specimen	B (mass %)
B	100.00
BN	43.56
FeB	16.20
Fe_2B	8.80
Danburite	8.63
Axinite	1.25

B. Measurements were performed for multiple specimens having different concentrations of Ni and B. **Table 3** shows the measured specimens and the concentrations of Ni and B. The accelerating voltage was set to 15 kV for measuring Ni and 10 kV for measuring B. The probe diameter was set to 20 μm. However, since the structure sizes of FeB and Fe_2B are small, the probe diameter of 2 μm was applied to measure these two specimens.

Figure 1 shows each detection limit C_{DL} for Ni and B for the six analytical conditions. The detection limit for Ni shows constant values regardless of its concentration, whereas the detection limit for B differs remarkably depending on its concentration. For example, the detection limit for Danburite (B: 8.63%) is three times or more worse than that for the standard specimen (B: 100%). This fact reflects that the light elements are severely absorbed by the matrix. Thus, in practical measurement of trace elements, the detection limit value for heavy elements is given by the value approximately the same as the standard specimen (pure substance); however, it is possible that the detection limit for light elements becomes three times or more worse than that for the standard specimen. Furthermore, in EDS analysis, not only the absorption effect but also the effect of spectral overlap must be taken into account. **Figure 2** shows X-ray spectra of mineral specimens obtained by WDS and EDS. Carbon conductive coating was applied to the specimens. Since the energy resolution of WDS is high, the peaks of B and C are completely separated in the WDS spectra. On the other hand, in the EDS spectra, the peak of B overlaps with the background of C. In the spectrum of Danburite with B concentration of 8.63%, B peak is slightly detected but quantitative evaluation of B is difficult. In the spectrum of Axinite with B concentration of 1.25%, B peak is not detected. In EDS spectra of light elements, there are many overlaps of L lines and M lines of heavy elements. Thus, it may be difficult to detect trace light elements as in the case of analyzing B. Moreover, we have to point out that even in

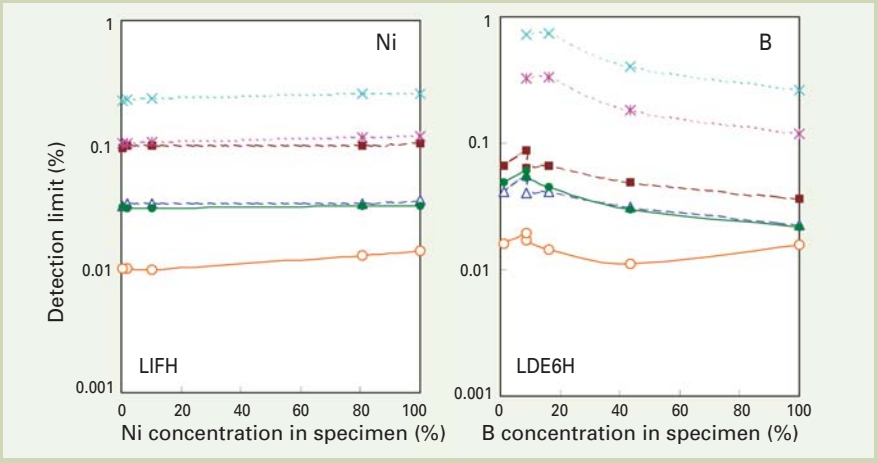

Fig. 1 Detection limits for Ni and B. The detection limit for Ni (heavy element) shows constant values regardless of its concentration variations, whereas the detection limit for B (light element) differs remarkably depending on its concentration because the light elements are severely absorbed by the matrix.

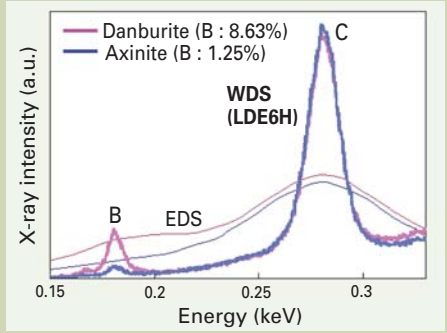

Fig. 2 WDS and EDS spectra of mineral specimens. Carbon coating was applied to the specimens. In the EDS spectra, since the peak of B overlaps with the background of C, even when B concentration is about 8%, detection and quantitative evaluation become difficult.

EDS analysis of heavy elements, if many spectral overlaps appear in the spectra, the detection of trace heavy elements is difficult.

Next, using the graph for Ni in **Fig. 1**, the detection limits for each analytical condition are compared. When comparing ① (Qual.: all by WDS) (total measurement time: 5 minutes) and ⑤ (EDS: 5 min.), the detection limits for both conditions are about 0.1%. This indicates that the detection limit in EDS analysis can reach the same level as that in Qualitative analysis of all elements by WDS if taking enough time for measurement (e.g. 5 minutes). When comparing WDS analytical conditions with a measurement time of 1 minute, that is, conditions ② to ④ are compared, the detection limits for ② (Qual.: trace) and ③ (Quant.: normal) show both 0.03%. For ④ (Quant.: trace), the detection limit is 0.01%; thus, the best detection limit under normal analytical conditions of EPMA (WDS) is the order of 0.01%. From the comparison of detection limit for condition ④ (Quant.: trace) and condition ⑥ (EDS: 1 min.), it is found that the detection limit for the analysis of specific elements by EDS is more than one order of magnitude worse than WDS with the same measurement time.

As stated above, the detection limit given by equation ② improves in proportion to the square root of the probe current and the measurement time. As shown in **Fig. 1**, the WDS detection limit for condition ④ (Quant.: trace) improves when setting the probe current to 10 times as high as that for condition ③ (Quant.: normal). Whereas the EDS detection limit for condition ⑤ (EDS: 5 min.) improves when setting the measurement time to 5 times as long as that for condition ⑥ (EDS: 1 min.). Thus, the EDS detection limit improves when increasing the measurement time. But in order to compensate the great difference (one order of magnitude) in detection limit between WDS and EDS, as confirmed from conditions ④ and ⑥, we must set the EDS measurement time to 100 times as long as that for ordinary measurement. This is not a practical analytical condition. On the other hand, when WDS analysis is performed for trace elements whose concentrations are 0.01% or lower, if the probe current is further increased to the μA order and if the measurement time is set long, compared to condition ④, the detection limit of the order of 10 ppm can be obtained. As a result, the difference in detection limit between WDS and EDS becomes greater, more than two orders of magnitude.

Figure 3 shows the measurement results of the detection limits for several elements besides Ni and B at an accelerating voltage of 15 kV under condition ③ (Quant.: normal). In this measurement, pure substances were used except for N and O (for N: AlN, for O: Al_2O_3). The results show that in condition ③, the detection limit for heavy elements is approximately 0.02% to 0.05%, whereas the detection limit for light elements differs remarkably depending on the analyzing crystal, but this limit reaches the same level as that for heavy elements if the optimum analyzing crystals are selected for each light element. However, this detection limit value is obtained from pure substances; therefore, as was explained before, in practical trace-element analysis, we have to take account of the absorption effect from the matrix in WDS and the effect of spectral overlaps as well as the absorption effect in EDS. When we take account of the results in **Fig. 3**, the detection limits for Ni for each analytical condition in **Fig. 1** and the effects of absorptions and spectral overlaps for light elements, the order of detection limit for light and heavy elements in typical qualitative and quantitative analysis is given in **Fig. 4**.

As an example of the detection of trace elements, WDS spectra of P and Sn in a stainless steel are shown in **Fig. 5**. In this experiment, measurement time was 1 minute. With a higher probe current, 0.029 mass% P is detected. Also, under a longer measurement time, it is confirmed that Sn of 0.01 mass% or below is detected.

Detection Limit in Area Analysis

In area analysis, although the measurement time per pixel point is very short compared to point analysis (qualitative and quantitative analysis), the intensity for one pixel point is actually calculated to be the mean value of the

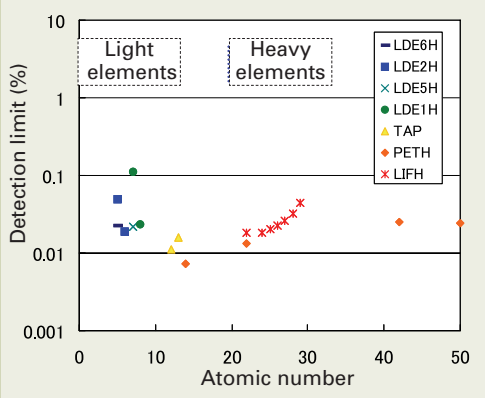

Fig. 3 Detection limits for several elements. Analytical condition of ③ in Table 2 is used at 15 kV. Measured specimens are pure substances of each element, except for N and O (N: AlN, O: Al_2O_3).

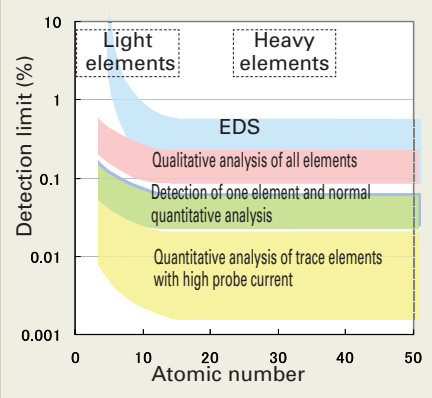

Fig. 4 Conceptual diagram of detection limit in typical qualitative and quantitative analysis conditions.

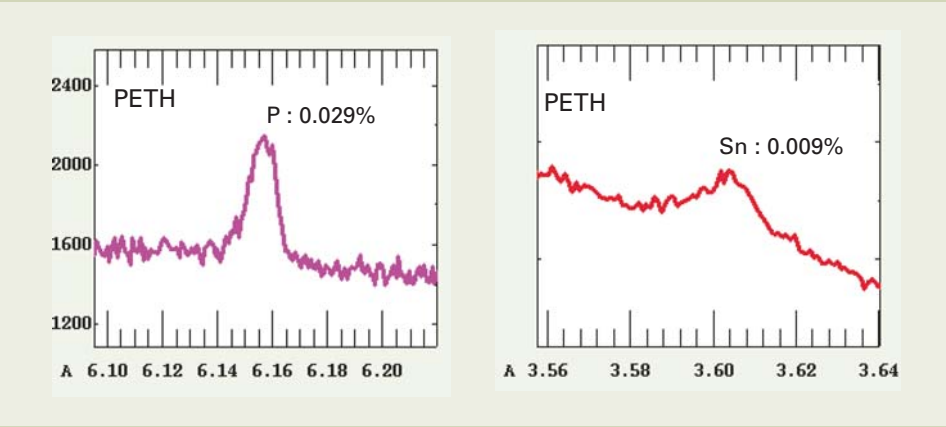

Fig. 5 Example of detection of trace elements P and Sn in stainless steel. Analytical condition: For P: 15 kV, 5 μA, total measurement time 1 minute. For Sn: 15 kV, 10 mA, total measurement time 10 minutes. With a high probe current of the order of μA, 0.029 mass% P is detected. Also under a longer measurement time, Sn of 0.01 mass% or below is detected.

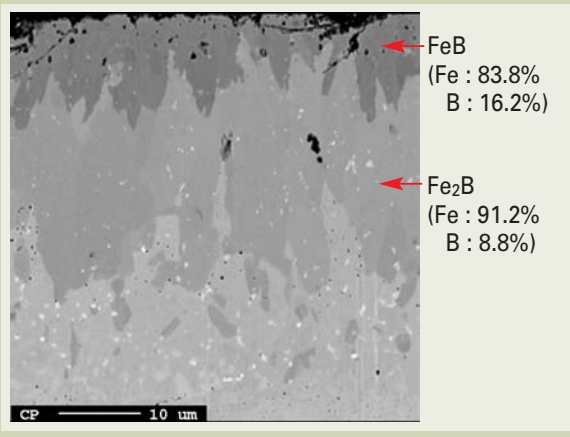

Fig. 6 FeB/Fe_2B backscattered electron image (at 10 kV). Concentration in the figure is expressed by mass%.

intensities for the surrounding 9 pixel points or 16 pixel points; therefore, the detection limit is rather better. As an example, we consider the analytical condition for area analysis of Ni by WDS where the accelerating voltage is 15 kV, the probe current is 50 nA, measurement time per pixel point is 30 msec/pix, pixels are 256 × 256 and the total measurement time is 30 minutes. Under this condition, the detection limit in area analysis is 0.28% for the mean value of 9 pixel points calculated from the value obtained in point analysis. If area analysis includes background measurement, or if the background intensity is very low so that this intensity can be neglected, even in area analysis, the detection limit comparable to that for qualitative analysis of all elements can be obtained.

However, the main purpose of area analysis is to visually distinguish a slight concentration difference in the distribution on the specimen surface rather than to detect trace elements. If an X-ray intensity P_{cnt} is given in concentration X%, in order to consider to what extent of concentration difference can be distinguished, we define significant concentration difference to be Y%, and intensity variation due to concentration difference to be P_{Ycnt}. If the variation of P_{Ycnt} is greater than the standard deviation of P_{cnt}, P_{Ycnt} can be regarded to have a significant difference to P_{cnt}. If the background is low enough, the distinguishable concentration difference Y% is given by the following equation

$$\sqrt{P_{cnt}} < P_{Ycnt} = \frac{Y}{X} P_{cnt} \qquad \therefore Y > \frac{X}{\sqrt{P_{cnt}}} \qquad \cdots\cdot(3)$$

Here, $\sqrt{P_{cnt}}$ represents S/N of an X-ray

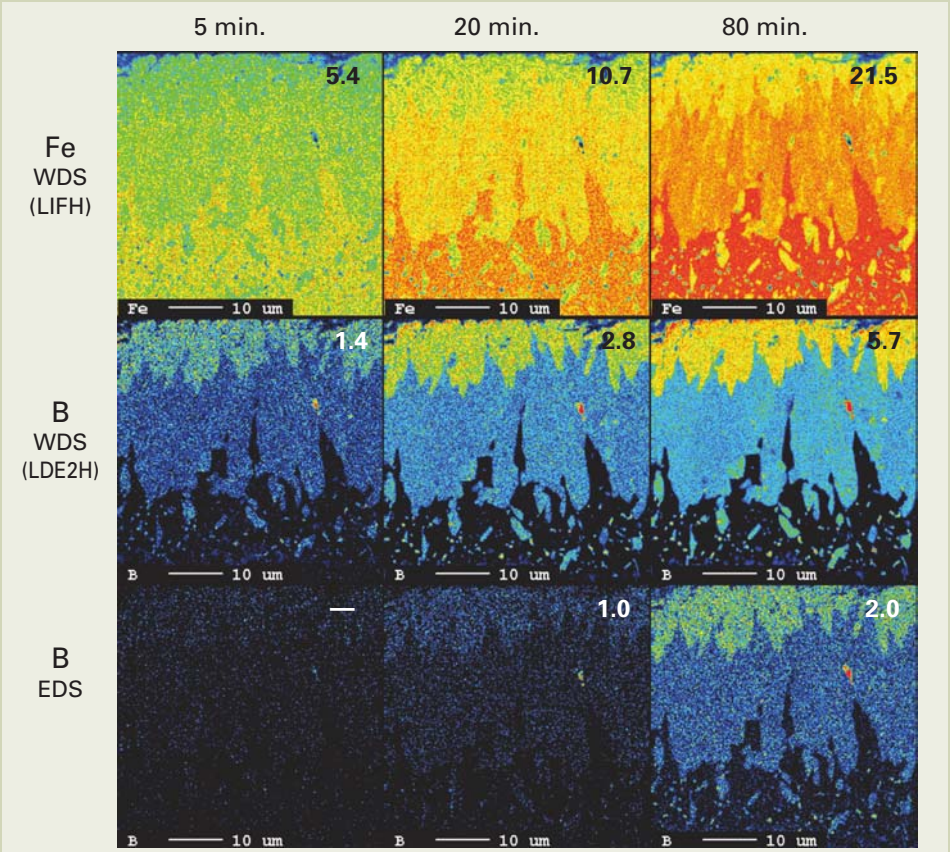

Fig. 7 X-ray maps of FeB/Fe_2B. Maps show the S/N improvement with a change of the measurement time (50 nA at 10 kV,). Numerical values on top of the maps are total measurement times. Numerical values on each map are $\sqrt{P}$ calculated from the mean X-ray intensity (P) of each map. When P = 0, values are not displayed. S/N improves as the measurement time is set longer, and concentration difference is clearly shown at a measurement time of 5 minutes for WDS and 80 minutes for EDS.

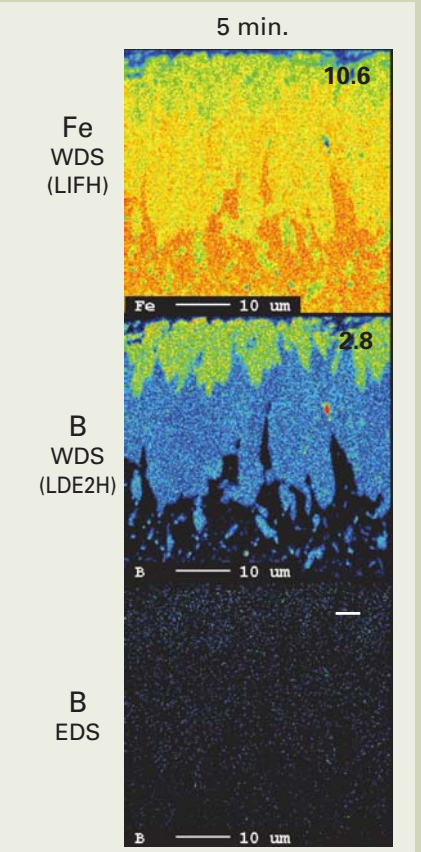

Fig. 8 X-ray maps of FeB/Fe_2B at a high probe current (200 nA at 10 kV). Numerical values for the maps are the same as those for Fig. 7. Probe current is set 4 times as high as that for Fig. 7. In WDS maps, both Fe and B show the same quality data as those obtained at a probe current of 50 nA and a measurement time of 20 minutes (see Fig. 7).

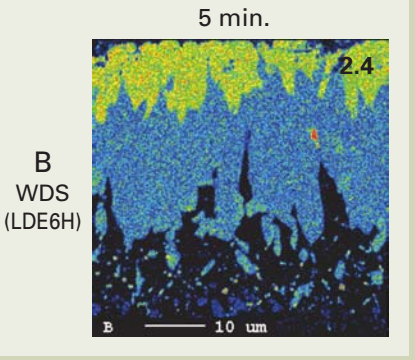

Fig. 9 X-ray map of FeB/Fe_2B obtained by the use of an analyzing crystal LDE6H for B (50 nA at 10 kV). Numerical values for the map are the same as those for Fig. 7. Analytical condition is the same as that for Fig. 7 except for the analyzing crystal. Fig. 9 data shows much better result than that obtained at a probe current of 50 nA and 20 minutes measurement time (see Fig. 7).

map. In area analysis, normally background is not measured; therefore, S/N of the map is given by $P_{cnt}/\sqrt{P_{cnt}}$ ($\sqrt{P_{cnt}}$ is the standard deviation of peak intensity). As in equation (2) which defines the detection limit, when P_{cnt} is expressed by the count rate per unit time and unit probe current, the standard deviation of peak intensity is given by $\sqrt{P}\times\sqrt{i\cdot t}$, and S/N increases in proportion to the square root of current i and time t. From equation (3), as the S/N of the map increases, the more a slight concentration variation can be distinguished. However, if $P_{cnt} \simeq B_{cnt}$, that is, if the background intensity is high or if the concentrations of elements to be analyzed are low, it is essential to simultaneously use the background measurement function in area analysis and then, attempt to improve S/N.

It should be noted that equation (3) is based on a statistical evaluation for one analysis point. As in the case of detection limit, owing to the characteristics of the map, there are many cases where a slight concentration variation can be distinguished. In addition, by using pixel interpolation in the map-processing function or smoothing, S/N can be improved. For example, when we consider the mean value of 9 points, a concentration difference, which is 1/3 as low as that obtained in equation (3), is distinguishable. However, if P_{cnt} is extremely low, statistical evaluation cannot be applied. Thus, in order to obtain high-quality data, when acquiring a map, it is desirable that $P_{cnt}\geqslant 10$.

As an example showing that concentration difference becomes clear due to the improvement and increase of S/N, area analysis results of FeB/Fe_2B are presented. **Figure 6** shows a backscattered electron image (BEI) and **Fig. 7** shows X-ray maps obtained by WDS and EDS under an accelerating voltage of 10 kV and a probe current of 50 nA. In this condition, the detection sensitivity of EDS is optimized. The numerical values at the upper right of the maps are $\sqrt{P_{cnt}}$ calculated from the mean X-ray intensity of each map. By improving S/N, the concentration difference of Fe between FeB/Fe_2B is clearly shown. In the case of B, the concentration difference between FeB and Fe_2B becomes clear under a measurement time of 5 minutes in WDS and under a measurement time of 80 minutes in EDS, which needs more than 10 times of the measurement time for WDS.

Figure 8 shows X-ray maps of FeB/Fe_2B obtained at an accelerating voltage of 10 kV and a measurement time of 5 minutes. We increased the probe current to 200 nA in this analysis. In WDS, both Fe and B show the same quality data as those obtained at a probe current of 50 nA and a measurement time of 20 minutes in **Fig. 7**. This result indicates that when increasing the probe current, efficient and rapid analysis can be performed by WDS. But it should be noted that when an analysis is performed at a high magnification, sometimes the X-ray spatial resolution is degraded due to the increased probe diameter with increasing the probe current. On the other hand, in EDS, even when using a probe current higher than that optimizes the detection sensitivity, the quality of X-ray mapping data is not improved.

In addition, in WDS, it is possible to perform efficient analysis especially when optimum analyzing crystals are used for each light element. **Figure 9** shows an X-ray map of FeB/Fe_2B under the following analytical condition: An analyzing crystal LDE6H for B was used and mapping data was acquired at an accelerating voltage of 10 kV, a probe current of 50 nA and a measurement time of 5 minutes. Comparing the map in **Fig. 9** with the data of B in **Fig. 7**(analyzing crystal: LDE2H), which is obtained under the same probe current and the same measurement time as **Fig. 9**, **Fig. 9** shows much better result than **Fig. 7**.

Applications to Magnetic Materials

Detection of trace elements

Here, we will show applications to magnetic materials to verify the high capability of EPMA (WDS) in practical analysis of trace elements. **Figure 10** shows a backscattered electron image of a magnetic material. The main composition of the matrix obtained by EPMA quantitative analysis is as follows. Fe: 67.0, Nd: 20.0, Dy: 5.7, Co: 3.5, B: 0.45, Al: 0.25 and Mn: 0.1 (mass%).

Qualitative analysis of all elements by WDS was performed on the matrix at a probe current of 100 nA at 15 kV and a measurement time of 5 minutes. As a result, all the above matrix elements were detected, including 0.1% Mn and 0.45% B. This result agrees with the order of the detection limits (heavy elements: 0.1% ~, light elements: 0.3%~) for condition ① (Qual.: all) in the section of Detection Limits in Qualitative and Quantitative Analysis.

Figure 11 shows part of WDS spectra obtained by qualitative analysis of all elements. Although an Nd-Lβ_3 peak exists near an Mn-Kα peak, a trace amount of Mn is detected without the influence of the Nd-Lβ_3 peak. **Figure 12** shows EDS and WDS spectra obtained on the matrix. In this figure, the abscissa shows energy (keV). In the EDS spectrum, due to the effect of the background of Nd, an Mn peak cannot be observed. Since rare earth elements show complicated and multiple peaks, when EDS is used for analyzing this type of specimen, the peaks extensively overlap even in the energy range of heavy elements, and the detection limit is degraded.

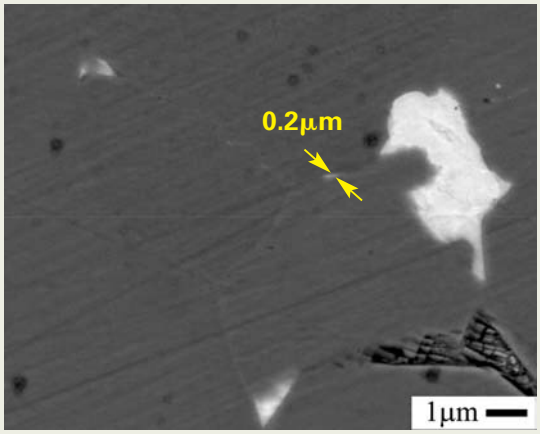

Fig. 10 Backscattered electron image of a magnetic material (at 10 kV). A form of grain boundaries on the surface of a specimen is different depending on locations. The most of grain boundary phase has a width of 0.1 μm or below, but the maximum width is 0.2 μm.

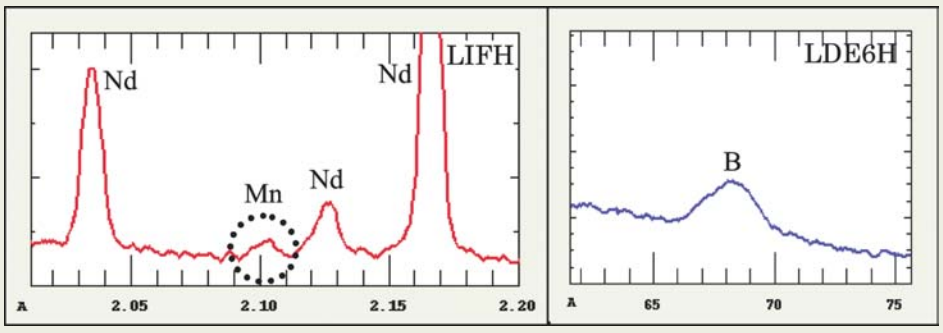

Fig. 11 Result of trace-element detection of a magnetic-material matrix obtained by WDS qualitative analysis of all elements. Analytical condition: accelerating voltage 15 kV, probe current 100 nA, total measurement time 5 minutes. 0.1% Mn is detected without the influence of Nd. In addition, 0.45% B (light element) is detected.

Thus, this analysis result confirms that WDS is very effective for detecting and analyzing trace elements in specimens that contain rare earth elements.

Distinction of concentration variation of rare earth elements

We distinguished the concentration variation of rare earth elements in the matrix by phase analysis. **Figure 13** shows a WDS area analysis result of Nd and Dy and a phase analysis result in which the area analysis result was quantified by calibration factor and phase analysis was applied. The analytical condition was a probe current of 100 nA at 15 kV. From **Fig. 13**, it is seen that there exist some phases where the concentrations of Nd and Dy in the matrix are changed by approximately 1%, respectively. In particular, the variation for the concentration of Nd is very small. Unless a sufficient S/N is obtained, it is impossible to detect and distinguish multiple phases that contain different compositions of elements on a scatter diagram. As is shown in the EDS spectrum of **Fig. 12**, EDS can analyze rare earth elements of Nd and Dy. However, in this analysis, a Dy–Lα peak and a Dy–Lβ peak overlap a peak of Fe which is a main element; therefore, it is necessary to apply peak deconvolution or measure M lines for accurate analysis of Dy by EDS. To the contrary, since WDS has higher peak to background ratio than EDS, this small concentration variation can be efficiently distinguished even when the measurement time is the same as that for EDS.

Analysis of elements distributed on grain boundaries

Next, examples of the analysis of element distribution on grain boundaries are shown. It is known that on grain boundaries, Co and Al are concentrated, which also exist in the matrix. **Figure 10** reveals that a form of grain boundaries on the surface of the specimen is different depending on locations, and that most of the grain boundary phase has a width of 0.1μm or below, but the maximum width is 0.2 μm.

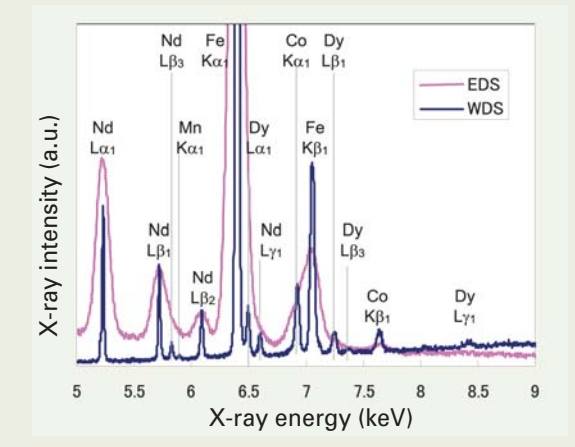

Fig. 12 EDS and WDS spectra of a magnetic-material matrix.

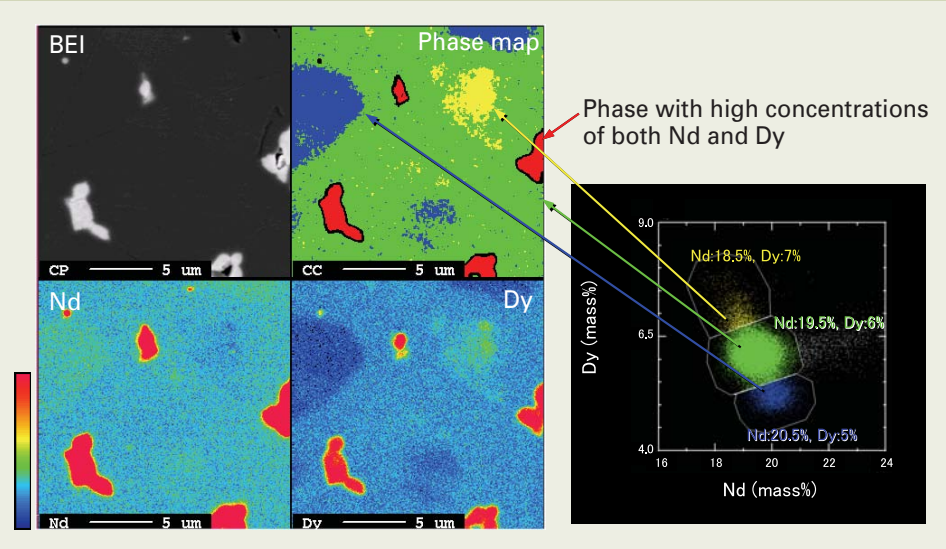

Fig. 13 Analysis result of concentration variation of rare earth elements in a magnetic-material matrix (100 nA at 15 kV). Three phases where the concentrations of Nd and Dy differ by about 1% are distinguished on a scatter diagram. These clusters are differentiated by color (yellow, green and blue) to create the phase map. In addition, a phase with high concentrations of each element is colored red.

When analyzing these sub-micro-areas, we have to consider the different analytical conditions optimized for "detection" and "quantitative evaluation." The spread of the analyzing volume of EPMA is given by the numerical value that adds the X-ray generation volume (generation depth) and the probe diameter. Normally, this is about 1 μm. Analyzing sub-micro-particles, the volume of the particle is smaller than that of analysis area; therefore, the X-ray intensity also decreases. That is, the "detection" of elements distributed on sub-micro-areas can be regarded as the detection of trace elements. As the detection limit is better, the smaller particles can be detected [2]. If the main purpose of analysis is "detection" of elements that are distributed in sub-micro-areas, when we use an analytical condition with better detection limit regardless of analyzing volume, the elements can be efficiently detected.

On the other hand, when performing "quantitative evaluation," at least 90% of X-rays must be generated from particles. This means that it is necessary to reduce the X-ray generation volume by applying a low accelerating voltage and a small-diameter probe. To meet this requirement, a FE-EPMA (Field-Emission Electron Probe Microanalyzer), JXA-8500F, is very effective because this powerful analyzer provides a small probe even at a low accelerating voltage. Studies using the JXA-8500F up to now prove that this FE-EPMA offers high-accuracy quantitative analysis of very small areas; therefore, the composition of an eutectic layer with a thickness of 0.2 μm at the boundary between solder and copper can be identified using a FE-EPMA [2]. We emphasize that when a high X-ray spatial resolution is required for area analysis, it is necessary to consider better analytical conditions as in case of quantitative evaluation. For the details of discussion on micro-area analysis using EPMA, see references [2] and [3].

Table 4 shows the X-ray generation depth of Co and Al in a magnetic material calculated from a Monte Carlo simulation. **Figure 14** shows the relationship between the probe diameter and the probe current of the FE electron gun, LaB_6 electron gun and W hairpin-gun, at 10 kV accelerating voltage. These facts imply that if using an accelerating voltage of 10 kV and also a FE-EPMA which provides a small-diameter probe at this accelerating voltage, elemental distributions on small grain boundaries can be acquired with high spatial resolution. To prove this, we performed area analysis on grain boundaries using the JXA-8500F FE-EPMA.

We carried out area analysis of Co and Al at a probe current of 100 nA at 10 kV and a magnification of × 5,000. In this experiment, total measurement time was set to 30 minutes, corresponding to a generally-used measurement time. With this measurement time, the distribution of Co was observed on a location of grain boundaries greatly emerging, but the distribution was not clear on small grain boundaries. For Al, the distribution along grain boundaries was not obtained. To solve this situation, we set measurement time to as long as 150 minutes. **Figure 15** shows an area analysis result with this long measurement time. It is shown that S/N for both Co and Al was greatly improved; therefore, the distribution of these elements on grain boundaries became clear. In

this experiment, priority was placed on the X-ray spatial resolution for X-ray maps, and measurement time was set longer without changing the probe current. This means that for example, if the probe current is increased 2 to 3 times, the X-ray spatial resolution is degraded but the distribution of Co and Al on grain boundaries can be efficiently obtained.

Furthermore, we performed area analysis at an increased magnification. **Figure 16** shows the result of analysis. Under analytical conditions of an accelerating voltage of 10 kV, a probe current of 30 nA, a magnification of x20,000 and a measurement time of 120 minutes, we also carried out background measurement and net X-ray intensities were obtained. We converted these X-ray intensities to mass concentrations using a calibration factor and displayed a line profile on maps. On the location where grain boundaries greatly emerge, shown at the right of the maps, concentrations of Co: 5 mass% and Al: 0.3 mass% were obtained. This indicates that slight concentration variations from the matrix can be distinguished (Co: 1.5mass% and Al: 0.05mass%).

The FE-EPMA (WDS), which has a high capability of analyzing trace elements and provides a small probe at a low accelerating voltage, makes it possible to distinguish slight concentration variations on these small grain boundaries.

Table 4 X-ray generation depth of Co and Al in a magnetic material (accelerating voltage: 10 kV and 15 kV).

	10kV	15kV
Co	0.12μ m	0.42μ m
Al	0.21μ m	0.36μ m

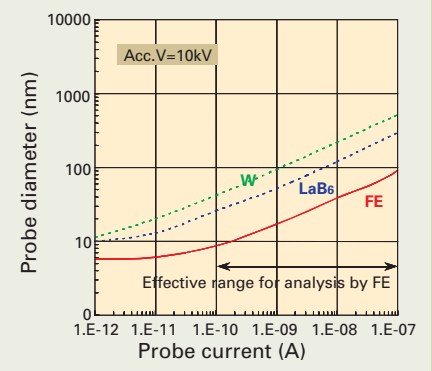

Fig. 14 Relationship between the probe diameter and the probe current of the FE electron gun, LaB_6 electron gun and W hairpin-gun, at 10 kV accelerating voltage.

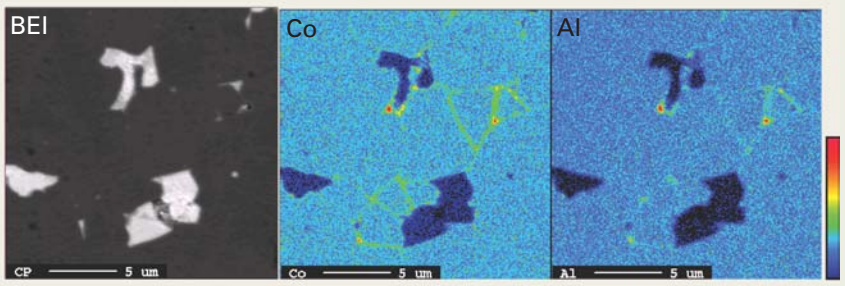

Fig. 15 Distribution of Co and Al on grain boundaries in a magnetic material (100 nA at 10 kV,). FE-EPMA (JXA-8500F) was used for measurement.

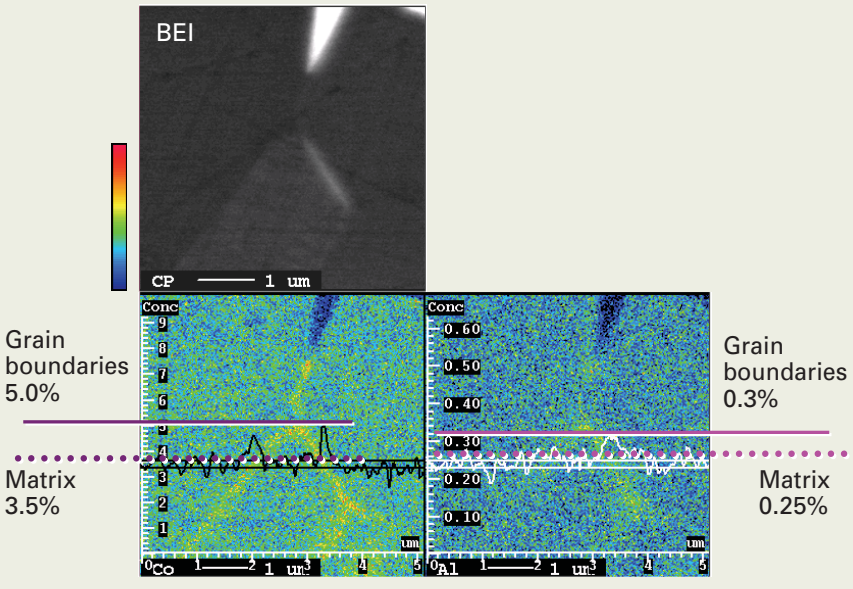

Fig. 16 Concentrations of Co and Al on grain boundaries in a magnetic material (30 nA at 10 kV). FE-EPMA (JXA-8500F) was used for measurement. On the location where grain boundaries greatly emerge, concentrations of these elements are obtained by a line profile: Co: 5.0 mass% and Al: 0.3 mass%. This result indicates that slight concentration variations from the matrix can be distinguished (Co: 1.5 mass% and Al: 0.05 mass%).

Summary

In this article, we obtained the detection limits in normal analytical conditions of EPMA and examined the practical concentration which can be measured. The examination results are summarized below.

(1) Detection limits in qualitative and quantitative analysis was summarized in **Fig. 4**.

(2) The detection limit in area analysis is comparable to that for qualitative analysis of all elements shown in **Fig. 4**.
The distinguishable concentration difference is 1/3 as low as that obtained in equation (3).

(3) Both in qualitative/quantitative analysis and area analysis, in proportion to the square root of the probe current and the measurement time, the more trace elements can be detected and the slighter concentration difference can be distinguished.

(4) We verified the high capability of EPMA (WDS) in practical analysis of trace elements using examples of analysis of magnetic materials.

Detection of trace elements:
From complicated WDS spectra of rare earth elements, 0.1mass% Mn and 0.45mass% B were detected under the analytical condition of qualitative analysis of all elements.

Distinction of concentration variation of rare earth elements:
Concentration difference of about 1% for Nd and for Dy in the matrix was distinguished by phase analysis.

Analysis of elements distributed on grain boundaries:
Using a FE-EPMA, slight concentration differences of specific elements between the matrix and small grain boundaries were distinguished(Co:3.5mass%→5mass%,Al: 0.25mass%→0.3mass%).

References

[1] The Surface Science Society of Japan, Electron Probe Micro Analyzer, p.11 (1998) (In Japanese)

[2] N. Mori, JEOL Application Note XM105 (2003) (In Japanese)

[3] N. Mori, JEOL Application Note XM109 (2005) (In Japanese)

Introduction of New Products

Electron Microscope
JEM-1400

The JEM-1400 is a high performance, high contrast, 120 kV TEM with excellent imaging and analytical capabilities in one compact, easy-to-use instrument. With an acceleration voltage of 40 to 120 kV, the JEM-1400 is suitable for biological, polymer and materials science applications.
The new JENIE™ software included with the JEM-1400 offers a set of tutorials and user guides designed to help beginning microscopists familiarize themselves with the microscope, but also allows experienced users to explore and understand advanced features. The Windows™ GUI is programmed with the latest in Windows™ based technologies and allows remote operation and communication between groups via a TCP/IP connection and a web browser.
The JEM-1400 also supports optional STEM digital imaging/scanning circuitry which displays STEM images (BF/DF) on the standard GUI. An EDS can be added for elemental mapping.

Features

Newly designed electron optics system

The JEM-1400 is designed on the concept of "unity of camera and column." The new electron optics system is optimized for integrated use with any digital CCD camera. Thus, the JEM-1400 provides high-contrast images and rotation-free from a low magnification of × 200.

New GUI – TEM Center –

The JEM-1400 can be operated using our newly designed GUI screens. The screens for routine operations are arranged in an easy-to-understand layout where items appear on the screen from top to bottom corresponding to the location of each unit in the column. This makes intuitive operation of the TEM Center.

Navigation – JENIE –

The JEM-1400 incorporates a TEM Navigation System, "JENIE (JEOL Electron microscope Navigation Interactive Engine)." When the operator selects an item to operate the screen, an easy-to-understand video appears to teach the operating procedure. Thus, JENIE ensures that beginners can operate the microscope easily.

Newly developed digital CCD camera

A new digital CCD camera, developed for the JEM-1400, employed an interline system that does not require beam blanking. This innovative CCD camera makes it possible to acquire high-speed data. Also, a range of CCD cameras from different manufacturers can be integrated.

Extensive application programs

Integration of the digital CCD camera into the TEM enables extensive application programs to be installed in the JEM-1400. The powerful programs automate and facilitate complicated operations such as automatic focusing and montage imaging.

A wealth of optional accessories

The JEM-1400 is provided with a wealth of optional accessories for extending its applications, including STEM, EDS and TEM tomography. For example, in the element analysis, the JEM-1400 can accommodate an EDS detector that requires liquid nitrogen only during analysis.

High quality images obtainable over the full range of magnification from lower to higher for lattice imaging

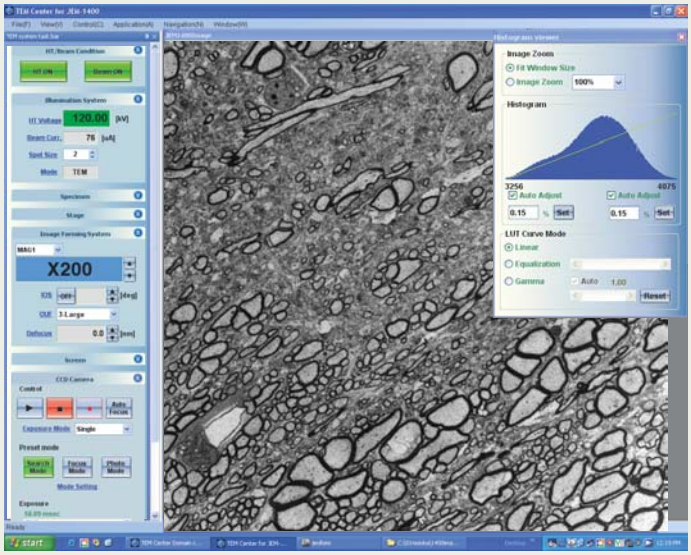

Specimen : Spinal cord of frog (CCD camera image)
Direct magnification : × 50

Introduction of New Products

Thermal FE SEM
JSM-7001F

The JSM-7001F, Thermal Field Emission SEM, is the ideal platform for demanding analytical applications as well as those requiring high resolution and ease-of-use. The JSM-7001F has a large, 5-axis, fully eucentric, motorized, automated specimen stage, a one-action specimen exchange airlock, small probe diameter even at large probe current and low voltage, and expandability with ideal geometry for EDS, WDS, EBSP, and CL. The specimen chamber handles specimens up to 200 mm in diameter.
A new Windows XP™ based computer interface allows for unprecedented ease of operation including function buttons that switch operation modes quickly and easily. Up to four live images can be simultaneously viewed, including signal mixing, and a single scan can record and store all four images at once.
The JSM-7001F SEM also supports full integration of EDS, WDS, e-beam lithography, and an image database. Stage automation is standard with a 5-axis computer control of X, Y, Z Tilt and eucentric rotation.

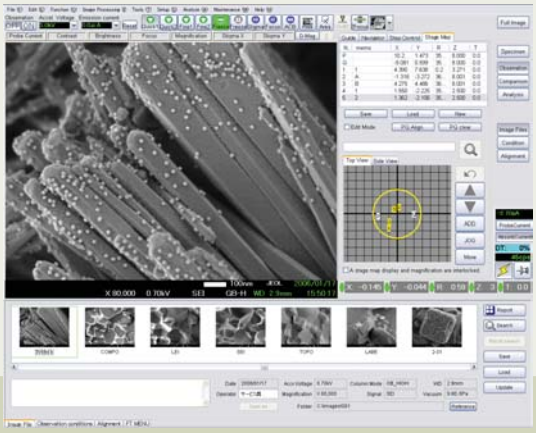

Observation mode

High-Performance Compact SEM
JCM-5700

The compact JCM-5700 features the high performance expected from the research grade SEM and the high throughput required by the industries. One can be acquainted with the operation of the SEM in a short time due to the fully automated operation including the Smile shot, which sets the SEM operation parameters just by selecting a kind of specimen to be observed.
The elemental analysis capability is embedded in the JCM-5700 Analytical Pack without requiring a larger footprint. The observation and elemental analysis are carried out seamlessly. A click on a feature on the SEM monitor starts the elemental analysis. The qualitative and quantitative analyses are done precisely in a short time.
The low vacuum SEM mode in JCM-5700 L-PAC allows one to observe and analyze non-conductive specimens without conductive coating.
The JCM-5700 is on wheels to allow one to move it around easily. It fits easily in any corner in your laboratory.

Introduction of New Products

FT NMR System
JNM-ECS Series

The ECS series of NMR spectrometers is designed for any laboratory needing an easy-to-use, reliable, routine NMR system for synthetic molecular characterization and mixture analysis. The ECS NMR series is available in 300 and 400 MHz models. The console is designed around a modular, digital NMR electronics chassis controlled by an intelligent acquisition computer. For unprecedented flexibility, the JEOL NMR system offers a Windows XP™ and Mac OSX™. Both the workstation and spectrometer may be connected to a standard network, allowing seamless remote operation anywhere in the world.

Features

- Compact spectrometer
- Advanced architecture proven in JNM-ECA series
- Stable, high sensitivity digital spectrometer
- High sensitivity autotune probe
- Advanced software and automation
- Network spectrometer

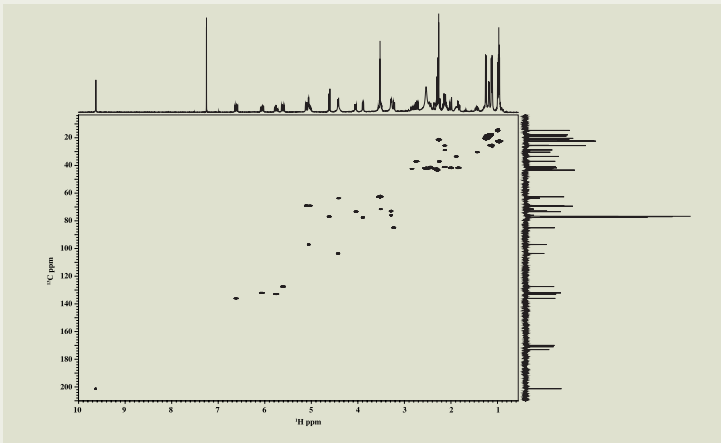

5mg Josamycin in $CDCl_3$, ^{13}C-^{1}H HSQC, 4 scans

AccuTOF TLC
JMS-T100TD

You will get TLC-MS Spectra in only few seconds!

JEOL has developed TLC sampler for DART™ Ion Source and achieved the highest throughput TLC-MS in the world.
" Time of Fight" spectrometry makes it possible to measure the elemental composition.

Configuration

- Analyzer : Time of Fight Mass Spectrometer (Reflection Type TOF)
- Ion Source : DART Ion Source with TLC Sampler
- Ion Source Power Supply : DART Ion Source Power Supply
- Data System : PC (DVDRW), TFT Monitor, Laser Printer

ISO 9001 & 14001 REGISTERED FIRM
DNV Certification B.V., THE NETHERLANDS

JEOL ISO 9001 & ISO 14001 Certificated

Certain products in this brochure are controlled under the "Foreign Exchange and Foreign Trade Law" of Japan in compliance with international security export control. JEOL Ltd. must provide the Japanese Government with "End-user's Statement of Assurance" and "End-use Certificate" in order to obtain the export license needed for export from Japan. If the product to be exported is in this category, the end user will be asked to fill in these certificate forms.

http://www.jeol.com/

JEOL Ltd. 1-2 Musashino 3-chome Akishima Tokyo 196-8558 Japan Sales Division ☎(042)528-3381 FAX(042)528-3386

ARGENTINA
COASIN S. A. C. I. yF.
Virrey del Pino 4071, 1430 Buenos Aires, Argentina
Telephone: 54-11-4552-3185
Facsimile: 54-11-4555-3321

AUSTRALIA & NEW ZEALAND
JEOL (AUSTRALASIA) Pty. Ltd.
Unit 9/750-752 Pittwater Road Brookvale, NSW 2100, Australia
Telephone: 61-2-9905-8255
Facsimile: 61-2-9905-8286

AUSTRIA
LABCO GmbH
Dr.-Tritremmel-Gasse 8, A-3013 Pressbaum, Austria
Telephone: 43-2233-53838
Facsimile: 43-2233-53176

BANGLADESH
A. Q. CHOWDHURY & CO. PVT. Ltd.
Baridhara Central Plaza 87, Suhrawardy Avenue,
2nd Floor Baridhara, Dhaka-1212, Bangradesh
Telephone: 880-2-9862272, 9894533
Facsimile: 880-2-8854428

BELGIUM
JEOL (EUROPE) B. V.
Planet II, Building B Leuvensesteenweg 542, B-1930 Zaventem, Belgium
Telephone: 32-2-720-0560
Facsimile: 32-2-720-6134

BRAZIL
FUGIWARA ENTERPRISES INSTRUMENTOS CIENTIFICOS LTDA.
Avenida Itaberaba,3563 02739-000 Sao Paulo, SPl Brazil
Telephone: 55-11-3983 8144
Facsimile: 55-11-3983 8140

CANADA
JEOL CANADA, INC.(Represented by Soquelec, Ltd.)
5757 Cavendish Boulevard, Suite 540, Montreal, Quebec H4W 2W8, Canada
Telephone: 1-514-482-6427
Facsimile: 1-514-482-1929

CHILE
TECSIS LTDA.
Avenida kennedy 5454 - Piso 5 Vitacura, Santiago, Chile
Telephone: 56-2-401-8520
Facsimile: 56-2-410-8541

CHINA
JEOL LTD., Beijing Office
Room B2308A, Vantone New World Plaza, No. 2 Fuwai Street,
Xicheng District,Beijing, 100037, P.R. China
Telephone: 86-10-6804-6321/6322/6323
Facsimile: 86-10-6804-6324

JEOL LTD., Shanghai Office
11 F2, Sanhe Building, No.121 Yan Ping Road, Shanghai 200042, P.R. China
Telephone: 86-21-62462353, 55
Facsimile: 86-21-62462836

JEOL LTD., Wuhan Office
Room 3216, World Trading Bldg., 686 Jiefang Street, Hankou,
Wuhan, Hubei 430032 P.R. China
Telephone: 86-27-8544-8953
Facsimile: 86-27-8544-8695

JEOL LTD., Guagzhou Office
N3104, World Trade Center Building 371-375,
Huan Shi East Road, Guang zhou, 510095, P.R. China,
Telephone: 86-20-8778-7848
Facsimile: 86-20-87784268

JEOL LTD., Chengdu Office
1807A Zongfu Building, No. 45 Zhongfu Road
Chengdu, Sichuan, 610016 P.R. China
Telephone: 86-28-86622554
Facsimile: 86-28-86622564

FARMING LTD.
Unit 1009, 10/F., MLC Millennia Plaza, 663 King's Road,
North Point, Hong Kong
Telephone: 852-2815-7299
Facsimile: 852-2581-4635

CYPRUS
MESLO LTD.
Scientific & Laboraty Division, P. O. Box 27709, Nicosia-Cyprus
Telephone: 357-2-666070/666080
Facsimile: 357-2-660355

EGYPT
JEOL SERVICE BUREAU
3rd Fl. Nile Center Bldg., Nawal Street, Dokki, (Cairo), Egypt
Telephone: 20-2-335-7220
Facsimile: 20-2-338-4186

FRANCE
JEOL (EUROPE) SAS
Espace Claude Monet,1 Allee de Giverny 78290, Croissy-sur-Seine, France
Telephone: 33-13015-3737
Facsimile: 33-13015-3747

GERMANY
JEOL (GERMANY) GmbH
Oskar-Von-Miller-Strasse 1A, 85386 Eching Germany
Telephone: 49-8165-77346
Facsimile: 49-8165-77512

GREAT BRITAIN & IRELAND
JEOL (U.K.) LTD.
JEOL House, Silver Court, Watchmead,
Welwyn, Garden City, Herts AL7 1LT, U. K.
Telephone: 44-1707-377117
Facsimile: 44-1707-373254

GREECE
N. ASTERIADIS S.A.
56-58, S. Trikoupi Str. P. O. Box 26140 GR-10022 Athens, Greece
Telephone: 30-1-823-5383
Facsimile: 30-1-823-9567

INDIA
Blue Star LTD. (HQ: Mumbai)
Analytical Instruments Department
'Sahas' 414/2 Veer Savarkar Marg,
Prabhadery Mumbai 400 025, India
Telephone: 91-22-6666-4068
Facsimile: 91-22-6666-4001

Blue Star LTD. (Haryana Delhi)
Analytical Instruments Department
E-44/12 Okhla Industrial
Area, Phase-11, New Delhi 110 020, India
Telephone: 91-11-5149-4000
Facsimile: 91-11-5149-4004

Blue Star LTD. (Calcutta)
Analytical Instruments Department
7, Hare Street Calcutta 700 001
Telephone: 91-33-2213-4133
Facsimile: 91-33-2213-4102

Blue Star LTD. (Chennai)
Analytical Instruments Department,
Garuda Building, Cathedral Road Chennai 600 086, India
Telephone: 91-44-5244-7210
Facsimile: 91-44-5244-4190

INDONESIA
PT. TEKNOLABindo Penta Perkasa
Komplek Gading Bukit Indah Blok I/11,
J1. Bukit Gading Raya Kelapa Gading Permai,
Jakarta 14240, Indonesia
Telephone: 62-21-45847057/58/59
Facsimile: 62-21-45842729

ITALY
JEOL (ITALIA) S.p.A.
Centro Direzionale Green Office Via Dei Tulipani,
1, 20090 Pieve, Emanuele (MI), Italy
Telephone: 39-2-9041431
Facsimile: 39-2-90414353

KOREA
JEOL KOREA LTD.
Dongwoo Bldg. 7F, 458-5, Gil-Dong,
Gangdong-Gu, Seoul, 134-010, Korea
Telephone: 82-2-511-5501
Facsimile: 82-2-511-2635

KUWAIT
YUSUF I. AL-GHANIM & CO. (YIACO)
P. O. Box 435, 13005-Safat, Kuwait
Telephone: 965-4832600/4814358
Facsimile: 965-4844954/4833612

MALAYSIA
JEOL (MALAYSIA) SDN. BHD. (359011-M)
205, Block A, Mezzanine Floor, Kelana Business Center 97,
Jalan SS 7/2, Kelana Jaya, 47301 Petaling Jaya, Selangor, Malaysia
Telephone: 60-3-7492-7722
Facsimile: 60-3-7492-7723

MEXICO
JEOL DE MEXICO S. A. DE C. V.
Av. Amsterdam #46 DEPS. 402, Col Hipodromo, 06100,
Mexico D. F. Mexico
Telephone: 52-5-55-211-4511
Facsimile: 52-5-55-211-0720

PAKISTAN
ANAKYTICALI MEASURING SYSTEM (PVT.) LTD. (AMS LTD)
AMS House Plot # 14C, Main Sehar Commercial Avenue, Commercial Lane 4
Khayaban-Sehar, D. H. A Phase 7 Karachi, Pakistan
Telephone: 92-21-5345581/5340747
Facsimile: 92-21-5345582

PANAMA
PROMED S. A.
Parque Industrial Costa del Este Urbanizacion Costa del Este
Apartado 0816-01755, Panama, Panama
Telephone: 507-303-3100
Facsimile: 507-303-3115

PHILIPPINES
PHILAB INDUSTRIES, INC.
7487 Bagtikan Street, SAV Makati,
1203 Metro, Manila Philippines
Telephone: 63-2-896-7218
Facsimile: 63-2-897-7732

PORTUGAL
Izasa. Portugal Lda.
R. do Proletariado, 1 2790-138 CARNAXIDE Portugal
Telephone: 351-21-424-7300
Facsimile: 351-21-418-6020

RUSSIA
JEOL LTD Moscow Office
Pereulok Krasina 16, bid 1, office 302, Moscow , Russia
Telephone: 7-495-641-11-14
Facsimile: 7-495-641-28-63

SAUDI ARABIA
ABDULREHMAN ALGOSAIBI G. T. B.
Algosaibi Bldg., Airport Rd., P. O. Box 215,
Riyadh 11411, Saudi Arabia
Telephone: 966-1-479-3000
Facsimile: 966-1-477-1374

SCANDINAVIA
JEOL (SKANDINAVISKA) A. B.
Hammarbacken 6 A, Box 716, 191 27 Sollentuna, Sweden
Telephone: 46-8-28-2800
Facsimile: 46-8-29-1647

SERVICE & INFORMATION OFFICE
JEOL NORWAY
Ole Deviks vei 28, N-0614 Oslo, Norway
Telephone: 47-2-2-64-7930
Facsimile: 47-2-2-65-0619

JEOL FINLAND
Ylakaupinkuja 2, FIN-02360 Espoo, Finland
Telephone: 358-9-8129-0350
Facsimile: 358-9-8129-0351

JEOL DEMARK
Naverland 2, DK-2600 Glostrup, Demark
Telephone: 45-4345-3434
Facsimile: 45-4345-3433

SINGAPORE
JEOL ASIA PTE. LTD.
29 International Business Park #04-02A Acer Building,
Tower B Singapore 609923
Telephone: 65-6565-9989
Facsimile: 65-6565-7552

SOUTH AFRICA
ADI Scientific (Pty) Ltd.
109 Blandford Road, North Riding,Randburg
(PO box 71295 Bryanston 2021) Republic of South Africa
Telephone: 27-11-462-1363
Facsimile: 27-11-462-1466

SPAIN
IZASA. S. A.
Aragoneses, 13, 28100 Alcobendas,
(Polígono Industrial) Madrid, Spain
Telephone: 34-91-663-0500
Facsimile: 34-91-663-0545

SWITZERLAND
JEOL (GERMANY) GmbH
Oskar-Von-Miller Strasse 1, 85386 Eching, Germany
Telephone: 49-8165-77346
Facsimile: 49-8165-77512

TAIWAN
JIE DONG CO., LTD.
7th, F1, 112, Chung Hsiao East Road, Section 1, Taipei,
Taiwan 10023, Republic of China
Telephone: 886-2-2395-2978
Facsimile: 886-2-2322-4655

JEOL TAIWAN SEMICONDUCTORS LTD.
11F, No.346, Pei-Ta Road, Hsin-Chu City 300,
Taiwan, Republic of China
Telephone: 886-3-523-8490
Facsimile: 886-3-523-8503

THAILAND
BECTHAI BANGKOK EQUIPMENT & CHEMICAL CO., LTD
300 Phaholyothin Rd. Phayathai, Bangkok 10400, Thailand
Telephone: 66-2-615-2929
Facsimile: 66-2-615-2350/2351

THE NETHERLANDS
JEOL (EUROPE) B. V.
Lireweg 4, NL-2153 PH Nieuw-Vennep, The Netherlands
Telephone: 31-252-623500
Facsimile: 31-252-623501

TURKEY
TEKSER LTD. STI.
Acibadem Cad. Erdem Sok. N ° 6/1 35660 Uskudar, Istanbul, Turkey
Telephone: 90-216-3274041
Facsimile: 90-216-3274046

UAE
Business Communications LLC.
P. O. Box 2534, Abu Dhabi, UAE
Telephone: 971-2-6348495
Facsimile: 971-2-6316465

USA
JEOL USA, INC.
11 Dearborn Road, Peabody, MA. 01960, U. S. A.
Telephone: 1-978-535-5900
Facsimile: 1-978-536-2205/2206

JEO USA, INC. WEST OFFICE
5653 Stoneridge Drive Suite #110 Pleasanton, CA. 94588, U. S. A.
Tel: 1-925-737-1740
Fax: 1-925-737-1749

VENEZUELA
GOMSA Service and Supply C. A.
Urbanizacion Montalban III
- Residencias Don Andres - Piso 7 - Apartomento 74
Avenida 3, entre calles 7 y 6 Montalban, Caracas, Venezuela
Telephone: 58-212-443-4342
Facsimile: 58-212-443-4342

VIETNAM
TECHNICAL MATERIALS AND RESOURCES IMPORT-EXPORT
JOINT STOCK COMPANY (REXCO)
Hanoi Branch,
157 Lang Ha Road, Dong da District., Hanoi, Vietnam
Telephone: 84-4-562-0516, 17/562-0535
Facsimile: 84-4-853-2511